2019

# Lignocellulosic Biomass Derived Activated Carbon for Energy Storage and Adsorption

Changle Jiang
*West Virginia University*, chjiang@mix.wvu.edu

# Lignocellulosic Biomass Derived Activated Carbon for Energy Storage and Adsorption

**Changle Jiang**

**Dissertation submitted**

**to the Davis College of Agriculture, Natural Resources and Design**

**at West Virginia University**

**in partial fulfillment of the requirements for the degree of**

**Doctor of Philosophy in**

**Forest Resources Science**

**Jingxin Wang, Ph.D., Chair**

**Edward Sabolsky, Ph.D.**

**Shawn Grushecky, Ph.D.**

**Debangsu Bhattacharyya, Ph.D.**

**Jamie Schuler, Ph.D.**

**School of Natural Resources**

**Morgantown, West Virginia**

**2019**

**Keywords: lignocellulosic biomass, biomass utilization, bioproducts, porous carbon, energy storage, adsorption**

ABSTRACT

Lignocellulosic Biomass Derived Activated Carbon for Energy Storage and Adsorption

Changle Jiang

Lignocellulosic biomass has been converted to hierarchical porous carbon materials which possess macro-, meso- and micro-pores. The natural structure of porous lignocellulosic structure was preserved during activation with further developed porosity by the activation. The activated carbon can be well applied to electrochemical double layer capacitor for transportation storage of ions as well as adsorbent materials for metal ion removal from wastewater.

The first chapter of this dissertation presents an introduction of biomass derived carbon and its applications. In the second chapter, both direct and indirect activation methods using carbon dioxide were adopted in this study. The results show that the carbon in both cases have a mixture of Type I and II isotherm which refers to a dominant microporous structure along with minor larger pores. The morphology reveals tortuous porous structure preserved after activation. The capacitances of 80.9 F/g and 92.7 F/g at current density 100 mA/g have been achieved in optimized carbon from direct and indirect activation, respectively. The surface chemistry study found that the surface functional groups also play a determinant role in capacitance besides the porosity of activated carbons.

In the third chapter, activated carbons from two different routes of KOH carbonization of biomass have been successfully fabricated. The yield study showed that the direct KOH carbonization has a higher yield than indirect carbonization. The porosity parameters of both activated carbon such as specific surface area, total pore volume and microporous volume are relatively higher in direct KOH activation sample. The Barium adsorption test showed that both activated carbons can be used to adsorb Ba from actual shale gas flowback water. The activated carbon from direct KOH carbonization has a higher reduction rate which is 11.3% at a relatively low carbon loading (carbon to water mass ratio at 1:38). In the fourth chapter, four lignocellulose biomasses were treated with mediate oxidative torrefaction with air flow at different heating rates. The yield study showed that when applying lower heating rates, the resulted weight of char decreases. The thermal degradation curves revealed that as the heating rates slows down, the peak of the decomposition process of all lignocellulose biomasses have shifted to lower temperatures. The elemental analysis indicated that the lower heating rates could decrease the H/C ratio. The infrared spectroscopy displayed a decreasing holocellulose intensity along with the decreasing heating rates. SEM images of all treated samples showed porosity have been created in most of the biomasses even at mediate level of torrefaction. The oxidative torrefaction could be used as feedstock improvement for biomass conversion to biochar and activated carbon. In the last chapter, four species of lignocellulosic biomass have been converted to activated carbon materials with an intermediate pyrolysis process. Two pyrolysis temperatures were applied in this very process at 450 and 1000 °C to study the differences of resulted biochar and activated carbon materials. Nitrogen adsorption and desorption test, scanning electron microscope as well as Raman spectroscopy have been used to characterize the samples. The results showed that the samples from all species showed a higher specific surface area and a better porosity development at 450 °C than at 1000 °C. The SEM showed that there is sign that intermediate pyrolysis of 1000 °C could lead to the observed collapse of the pore

development. The increased $I_D/I_G$ ratios from Raman spectra of both biochar and activated carbon samples indicated that the higher pyrolysis temperature could result in the increase of amorphous portion in the carbon rich materials and the decrease of graphitization degree. Finally, Chapter 6 summarizes the major findings and results of this dissertation.

DEDICATION

I would like to dedicate this dissertation to my family for their endless understanding, love and support in my life.

ACKNOWLEDGEMENTS

I would like to express my gratefulness to my advisor and the chair of my graduate committee, Dr. Jingxin Wang, for helping me develop this research plan, for giving constant guidance on the work for past years. Without Dr. Jingxin Wang's support and instructions, I wouldn't be able to complete this dissertation work. I also would like to thank Dr. Edward Sabolsky, Dr. Shawn Grushecky, Dr. Debangsu Bhattacharyya and Dr. Jamie Schuler for providing me so much help and guidance during my research.

It has been a great pleasure to work with members in Dr. Wang's group, Yuxi Wang, Xufeng Zhang, Wanhe Hu, John Vance and Nan Nan. I really appreciate their help in past years. I am deeply grateful for having the opportunity to work with my research partner, Dr. Gunes Yakaboylu and Dr. Tugrul Yumak. During the past years, we have worked closely on details related to this dissertation. Many thanks to WVU shared research facilities staff Mrs. Gabriela Perhinschi for the elemental analysis and ICP testing. I would also like to thank Dr. Marcelo Redigolo for her help with the electron microscopy. I thank Dr. Qiang Wang for helping out with the FTIR and Raman Spectroscopy.

I would also like to take this opportunity to thank the funding agencies who have supported this work. This research was supported by Agriculture and Food Research Initiative Competitive Grant No. 2015-67021-22995 from the USDA National Institute of Food and Agriculture - "Enhancing the nanostructure of the lignocellulosic cell wall as a natural template for highly-ordered mesoporous carbons". I also acknowledge the National Science Foundation EPSCOR project - "Improving water management, treatment and recovery in oil and gas production" for providing funding for contaminants adsorption related work.

## Table of Contents

ABSTRACT ..... ii
DEDICATION ..... iv
ACKNOWLEDGEMENTS ..... v
**Chapter 1. Introduction** ..... 1
**1.1. Biomass Derived Activated Carbon** ..... 2
**1.2. Thermal Pretreatment of Biomass** ..... 3
**1.3. Activation Methods** ..... 4
**1.4. Activated Carbon for Supercapacitor Electrode** ..... 6
**1.5. Activated Carbon for Adsorption** ..... 7
**1.6. References** ..... 8
**Chapter 2. Activated Carbons by Indirect and Direct $CO_2$ Activations of Lignocellulosic Biomass for Supercapacitor Electrodes** ..... 12
**2.1. Abstract** ..... 13
**2.2. Introduction** ..... 14
**2.3. Material and Method** ..... 16
**2.3.1. Preparation of activated carbons** ..... 16
**2.3.2. Materials characterization** ..... 18
**2.3.3. Supercapacitor fabrication and electrochemical testing** ..... 19
**2.4. Results** ..... 20
**2.4.1. Process yield** ..... 20
**2.4.2. Surface area and pore structure** ..... 22
**2.4.3. Proximate and ultimate analysis** ..... 25
**2.4.4. Microstructures** ..... 27
**2.4.5. Electrochemical performance of supercapacitors** ..... 28
**2.4.6. Chemistry and surface functional groups** ..... 35
**2.4.7. Statistical Analysis** ..... 37
**2.5. Discussion** ..... 40
**2.5.1. Reaction Mechanism** ..... 40
**2.5.2. Influence of processing parameters on electrochemical performance** ..... 43
**2.5.3. Effect of surface functional groups on electrochemical performance** ..... 44
**2.6. Conclusion** ..... 49

**Chapter 3. Biomass Derived Porous Carbon Materials for Barium Removal from Shale Gas Flowback Water** ..... 56
**3.1. Abstract** ..... 57
**3.2. Introduction** ..... 58
**3.3. Material and Method** ..... 59
**3.3.1. Materials** ..... 59
**3.3.2. Preparation of Porous Carbon Materials** ..... 59
**3.3.3. $N_2$ Adsorption and Desorption** ..... 61
**3.3.4. Barium Removal Efficiency Test** ..... 61
**3.3.5. SEM and EDAX** ..... 62
**3.3.6. Statistical Analysis** ..... 62
**3.4. Results** ..... 63
**3.4.1. Processing and Yield** ..... 63
**3.4.2. $N_2$ Adsorption-desorption Isotherms and Pore Characteristics** ..... 63
**3.4.3. Barium Removal Application** ..... 67
**3.4.4. Surface Morphology and EDAX** ..... 70
**3.5. Discussion** ..... 74
**3.5.1. Surface Functional Groups and Adsorption** ..... 74
**3.5.2. Direct and Indirect KOH Activation** ..... 76
**3.5.3. Statistical analysis** ..... 78
**3.6. Conclusion** ..... 81
**3.6. References** ..... 83
**Chapter 4. Chemical and Structural Variation of Lignocellulosic Biomass during Oxidative Torrefaction** ..... 88
**4.1. Abstract** ..... 89
**4.2. Introduction** ..... 89
**4.3. Material and Method** ..... 92
**4.3.1. Materials** ..... 92
**4.3.2. Torrefaction Process** ..... 93
**4.3.3 Thermogravimetric Analysis (TGA)** ..... 93
**4.3.4. Elemental Analysis** ..... 93
**4.3.5. Fourier-transform Infrared Spectroscopy (FTIR)** ..... 94
**4.3.6. Scanning Electron Microscope (SEM)** ..... 94
**4.4. Results** ..... 94

**4.4.1. Yield by Different Heating Rates** ..... 94
**4.4.2. Thermo-gravimetrical Analysis (TGA)** ..... 95
**4.4.3. Elemental Analysis** ..... 97
**4.4.4. Surface Functional Groups of Torrefied Biomass.** ..... 98
**4.4.5. Morphology** ..... 101
**4.5. Discussion** ..... 104
**4.5.1. Effect of oxidative torrefaction** ..... 104
**4.5.2. Surface chemistry and pore development** ..... 104
**4.6. Conclusion** ..... 105
**4.7. References** ..... 107
**Chapter 5. Effect of Intermediate Pyrolysis Temperature for Lignocellulosic Biochar on the Physicochemical Properties of Eventual Activated Carbon** ..... 111
**5.1. Abstract** ..... 112
**5.2. Introduction** ..... 112
**5.3. Material and Method** ..... 115
**5.3.1. Materials** ..... 115
**5.3.2. Processing** ..... 115
**5.3.3. $N_2$ Adsorption and Desorption NLDFT Pore Size Distribution** ..... 116
**5.3.4. Scanning Electron Microscope (SEM)** ..... 116
**5.3.5. Raman Spectroscopy** ..... 116
**5.4. Results** ..... 117
**5.4.1. Yield** ..... 117
**5.4.2. $N_2$ Adsorption and Desorption** ..... 118
**5.4.3. NLDFT Pore Size Distribution** ..... 120
**5.4.4. Morphology** ..... 122
**5.4.5. Raman Spectroscopy** ..... 124
**5.5. Discussion** ..... 126
**5.5.1. Effect of intermediate pyrolysis temperature on porosity** ..... 126
**5.5.2. Effect of intermediate pyrolysis temperature on pore size and chemical structure** ..... 127
**5.6. Conclusion** ..... 127
**5.7. References** ..... 129
**Chapter 6. Summary** ..... 133

## LIST OF FIGURES

Figure 2.1. The porosity characterization of activated carbon samples: the adsorption and desorption curves of direct activated carbons (a) and indirectly activated carbons (b); the pore size distribution by NLDFT for direct activation samples (c) and indirect activation samples (d). ..... 23
Figure 2.2. SEM characterization of activated carbons by direct activation..... 28
Figure 2.3. SEM characterization of activated carbons by indirect activation..... 28
Figure 2. 4. Charge-discharge tests of direct activation samples under constant current density of 100 mA/g: (a) BAC-700-30-D, (b) BAC-700-60-D, (c) BAC-750-30-D, (d) BAC-750-60-D, (e) BAC-800-30-D, and (f) BAC-800-60-D..... 30
Figure 2. 5. Charge-discharge of indirect activation samples under constant current density of 100 mA/g: (a) BAC-250-I, (b) BAC-350-I, (c) BAC-450-I, (d) BAC-550-I and (e) BAC-750-I. ..... 30
Figure 2. 6. Self-discharge tests of direct activation samples under constant current density of 100 mA/g and an hour rest period: (a) BAC-700-30-D, (b) BAC-700-60-D, (c) BAC-750-30-D, (d) BAC-750-60-D, (e) BAC-800-30-D, and (f) BAC-800-60-D. ..... 31
Figure 2. 7. Self-discharge tests of indirect activation samples under constant current density of 100 mA/g and an hour rest period: (a) BAC-250-I, (b) BAC-350-I, (c) BAC-450-I, (d) BAC-550-I, and (e) BAC-750-I. ..... 32
Figure 2. 8. (a-b) Specific capacitances of activated biomass and biochar samples as a function of current density, (c-d) specific capacitances of activated biomass and biochar samples as a function of number of cycles (cycling stability) over 1000 cycles at 100 mA/g constant current density..... 34
Figure 2. 9. XPS survey spectra of activated carbons prepared by (a) direct activation and (b) indirect activation..... 37
Figure 2. 10. Raman spectra of activated carbons prepared by direct activation (a) and indirect activation (b). ..... 37
Figure 2. 11. Deconvolution of C1s peaks of all samples: (a) BAC-350-I, (b) BAC-450-I, (c) BAC-550-I, (d) BAC-700-60-D, (e) BAC-750-60-D, (f) BAC-800-30-D, and (g) BAC-800-60-D..... 46
Figure 2. 12. Deconvolution of O1s peaks of all samples: (a) BAC-350-I, (b) BAC-450-I, (c) BAC-550-I, (d) BAC-700-60-D, (e) BAC-750-60-D, (f) BAC-800-30-D, and (g) BAC-800-60-D..... 47

Figure 3. 1. The adsorption-desorption isotherms of porous carbon materials: (a) BC, (b) BPC-1, (c) BPC-2, and (d) all three porous carbon materials with different adsorbed amount levels. ..... 65
Figure 3. 2. The pore size distribution of different porous carbon materials: (a) BC, (b) BPC-1, (c) BPC-2, and (d) comparison of PSD for three porous carbons..... 67
Figure 3. 3. Influence of porous carbon type and load on Ba removal. ..... 68
Figure 3. 4 SEM of BC: (a) and (b) before adsorption; (c) and (d) after adsorption. ..... 71
Figure 3. 5 SEM of BPC-1: (a) and (b) before adsorption; (c) and (d) after adsorption..... 72
Figure 3. 6. SEM of BPC-02: (a) and (b) before adsorption; (c) and (d) after adsorption. ..... 73
Figure 3. 7. EDAX of three porous carbon materials before and after adsorption of Ba from flowback water. ..... 74
Figure 3. 8 Typical oxygen functional groups found on activated carbon. ..... 76

Figure 4. 1. TGA of four lignocellulosic biomasses. 96
Figure 4. 2. FTIR analysis of switchgrass biomass under torrefaction treatment with different heating rates. 100
Figure 4. 3. FTIR analysis of hybrid willow biomass under torrefaction treatment with different heating rates. 100
Figure 4. 4. FTIR analysis of miscanthus grass and eastern white pine. 101
Figure 4. 5. SEM image of two grass species after torrefaction at 250 °C with heating rates of 5 and 0.5 °C/min. 102
Figure 4. 6. SEM image of two wood species after torrefaction at 250 °C with heating rates of 5 and 0.5 °C/min. 103

Figure 5. 1. The adsorption and desorption isotherms of activated carbon from char prepared at 450 and 1000 °C. 119
Figure 5. 2. Pore size distribution of resulted activated carbon by NLDFT method. 120
Figure 5. 3. SEM image of eastern white pine biochar and activated carbon. 122
Figure 5. 4. SEM image of switchgrass biochar and activated carbon. 123
Figure 5. 5. Raman spectroscopy of both biochar and resulted activated carbon. 124

## LIST OF TABLES

Table 2.1 The BAC yield by indirect (label with -I) and direct activation (label with -D)..... 21
Table 2.2 The porosity of activated carbon materials prepared by both methods. ..... 24
Table 2. 3 Proximate and ultimate analysis of hybrid willow biomass, biochar and activated carbons. .... 26
Table 2. 4 Descriptive statistics of IR drop values of direct activation samples. ..... 38
Table 2. 5 ANOVA of IR drop values of direct activation samples. ..... 39
Table 2. 6 Descriptive Statistics of IR drop values of indirect activation samples. ..... 39
Table 2. 7 ANOVA of IR drop values of direct activation samples. ..... 40
Table 2. 8 The kinetics of activation process at different temperature ..... 43
Table 2. 9 Deconvolution results of C1s peaks of all samples. ..... 49
Table 2. 10 Deconvolution results of O1s peaks of all samples. ..... 49

Table 3. 1. Yields of char and activation carbon production. ..... 63
Table 3. 2. The pore characterization of three porous carbons. ..... 65
Table 3. 3 Ba Reduction at different pH of flowback water. ..... 69
Table 3. 4 Ba reduction at different adsorption time. ..... 69
Table 3. 5 ANOVA of Ba concentration (mg/L) after adsorption considering treatment and treatment interaction with carbon loading (R-square=0.76)..... 80
Table 3. 6 Descriptive statistics of Ba concentration (mg/L) after treatments with different carbon types. ..... 80
Table 3. 7 Descriptive statistics of Ba concentration (mg/L) after treatments with different carbon type at different carbon loading. ..... 81

Table 4. 1. Yield by species after air torrefaction under different ramping rates. ..... 95
Table 4. 2. Pyrolysis parameters of four species by TGA. ..... 97
Table 4. 3. Elemental analysis of biomass treated with three different heating rates. ..... 98

Table 5. 1. The yields of activated carbon from char prepared at 450 and 1000 °C. ..... 117
Table 5. 2. Porosity parameters of activated carbon from char prepared at 450 and 1000 °C. ..... 119
Table 5. 3. The pore size distribution parameters by NLDFT method. ..... 121
Table 5. 4 .Raman spectroscopy parameters of biochar and resulted activated carbon. ..... 125

## Chapter 1. Introduction

Lignocellulosic biomass commonly refers to the non-edible plant-based materials that consist of primarily cellulose, hemicellulose and lignin. It also has a limited amount of small organic molecules that are extractives. Typical lignocellulosic biomass are agriculture residues, forest residues and energy crops. These materials are abundant, renewable, environmentally friendly and affordable. There are many pathways to utilize the lignocellulosic biomass rsources. Traditionally, lignocellulosic biomass was directly burnt to produce heat and was a critical energy source for human society. As the technology advances, the lignocellulosic biomass was utilized in many new ways. Generally, the conversion of lignocellulosic biomass could be classified into three types: thermal, chemical and biological (Küçük et al. 1997). Pellets made from lignocellulosic biomass could be used as a fuel for heat and power generation (Nunes et al. 2014, Pirraglia et al. 2013). Lignocellulosic biomass could be converted to renewable chemicals which can later be used in many chemical industries (Zhou et al. 2011). Gasification of lignocellulosic biomass can produce syngas which can be used for energy and fuel production (Kirubakaran et al. 2009).

Lignocellulosic biomass has been utilized for the production of activated carbon. Activated carbon is widely used in water treatment, air quality control and energy storage. It is a carbonaceous, highly porous, and relatively light material. It is usually made from a carbon precursor such as coal, biomass, and organic chemicals (Chingombe et al. 2005, Ioannidou and Zabaniotou 2007, Chen et al. 2015).

### 1.1. Biomass Derived Activated Carbon

Activated carbon can be prepared from coal or biomass. Compared to coal, biomass is considered as possible carbon neutral, renewable, lost cost and abundant feedstock to produce activated carbon. There are many types of biomass, including forest residues, agricultural residues, and animal residues, etc. With these different sources, many studies have been reported using biomass to produce activated carbon.

Wood, particularly, has a natural porous structure which could be a great advantage for producing activated carbon which also has a focus on porosity (Greil et al. 1998, Gibson 2012). Forest residue as a suitable lignocellulosic biomass source is very promising to be used for the manufacturing of activated carbon. During logging operations, the stem wood (log) is usually harvested for the large value part of a tree while the crown, branches, stump, as well as bark are commonly left dry and used as fuel later, which is considered an underutilized resource in forest operations (Wang et al. 2017).

Theoretically, wood has many natural structures which could form pores after pyrolysis. In softwood, pore forming structure includes resin canals, longitudinal tracheids (20-70μm) and radial ray tracheids, which could be seen by human eyes with simple magnification tools. Smaller pore forming structure includes parenchyma cells and pit. In hardwood, major pore forming structures are vessels, tracheid, ray cells, perforation plates and pits.

Grasses are natural plants which could produce a large amount of biomass. In the Northeastern United States, switchgrass (*Panicum virgatum*), a perennial warm season bunchgrass, is one of the dominant species. It is primarily used for soil conservation, forage production, game cover, fiber, heat production and more recently as a biomass feedstock for ethanol and butanol. *Miscanthus x giganteus* is another species which could provide a large amount of biomass. It is a perennial grass

hybrid of *miscanthus sinensis* and *miscanthus sacchariflorus*. This grass is full sun plant which can grow 8-12 ft (240-360 cm) tall each year. The grass also has a porous structure which could be utilized to prepare porous carbon products. For examples, the microstructure of miscanthus grass stalk shows countless natural pores around 0.2 μm (Klimek et al. 2018).

There are many studies related to other biomass sources. To fabricate activated carbon, palm and coconut shell as sources were compared and the results indicated that more micro- and meso-pores were developed in palm shell derived carbon (Daud and Ali, 2004). Another study prepared activated carbon from bamboo and showed that the resulting micropores has a size between 0.33 and 0.82 nm, which largely contributed to the adsorption of $CO_2$ in the application (Wei et al. 2012). Rice husk and bagasse were treated with one-step chemical activation and the derived activated carbon has a specific surface area value of 750 and 674 $m^2/g$, respectively (Kalderis et al. 2008).

### 1.2. Thermal Pretreatment of Biomass

Torrefaction is a common thermal pretreatment used to upgrade the solid biomass by heating the raw biomass in an inert atmosphere at 200-300 °C (Tran et al. 2013). Like pyrolysis process, N2 is the most commonly used gas agent for the torrefaction process. Other gases may include Ar and Kr. Torrefaction has a similar condition when compared to pyrolysis except for the different resident temperature. Therefore, torrefaction is sometimes called mild pyrolysis.

Hygroscopicity, low bulk density and heating value, as well as high water content are some drawbacks of raw biomass when it is used as fuel (Amer et al. 2019, Chen et al. 20 15). The

torrefaction could be used to improve energy density, hydrophobicity, grindability and gain lower water content as well as lower heteroatom to carbon ratio (Van der Stelt et al. 2011).

The torrefaction process could be classified as light (200~235 °C), mediate (235~275 °C) and severe (275~300 °C) (Chen et al. 2011). The light level will vent low molecular weight volatiles along with the moisture. Hemicellulose will be degraded to a certain extent while cellulose and lignin barely degraded (Rousset et al. 2011). Mild torrefaction leads to substantial depletion of hemicellulose and cellulose is also degraded to a certain extent. At severe level, hemicellulose is largely decomposed, and cellulose was dehydrated but not entering fragmentation yet. Due to higher thermal stability, lignin consumption at this stage is relatively low. The thermal degradation is usually finished in less than 1 hour during torrefaction. The other factor during the process is the residence time, which has less influence when compared to the temperature (Chen et al. 2011).

### 1.3. Activation Methods

The activation process is to develop the pore network in carbon materials. The activation process of biomass typically includes two types: physical activation and chemical activation. The physical activation is to carbonize the precursor in an inert gas atmosphere to remove volatiles and obtain char. Then the char was activated in the atmosphere of suitable oxidizing gasifying agents such as $O_2$, $CO_2$ and steam (Sevilla and Mokaya. 2014). The activation process is also to develop porosity and it is usually operated in the temperature range of 600-1200 °C. The physical activation reactions are listed here according to different activation agent.

The typical reactions when oxygen ($O_2$) is the activation agent:

$$C + O_2 \rightarrow CO_2$$

$$2C + O_2 \rightarrow 2CO$$

The typical reactions when carbon dioxide ($CO_2$) is the activation agent:

$$C + CO_2 \rightarrow 2CO$$

The typical reactions when steam ($H_2O$) is the activation agent:

$$C + H_2O \rightarrow CO + H_2$$

$$CO + H_2O \rightarrow CO_2 + H_2$$

The chemical activation is typically operated by mixing the precursor with the activation agents such as KOH, $H_3PO_4$, and $ZnCl_2$ then carbonized at the temperature range of 400-900 °C. The chemical activation could lead to a higher specific area up to 2000-3000 $m^2/g$ as well as a larger pore volume, when compared with physical activation (Wang and Kaskel 2012). Generally, the chemical activation has many advantages such as lower activation temperature and less activation time that resulting in less energy consumption. It also has higher yields of final activated carbon than physical activation. However, the chemical activation has some drawbacks. It is usually corrosive to the equipment and requires further operation to clean up the end product. KOH, among various chemical agents for activation, is widely used due to that it can fabricate activated carbon with defined micropore size distribution, high microporous volume and specific surface area. The pore structure and elemental composition depend on the processing parameters such as mass ratio of KOH/precursor, activation temperature and time. The initial precursor could also determine the pore and elements of final activated carbon.

The mechanism of potassium hydroxide as a chemical activation agent is still not clear. The reason is that the complicated and countless operational parameters and not unified reactivity of feedstock (Jia and Kaskel 2012). It is generally believed that the activation begins with solid-solid phase then solid-liquid phase, involving the K reduction, C oxidation and secondary reactions to form

intermediates (Otowa et al. 1993, Lozano-Castello et al. 2007). The gas phase product has hydrogen, water vaper, carbon monoxide and carbon dioxide. The solid phase product includes $K_2O$ and $K_2CO_3$. The activation process could be described by following equations.

$$2KOH \rightarrow K_2O + H_2O$$

$$C + H_2O \rightarrow CO + H_2$$

$$CO + H_2O \rightarrow CO_2 + H_2$$

$$CO_2 + K_2O \rightarrow K_2CO_3$$

$$6KOH + 2C \rightarrow 2K + 3H_2 + 2K_2CO_3$$

### 1.4. Activated Carbon for Supercapacitor Electrode

There are increasing studies regarding using biomass to prepare activated carbon for supercapacitor electrode applications. Activated carbon from peanut shell and rice husk were prepared with one-stage $ZnCl_2$ activation with the help of microwave heating (He et al. 2013). The results show that the specific capacitance has ranged from 50 to 250 F/g and a high energy density as well as power density than conventional heating.

Activated carbon derived from the leaves of willow tree has been fabricated using one-stage zinc chloride activation and displayed a great pore volume of 0.66 $cm^3/g$, which was later assembled into supercapacitor electrode and characterized with a relatively high capacitance of 216 F/g as well as a 97% retention rate after 1000 cycles (Liu et al. 2016). Stem bark of broussonetia papyrifera was converted to N doped carbon by KOH activation (Wei et al. 2015). The specific

surface area was 1212 $m^2$/g. The average pore size was 3.8 nm. The carbon had a great capacitance of 320 F/g at 0.5 A/g and showed an excellent retention because of N functional groups.

### 1.5. Activated Carbon for Adsorption

In shale gas production process, hydraulic fracking water became a concerning issue in the last decade. The used water contains metal ions, organics, suspended solids, oil and grease which will make the water non-reusable. The industrial side is searching for better solutions to solve the water recycling problem since according to the current regulations. The fracking water will be injected to an even deeper formation in earth.

Fertilizer waste was reported being converted to carbon and applied to adsorb Hg (II) from wastewater (Mohan et al. 2011). The study indicated that the concentration of adsorbate, the properties of the adsorbent are key parameters in the adsorption process. Acidity, temperature, initial Hg concentration, carbon size, and carbon loading were further investigated. The report indicated that the mechanism of adsorption could be explained with film diffusion when the initial concentration is low while with particle diffusion when the initial concentration is high.

Tetrabutyl ammonium iodide and sodium diethyl dithiocarbamate modified activated carbon was reported to remove toxic ions, copper zinc, chromium and cyanide (Monser and Adhoum 2002). The former could effectively remove cyanide five times better than non-treated carbon, four times on copper, four times on zinc and twice on chromium. Sulfur is a typical agent to modify activated carbon by static and column methods to improve the Pb (II) adsorption from water.

There appears necessity to further examine and assess biomass derived activated carbon in energy storage and water treatment applications.

## 1.6. References

Chen, W.H. and Kuo, P.C., 2011. Torrefaction and co-torrefaction characterization of hemicellulose, cellulose and lignin as well as torrefaction of some basic constituents in biomass. Energy, 36(2), pp.803-811.

Chen, X., Li, Z., Wei, L., Li, X., Liu, S. and Gu, J., 2015. Fabrication of hierarchical cabbage-like carbonaceous materials by one-step cobalt-assisted hydrothermal carbonization of furfural. Microporous and Mesoporous Materials, 210, pp.149-160.

Chen, W.H., Peng, J. and Bi, X.T., 2015. A state-of-the-art review of biomass torrefaction, densification and applications. Renewable and Sustainable Energy Reviews, 44, pp.847-866.

Chingombe, P., Saha, B. and Wakeman, R.J., 2005. Surface modification and characterisation of a coal-based activated carbon. Carbon, 43(15), pp.3132-3143.

Daud, W.M.A.W. and Ali, W.S.W., 2004. Comparison on pore development of activated carbon produced from palm shell and coconut shell. Bioresource technology, 93(1), pp.63-69.

Gibson, L.J., 2012. The hierarchical structure and mechanics of plant materials. Journal of the royal society interface, 9(76), pp.2749-2766.

Greil, P., Lifka, T. and Kaindl, A., 1998. Biomorphic cellular silicon carbide ceramics from wood: I. Processing and microstructure. Journal of the European Ceramic Society, 18(14), pp.1961-1973.

He, X., Ling, P., Qiu, J., Yu, M., Zhang, X., Yu, C. and Zheng, M., 2013. Efficient preparation of biomass-based mesoporous carbons for supercapacitors with both high energy density and high power density. Journal of Power Sources, 240, pp.109-113.

Kalderis, D., Bethanis, S., Paraskeva, P. and Diamadopoulos, E., 2008. Production of activated carbon from bagasse and rice husk by a single-stage chemical activation method at low retention times. Bioresource technology, 99(15), pp.6809-6816.

Klímek, P., Wimmer, R., Meinlschmidt, P. and Kúdela, J., 2018. Utilizing Miscanthus stalks as raw material for particleboards. Industrial crops and products, 111, pp.270-276.

Kirubakaran, V., Sivaramakrishnan, V., Nalini, R., Sekar, T., Premalatha, M. and Subramanian, P., 2009. A review on gasification of biomass. Renewable and Sustainable Energy Reviews, 13(1), pp.179-186.

Küçük, M.M. and Demirbaş, A., 1997. Biomass conversion processes. Energy Conversion and Management, 38(2), pp.151-165.

Liu, Y., Wang, Y., Zhang, G., Liu, W., Wang, D. and Dong, Y., 2016. Preparation of activated carbon from willow leaves and evaluation in electric double-layer capacitors. Materials Letters, 176, pp.60-63.

Lozano-Castello, D., Calo, J.M., Cazorla-Amoros, D. and Linares-Solano, A., 2007. Carbon activation with KOH as explored by temperature programmed techniques, and the effects of hydrogen. Carbon, 45(13), pp.2529-2536.

Mohan, D., Gupta, V.K., Srivastava, S.K. and Chander, S., 2001. Kinetics of mercury adsorption from wastewater using activated carbon derived from fertilizer waste. Colloids and Surfaces A: Physicochemical and Engineering Aspects, 177(2-3), pp.169-181.

Monser, L. and Adhoum, N., 2002. Modified activated carbon for the removal of copper, zinc, chromium and cyanide from wastewater. Separation and purification technology, 26(2-3), pp.137-146.

Nunes, L.J.R., Matias, J.C.O. and Catalão, J.P.S., 2014. A review on torrefied biomass pellets as a sustainable alternative to coal in power generation. Renewable and Sustainable Energy Reviews, 40, pp.153-160.

Otowa, T., Tanibata, R. and Itoh, M., 1993. Production and adsorption characteristics of MAXSORB: high-surface-area active carbon. Gas separation & purification, 7(4), pp.241-245.

Pirraglia, A., Gonzalez, R., Saloni, D. and Denig, J., 2013. Technical and economic assessment for the production of torrefied ligno-cellulosic biomass pellets in the US. Energy Conversion and Management, 66, pp.153-164.

Rousset, P., Aguiar, C., Labbé, N. and Commandré, J.M., 2011. Enhancing the combustible properties of bamboo by torrefaction. Bioresource Technology, 102(17), pp.8225-8231.

Sevilla, M. and Mokaya, R., 2014. Energy storage applications of activated carbons: supercapacitors and hydrogen storage. Energy & Environmental Science, 7(4), pp.1250-1280.

Tran, K.Q., Luo, X., Seisenbaeva, G. and Jirjis, R., 2013. Stump torrefaction for bioenergy application. Applied energy, 112, pp.539-546.

Van der Stelt, M.J.C., Gerhauser, H., Kiel, J.H.A. and Ptasinski, K.J., 2011. Biomass upgrading by torrefaction for the production of biofuels: A review. Biomass and bioenergy, 35(9), pp.3748-3762.

Wang, L., Barta-Rajnai, E., Skreiberg, Ø., Khalil, R., Czégény, Z., Jakab, E., Barta, Z. and Grønli, M., 2017. Impact of torrefaction on woody biomass properties. Energy Procedia, 105, pp.1149-1154.

Wang, J. and Kaskel, S., 2012. KOH activation of carbon-based materials for energy storage. Journal of Materials Chemistry, 22(45), pp.23710-23725.

Wei, H., Deng, S., Hu, B., Chen, Z., Wang, B., Huang, J. and Yu, G., 2012. Granular bamboo‐derived activated carbon for high CO2 adsorption: the dominant role of narrow micropores. ChemSusChem, 5(12), pp.2354-2360.

Wei, T., Wei, X., Gao, Y. and Li, H., 2015. Large scale production of biomass-derived nitrogen-doped porous carbon materials for supercapacitors. Electrochimica Acta, 169, pp.186-194.

Zhou, C.H., Xia, X., Lin, C.X., Tong, D.S. and Beltramini, J., 2011. Catalytic conversion of lignocellulosic biomass to fine chemicals and fuels. Chemical Society Reviews, 40(11), pp.5588-5617.

# Chapter 2. Activated Carbons by Indirect and Direct $CO_2$ Activations of Lignocellulosic Biomass for Supercapacitor Electrodes

## 2.1. Abstract

Lignocellulosic biomass feedstock was converted into hierarchical porous carbon by using physical activation technique under carbon dioxide environment. Both direct and indirect $CO_2$ activation routes were followed to investigate the effect of processing parameters and the kinetics of the activation. The porosity, surface chemistry, and morphology of the activated carbons were characterized in addition to their proximate and ultimate analyses. This was followed by the preparation of the carbon electrodes, and fabrication and electrochemical testing of their supercapacitor cells. The results showed dominant microporous structure along with minor larger pores for the activated carbons prepared via both direct and indirect activation. Along with the preserved pore structure of the biomass precursor, engineered pore structure was achieved, which can be highly beneficial for the supercapacitors with respect to the transportation and storage of ions. The morphological analysis revealed the tortuous porous structure. The maximum specific capacitances of 80.9 and 92.7 F/g at the current density of 100 mA/g were achieved after direct and indirect activation routes, respectively. The surface functional groups were found to play a significant role in the resultant electrochemical performance of the supercapacitors.

## 2.2. Introduction

Lignocellulosic biomass is a plant-based material not used for food purpose, which is mainly composed of cellulose, hemicellulose and lignin. As a source for energy, it can be used as a feedstock to produce heat, such as firewood and pellets, or be converted into various biofuels (Poddar et al. 2014, Binder and Raines 2009). In addition, it can be utilized to prepare renewable materials, such as, cellulose and bio-adhesive (Brinchi et al. 2013, Hoong et al. 2011). The conversion of biomass into biofuels and byproducts can be classified into three major pathways as thermal, chemical and biochemical. Woody biomass is still a major component of lignocellulosic biomass. Typical woody biomass includes logging and mill residues, such as, wood shavings and sawdust. Hybrid willow is a shrub woody crop, which is an alternative energy source as promoted in the recent years in Northeast United States. It is a short rotation tree that can grow relatively fast and be harvested in three years. Therefore, there is an increasing interest on the hybrid willow in recent years (Tarves et al. 2017, Volk et al. 2016).

Activated carbon is usually made from coconut shell, peat, wood, coal, bamboo, and organic chemicals (Guo et al. 2009, Mi et al. 2018, and Chen et al. 2015). It is a carbonaceous and highly porous adsorptive material, which mainly contains carbon, with minor contents of oxygen and hydrogen, and a limited amount of nitrogen and sulfur (Tay el al. 2009). The activated carbon is an amorphous material, which typically has a well-organized pore network with a dominant microporous or mesoporous structure. Lignocellulosic biomass is a highly preferred precursor for the production of porous activated carbon materials due to its natural interconnected pore network (Dutta et al. 2014). The vertical and horizontal pores within the lignocellulosic biomass are usually connected with pits and perforation plates. These pore networks play a critical role in plant nutritional transportation. In other words, they provide the capability of transporting nutrition

elements including the inorganic ions. Therefore, the carbonization of the lignocellulosic biomass feedstocks into engineered, hierarchically porous carbon structures is trending in recent years (Abioye and Ani 2015). Due to their advantage for energy storage on the basis of the ion storage and diffusion, they are highly suitable for the electrochemical double layer capacitors (EDLCs) as ususally referred to supercapacitors. The piling of pure electrostatic charge on the interface between electrode and electrolyte provides the capacitance of the supercapacitor, which is mainly dictated by the specific surface area of carbon electrode accessible to the electrolyte ions (Wang et al. 2015). Along with the pores and surface area, the surface functional groups of the carbon materials are also critical to the adsorption behavior since they can serve as electron donors or acceptors for the targeted ions (Wang et al. 2013).

The thermochemical conversion process typically involves one-step or two-step carbonization. In an one-step process, biomass source is converted into porous carbon material by heating to a certain temperature range (600°-900°C) either in an inert atmosphere in the presence of a chemical activating agent or in an activating gas environment, such as, steam or carbon dioxide (Chang et al. 2000). Two-stage carbonization process usually refers to an initial pyrolysis process to convert biomass to biochar, which is followed by a chemical or physical activation process (Zhang et al. 2004). The physical activation has three major reagents, which are air, steam and carbon dioxide ($CO_2$). The steam and $CO_2$ typically have an activation temperature ranging from 700° to 1000°C, whereas the air has a lower temperature of activation at the range of 350°-550°C (Lu and Zhao 2017, Olivares-Marin et al. 2012). The physical activation method is widely considered to be a cost-effective and efficient way to produce porous carbon materials (Bouchelta et al. 2008). More importantly, it is less corrosive when compared to the chemical activation method. The widely used chemical activation reagents, such as KOH and $ZnCl_2$, are highly corrosive, and they can

react directly with the furnace components used in such processes (Hayachi et al. 2002). In addition, the physical activation route (e.g. $CO_2$) could be highly time efficient, since it typically does not require an extensive washing process afterwards. The inorganic release took place along with the chemical activation route could also lead to the environmental pollution, which could be avoided by using the physical activation instead (Chang et al. 2000). The $CO_2$ activation can promote the formation of meso/microporous structure and preserve the natural interconnected pore network of the biomass, compared to the chemical activation that may destruct or collapse the pore structure. The main objective of this study is to investigate the effect of direct and indirect activation on the physical and chemical properties of activated carbon being applied as supercapacitor electrode. The temperature and residence time of direct activation and biochar char preparation time will be studied to determine the better preparation parameter for the final activated carbon with better properties. The electrochemical performance will be evaluated, and determinant properties of activated carbon will be discussed in this work.

## 2.3. Material and Method

### 2.3.1. Preparation of activated carbons

The hybrid willow biomass was provided by Genova Agricultural Experiment Station, Cornell University. The hybrid willow chips were milled with 1 mm sieve to obtain the biomass particles. The milling was carried out with a power cutting mill (Pulverisette 25, Fritsch, Germany). The gas cylinders, both $CO_2$ and $N_2$, were all purchased from the Matheson Tri-Gas Inc (Montgomeryville PA, USA).

The direct activation process refers to one-step conversion of the biomass into an activated carbon using carbon dioxide ($CO_2$) as an activating environment. The carbonization took place in a tube

furnace with a quartz tube. An alumina combustion boat containing 10 g of the biomass was placed in tube furnace and heated to 700°C, 750°C and 800°C under continuous $CO_2$ flow (20 sccm). The samples were held at the maximum temperature for 30-60 min. The heating rate was fixed at 10°C/min for all experiments. The biomass was thermally degraded as similar to the conventional pyrolysis, but at higher temperatures. When the physical activation temperature was above 700°C, the activation process took place as termed as Boudouard Reaction (Mathieu and Dubuisson, 2002). In the indirect activation route, the biomass-derived char (biochar) was prepared by low temperature pyrolysis, which was followed by its physical activation using carbon dioxide. The initial pyrolysis experiments were conducted at 250°, 350°, 450°, 550° and 750°C for a period of 30 min under nitrogen flow. Similar to the direct $CO_2$ activation route, 10 g of biomass samples were processed. The heating rate during pyrolysis experiments was set as 10°C/min. The yields of the biochar samples were recorded after pyrolysis. In the second step, the biochar samples were similarly activated at 800°C for 60 min under $CO_2$ atmosphere (20 sccm). The heating rate during the activation process was set to 10°C/min. The yields of the activated carbons were also recorded for further comparison. The direct activation samples have been labelled in a temperature and time fashion. For example, in the label of BAC-700-30-D, BAC refers to biomass derived activated carbon. 700 means the activation temperature. 30 means the sample being activated for 30 minutes. D means the sample being prepared by direct activation. The indirect activation samples have been labelled in a temperature only manner. For instance, in the label of BAC-450-I, BAC still refers to biomass derived activated carbon. 450 is the pyrolysis temperature for the biochar. The symbol I means that the sample being prepared by indirect activation method.

### 2.3.2. Materials characterization

A Micromeritics ASAP2020 surface area analyzer (Micromeritics Corp., Norcross GA, USA) was used for the $N_2$ physisorption tests that were conducted at 77K. The samples were degassed at 105°C for 24 h before these measurements. The Brunauer-Emmett-Teller (BET) specific surface area, total pore volume (single point adsorption), volume of micropores (t-plot) and adsorption average pore width (BET) were recorded. Besides, the pore size distributions were calculated from the adsorption-desorption isotherms using the non-local density functional theory (NLDFT). The calculation was conducted using SAIEUS program by Micromeritics Instrument Corp. (Norcross, GA). Afterwards, the proximate and ultimate analyses were performed. Four samples (5 g for each), which are HW-0 (raw biomass), BC-450, BAC-800-60-D and BAC-450-I, were analyzed by these techniques. The testing was carried out by the Ultimate and Proximate Analysis for coal at standard laboratories. The proximate analyzer was conducted with a TGA 701 instrument (LECO Corp., St. Joseph, MI). The ultimate analysis was conducted with a Flash EA 1112 instrument (ThermoQuest). The proximate analysis reported the moisture content, volatiles, ash content and fix carbon, while the ultimate analysis provided the elemental composition, such as C, H, N, and S. The oxygen content was calculated based on the recorded weight percentages of the four elements. Furthermore, the as-prepared activated carbon materials were imaged from a scanning electron microscope (SEM, Hitachi S-4700) for their microstructural evaluation. X-ray photoelectron spectroscopy (XPS, Physical Electronics, PHI 5000 VersaProbe, Chanhassen MN, USA) was utilized to characterize the surface chemistry and functional groups of the as-prepared activated carbons. The XPS analyses were carried out under a focused monochromatized Al-Kα radiation (1486.6 eV). All peaks were plotted between spectral ranging from 0-1200 eV. Lastly,

Raman spectrometer (Renishaw InVia Raman, New Mills, UK) with 532 nm Ar laser excitation was applied to examine the structural chemistry of the activated carbons.

### 2.3.3. Supercapacitor fabrication and electrochemical testing

The electrode inks were prepared by mixing the as-prepared activated carbon powders with polyvinylidene difluoride (PVDF, Alfa Aesar) and carbon black (CB, acetylene, 75 $m^2/g$, Alfa Aesar) with a set ratio of 85:10:5 (AC:PVDF:CB) by mass. The PVDF acts as a binder, while the carbon black is a conductive enhancement agent. N-methyl-2-pyrrolidone (NMP, Alfa Aesar) was added as a solvent, and these mixtures were roll-milled for 24 h. After achieving homogeneous activated carbon electrode inks, they were casted on a pre-cleaned stainless-steel sheet using a doctor blade. The average thickness of these casts was recorded as 0.61 mm. The electrodes were initially kept at room temperature for drying, which was followed by a second-step drying in a vacuum oven at nearly 60°C. The final electrodes in 13 mm diameter were obtained using a steel punch. The electrodes were then soaked in 6 M KOH solution (electrolyte) for 24 h before being assembled. The standard CR2032 coin cell packaging (MTI, Richmond CA, USA) was adopted to assemble electrode. A typical symmetrical supercapacitor cell includes two activated carbon electrodes, a Nafion separator (NR-212, 15 mm diameter, Ion Power Inc., New Castle DE, USA), 6 M KOH electrolyte and current collectors (stainless steel). Prior to assembly, similar to the activated carbon electrodes, Nafion separators were also immersed in 6 M KOH electrolyte. The electrochemical properties were tested with an 8-channel capacitor/battery analyzer (MTI). The voltage applied was ranging from 0.1 to 1.0 V. The current density of 100 mA/g was adopted for the constant charge and discharge, as well as, self-discharge tests, for up to 1000 cycles. Further charge/discharge measurements were also tested at the current density range of 0.05-0.15 A/g for a thorough estimation of their performance. Following these tests, the specific capacitance ($C_s$) of

the activated carbon electrodes were calculated from their respective discharge curves using the Eq. (1) below.

$$C_s = 2\frac{I}{m}\frac{\Delta t}{\Delta V} \quad (1)$$

In this equation, $I$, $\Delta t$, $m$, and $\Delta V$ refer to the constant discharge current, discharge time, average mass of a single dry activated carbon electrode, and voltage change during discharge process, respectively (Chen et al. 2013). The rapid potential drops (IR drop) at the beginning of the discharge curves were not included into these calculations (Zhang et al. 2012).

### 2.4. Results

#### 2.4.1. Process yield

The yields of biochar samples obtained after pyrolysis at different temperatures (250°-750°C) are listed in Table 2.1. With increasing temperature from 250° to 350°C, it is evident that the yield of biochar decreased from 90.6 to 38.4%. This is mainly due to the degradation of hemicellulose, as well as, a very limited contents of cellulose and lignin. The mass loss after 450°C is typically due to the degradation of lignin (Yang et al. 2007). After pyrolysis at a higher temperature (750°C) for 30 min, the yield of biomass reduced to 23.6%. As presented in Table 2.1, the biochar yields highly decreased with increasing pyrolysis temperature. In the second step of the indirect activation route, the biochar samples were activated at 800°C for 60 min under carbon dioxide atmosphere. The yield of the activated carbons (ACs) obtained after the indirect activation decreased, when the initial pyrolysis temperature was in the range of 250°-450°C. However, the yield relatively increased for the activated carbon obtained after initial pyrolysis at 750°C. In brief, the final AC yields for the indirect activation route were in the range of 8.0-11.6%, which slightly varied with changing pyrolysis temperature, since the process conditions of the indirect $CO_2$ activation were

fixed at 800°C and 60 min. The BAC-450-I with lowest AC yield (8.0%) was observed after an initial pyrolysis at 450°C and then indirect activation.

Table 2.1 The BAC yield by indirect (label with -I) and direct activation (label with -D).

| Sample | Original Weight (g) | Char Yield Percentage (%) | Final AC Yield (g) | Final Yield Percentage (%) |
|---|---|---|---|---|
| BAC-250-I | 10 | 90.6 | 0.95 | 9.5 |
| BAC-350-I | 10 | 38.4 | 0.96 | 9.6 |
| BAC-450-I | 10 | 26.9 | 0.80 | 8.0 |
| BAC-550-I | 10 | 24.2 | 0.82 | 8.2 |
| BAC-750-I | 10 | 23.6 | 1.16 | 11.6 |
| BAC-700-30-D | 10 | - | 2.04 | 20.4 |
| BAC-700-60-D | 10 | - | 2.03 | 20.3 |
| BAC-750-30-D | 10 | - | 1.67 | 16.7 |
| BAC-750-60-D | 10 | - | 1.66 | 16.6 |
| BAC-800-30-D | 10 | - | 1.27 | 12.7 |
| BAC-800-60-D | 10 | - | 0.89 | 8.9 |

In the case of direct activation route, it was found that the AC yield decreased from 20.3 to 8.9% with increasing activation temperature from 700° to 800°C at the processing time of 60 min. Similar trend was also observed for the samples activated for 30 min. This indicated that the final yield was dictated mainly by the activation temperature. The processing time was determined to not have a significant influence on the final yield, particularly at the activation temperatures of 700° and 750°C. The final AC yield decreased from 12.7 to 8.9% with increasing processing time from 30 to 60 min at the activation temperature of 800°C. This could be explained by the existence of a rapid increase of the reaction rate for carbon and carbon dioxide between 750° and 800°C, where the gasification behavior of biomass became more intensive. It was reported that the reaction rate of char gasification in carbon dioxide environment was determined by two major parameters, which are temperature and partial pressure of gas (Klose and Wolki, 2005). The study showed that the oil palm shell char has nearly two times increased reaction rate when the processing temperature increased from 750° to 780°C.

### 2.4.2. Surface area and pore structure

The adsorption-desorption isotherms of the biomass-derived activated carbons (BACs) prepared by direct and indirect activation are presented in Figure 2.1(a) and (b), respectively. All the BACs displayed a mixture of type I and type II isotherm. Type I isotherm indicated the formation of activated carbon with micropores and narrow mesopores (2.0-2.5 nm), while type II typically refers to the macroporous structure (Thommes et al. 2015). The type II was confirmed by the observation of increasing nitrogen uptake at high relative pressure (0.9-1.0) and the existence of H4 type hysteresis. The presence of the hysteresis loops was also identified for all indirectly activated samples and also directly activated samples only at 800°C. The identified typical H4-type hysteresis loop also supported the micro-mesoporous structure for these BACs.

For the direct activation route, higher temperatures resulted in steeper uptakes of nitrogen at lower $P/P_0$ (<0.1). The BACs directly activated at 700° and 750°C revealed a type I(a) due to lower uptakes, which indicated that they have narrow micropores with sizes less than 1 nm. The larger uptakes at lower $P/P_0$ recorded for the BACs directly activated at 800°C (BAC-800-30-D and BAC-800-60-D) implied type I(b) isotherms. This indicated that they have wider micropores, as well as, narrow mesopores. These results for the direct activation route are further supported by the NLDFT analysis of pore size distribution as displayed in Figure 2.1(c). As the $CO_2$ activation temperature increased from 700° to 800°C, the pore volume in the range of 0.5-1.5 nm significantly increased. It is evident that the higher activation temperatures promoted the formation of micropores and also narrow mesopores (~2.0-2.5 nm) for the direct activation route. This is in good agreement with a previously reported study (Sudaryanto et al. 2006). They showed that the carbon materials prepared at the range of 450°-650°C were composed of micro- and meso-pores, whereas mesopore structure was further developed at 750°C.

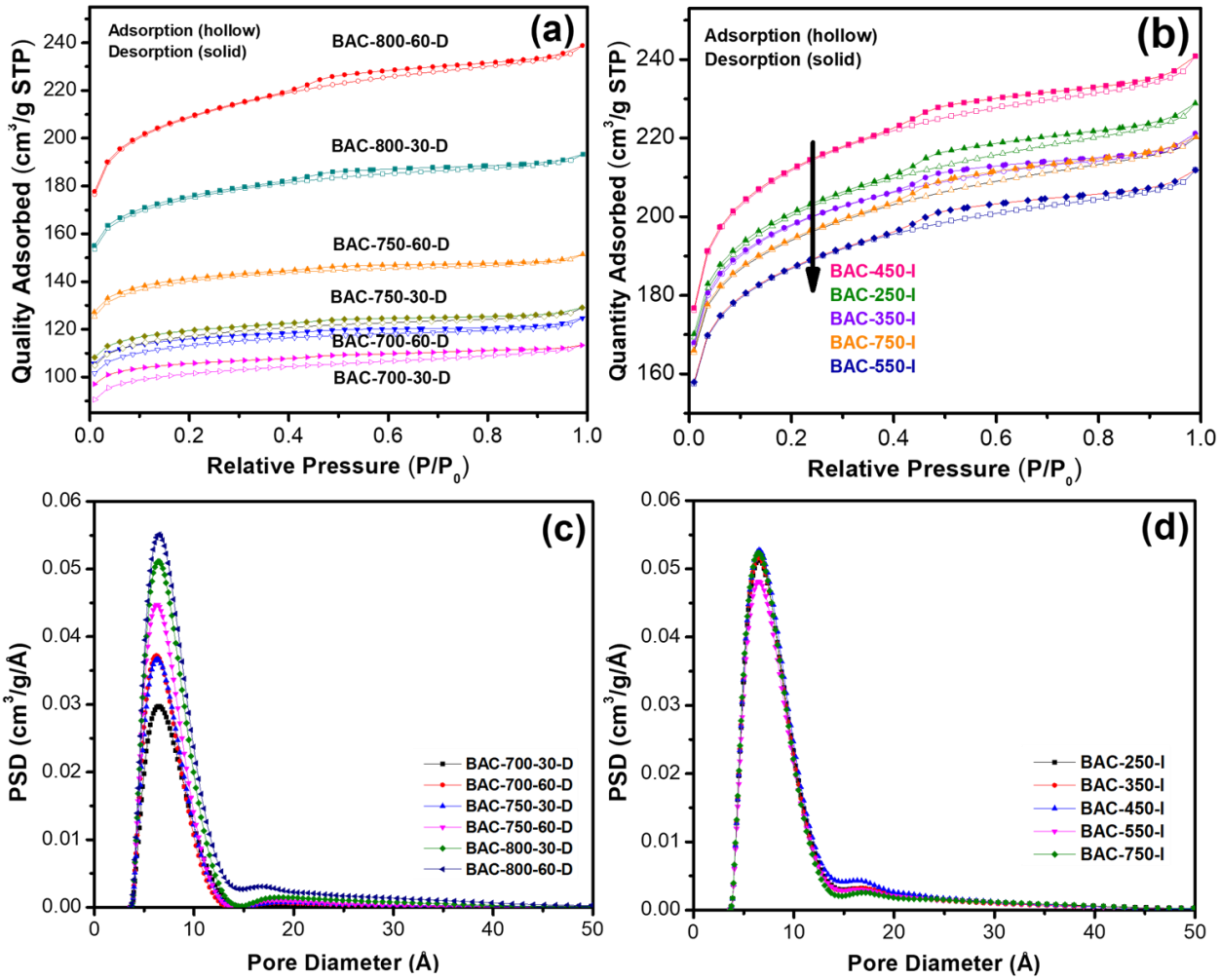


Figure 2.1. The porosity characterization of activated carbon samples: the adsorption and desorption curves of direct activated carbons (a) and indirectly activated carbons (b); the pore size distribution by NLDFT for direct activation samples (c) and indirect activation samples (d).

Due to the increased pore volume and formation of highly micro-mesoporous structure, the optimal $CO_2$ activation conditions were determined to be 800°C and 60 min for the hybrid willow biomass used. Therefore, these experimental conditions were applied to the second step of the indirect activation following the pyrolysis step. In the case of the indirect activation route (pyrolysis + $CO_2$ activation), micropore volume was found to be highly similar for all BAC samples, as shown in Figure 2.1(d). This indicated that the pyrolysis temperature has a very limited influence on the

pore volume and pore size distribution. When the pyrolysis temperature was above 450°C, the volume of wider micropores (1.5-2.0 nm) relatively decreased, indicating a partial collapse of the pore structure at higher temperatures.

Table 2.2 The porosity of activated carbon materials prepared by both methods.

| Sample | BET Surface Area ($m^2/g$) | Micropore Area ($m^2/g$) | Micropore Volume ($cm^3/g$) | Total Pore Volume ($cm^3/g$) | BET Pore Size (nm) |
|---|---|---|---|---|---|
| BAC-700-30-D | 358.85 | 283.83 | 0.12 | 0.18 | 1.95 |
| BAC-700-60-D | 400.91 | 318.42 | 0.13 | 0.19 | 1.92 |
| BAC-750-30-D | 415.00 | 325.63 | 0.14 | 0.19 | 1.92 |
| BAC-750-60-D | 469.64 | 391.99 | 0.17 | 0.23 | 1.88 |
| BAC-800-30-D | 618.61 | 465.53 | 0.20 | 0.30 | 1.93 |
| BAC-800-60-D | 738.74 | 507.64 | 0.22 | 0.37 | 2.00 |
| BAC-250-I | 708.79 | 484.57 | 0.21 | 0.35 | 1.99 |
| BAC-350-I | 700.48 | 484.92 | 0.21 | 0.34 | 1.95 |
| BAC-450-I | 750.70 | 498.20 | 0.21 | 0.37 | 1.98 |
| BAC-550-I | 661.52 | 452.71 | 0.20 | 0.32 | 1.98 |
| BAC-750-I | 686.62 | 482.59 | 0.21 | 0.34 | 1.98 |

To summarize, the specific surface area, micropore area, micropore volume and total pore volume of the prepared BACs are listed in Table 2.2. For the direct $CO_2$ activation route, the specific surface area, micropore volume and total pore volume increased with increasing activation temperature and time. It has been reported that the temperature and resident time are the dominating parameters previously (Zhang et al. 2004). Therefore, among all directly activated BACs, highest surface area (738.7 $m^2/g$) and total pore volume (0.37 $cm^3/g$) were achieved after processing at 800°C for 60 min (BAC-800-60-D). In the case of the indirect $CO_2$ activation route, highest specific surface area (750.7 $m^2/g$) and total pore volume (0.37 $cm^3/g$) was obtained by BAC-450-I sample (pyrolysis at 450°C + $CO_2$ activation at 800°C/60 min). The pyrolysis process at the temperatures above 450°C resulted in a decrease in both surface area and total pore volume. The results also showed that the initial pyrolysis process and temperature have almost no effect on

the micropore volume of the BACs. This implied that the micropore volume is mostly controlled by the second step of the indirect activation route, which is the $CO_2$ activation temperature and time. The pyrolysis step was found to slightly affect the surface area and total pore volume of the prepared activated carbons.

### 2.4.3. Proximate and ultimate analysis

The proximate and ultimate analyses of the selected four samples are presented in Table 2.3 to understand the influence of pyrolysis, direct activation and indirect activation. Two activated carbon samples prepared via direct and indirect activation route (BAC-800-60-D and BAC-450-I) were compared to the raw hybrid willow biomass (HW-0) and biochar obtained via pyrolysis at 450°C (BC-450). The proximate analysis showed that the hybrid willow biomass has a moisture content 5.06%, volatile content of 76.52%, ash content of 0.94% and fix carbon content of 17.48. The ultimate analysis of the raw biomass precursor has 47.8% C, 5.7% H, and 44.8% O. Its nitrogen concentration was measured to be very low (0.83%). The same type of hybrid willow biomass but grown in a different site was previously reported for proximate and ultimate analysis. The reported study showed that the hybrid willow has 6.2% moisture content, 79.8% volatile matter, 2.7% ash, 17.5% fixed carbon, 47.3% C, 6.0% H, 45.4% O, 0.98% N (Nobert et al. 2016). The general guideline of proximate and ultimate analysis can be referred to the standard of hybrid willow being used for energy production.

Table 2. 3 Proximate and ultimate analysis of hybrid willow biomass, biochar and activated carbons.

| Sample | Moisture Content (%) | Volatile (%) | Ash (%) | Fix Carbon (%) | C (%) | H (%) | O (%) | N (%) | S (%) |
|---|---|---|---|---|---|---|---|---|---|
| HW-0 | 5.06 | 76.52 | 0.94 | 17.48 | 47.77 | 5.69 | 44.77 | 0.83 | 0 |
| BC-450 | 3.46 | 26.90 | 3.59 | 66.05 | 73.03 | 3.78 | 18.54 | 1.06 | 0 |
| BAC-800-60-D | 4.04 | 13.82 | 7.17 | 74.97 | 77.52 | 2.00 | 12.08 | 1.23 | 0 |
| BAC-450-I | 4.07 | 13.23 | 7.64 | 75.06 | 76.21 | 1.83 | 13.09 | 1.20 | 0.03 |

The guided line was reported as biomass having moisture content (>5%), volatile matter ( <82%), ash (~1%), fix carbon (>17%), C (42-54%), H (~5-6%), O (35-45%), N (<1%) (Demirbas, 2004, Nobert et al. 2016). Upon comparison of the results from the current study with the general guideline, it shows that the hybrid willow biomass in the current study fulfill the general guideline. It should be noted that the presence of high oxygen and limited nitrogen contents are essential for the creation of functional groups on the prepared activated carbons (BACs) surface. The pyrolysis process at 450°C substantially increased the carbon concentration to 73.0%, while decreasing the hydrogen and oxygen contents. Similar to the pyrolysis, both direct and indirect $CO_2$ activation also resulted in increased carbon concentrations (76.2-77.5%), which were relatively higher than the biochar (without activation). The oxygen and hydrogen concentrations also further decreased after both activation processes. Besides, direct activation route revealed the lowest oxygen concentration (12.1%). The pyrolysis and $CO_2$ activation processes all increased the nitrogen concentration from 0.8 to 1.1-1.2%. Furthermore, the volatiles released from the biomass feedstock during thermal treatment typically consist of $CO_2$, CO, $H_2O$, acetic acid and light hydrocarbons (Demirbas, 2004). The activated carbons prepared by both indirect and direct $CO_2$ activation methods has a similar fixed carbon content (75.0%).

### 2.4.4. Microstructures

The microstructure of samples from direct activation was imaged using SEM to investigate the influence of temperature and residence time. Figure 2.2 displayed the images of hybrid willow derived activated carbon. The activated carbon prepared at 700 °C (Figure 2.2a and 2.2b) showed hierarchical structures which has thick cell wall as well as macropores on the surface. It displayed well-developed channels which could be used for ion storage and transportation (Song et al. 2017). The samples prepared at 750 °C have showed very similar structures as 700 °C, while the ones from 800 °C has a more porous surface. The influence of the residence time does not change the microstructure of the activated carbon. The activated carbons prepared by indirect carbonization were displayed in Figure 2.3. The microstructure of samples prepared with different biochar pyrolysis temperature was characterized with SEM. Note that the only difference these samples have was that the intermediate biochar was prepared at different pyrolysis temperature ranging from 250 to 750 °C. Figures 2.3(b) and (e) show plenty large pores on the cell wall. These pores were believed to be created by the burnt-off of pits on the cell wall. The observation could be confirmed by Figure 2.3(c) in which some unburnt pits were clearly observed. The texture in Figure 2.3(e) has firm edges while others have soft ones, duo to higher biochar pyrolysis temperature (750 °C). It is believed that the biochar prepared at higher pyrolysis temperatures tend to react less intensely with $CO_2$. This can also be explained by the yield of activated carbon using biochar with pyrolysis temperature at 750 °C (49.2%, the highest among all temperatures). In general, these activated carbons have relatively directional macropores with numerous mesopores and micropores on the cell wall. The pore shape is tortuous in all activated carbons.

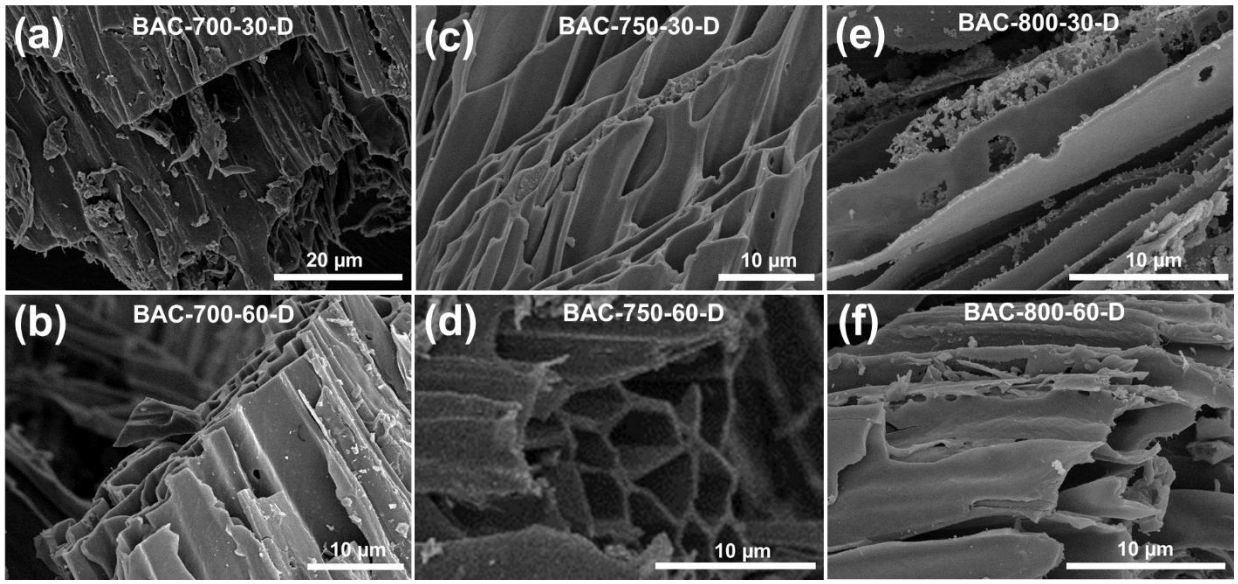


Figure 2.2. SEM characterization of activated carbons by direct activation

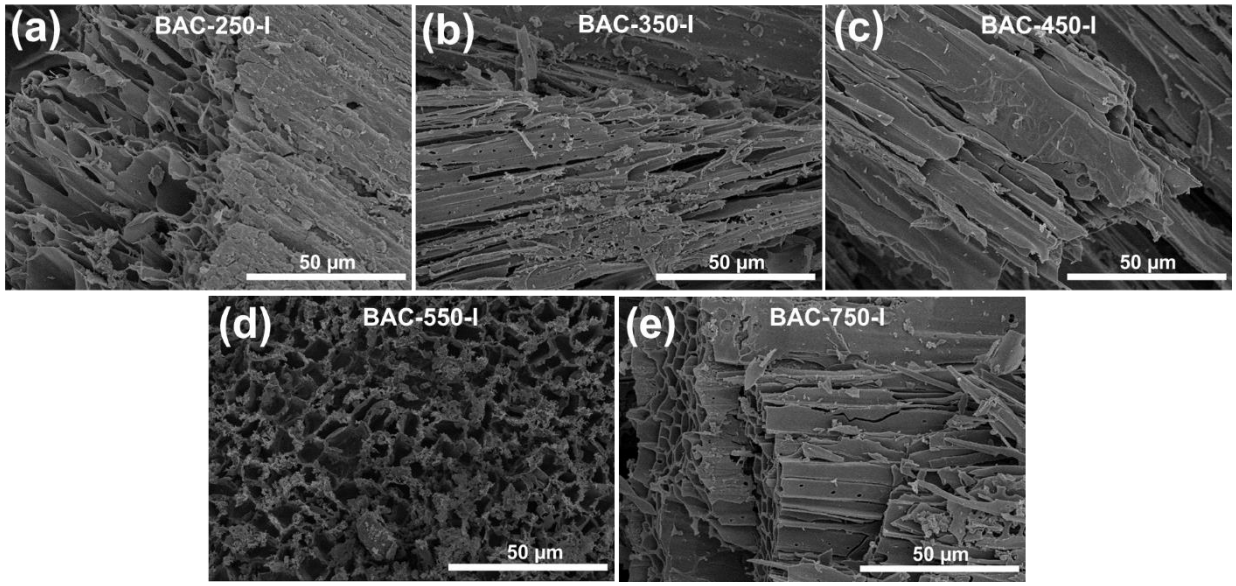


Figure 2.3. SEM characterization of activated carbons by indirect activation

### 2.4.5. Electrochemical performance of supercapacitors

The constant current charge-discharge evaluations were conducted at 100 mA/g current density over 1000 cycles. Figures 2.4 and 2.5 present the constant current charge-discharge profiles of the

activated carbon samples prepared by direct and indirect activation methods, respectively. It should be noted that the results represent the profiles recorded at 499, 500 and 501st cycles of these measurements. Among all directly activated carbon samples, BAC-750-30-D and BAC-800-60-D demonstrated a symmetrical triangular-shaped profile, indicating the formation of electrochemical double layer and good charge-discharge capability (Fig. 2.4). These samples also revealed much lower potential drops (IR drop) in the beginning of their discharge curves. However, other directly activated biomass samples showed disrupted profiles owing to relatively higher IR drops (0.33-0.50 V). On the other hand, all indirectly activated carbon samples displayed the desired triangular profiles (Fig. 2.5), indicating the positive influence of the initial pyrolysis process on their electrochemical performance. The samples initially pyrolyzed at 250° and 750°C (BAC-250-I and BAC-750-I) exhibited relatively higher IR drops (0.16-0.22 V) compared to the other samples pyrolyzed in the temperature range of 350-550 °C, supporting the optimal conditions for the pyrolysis process.

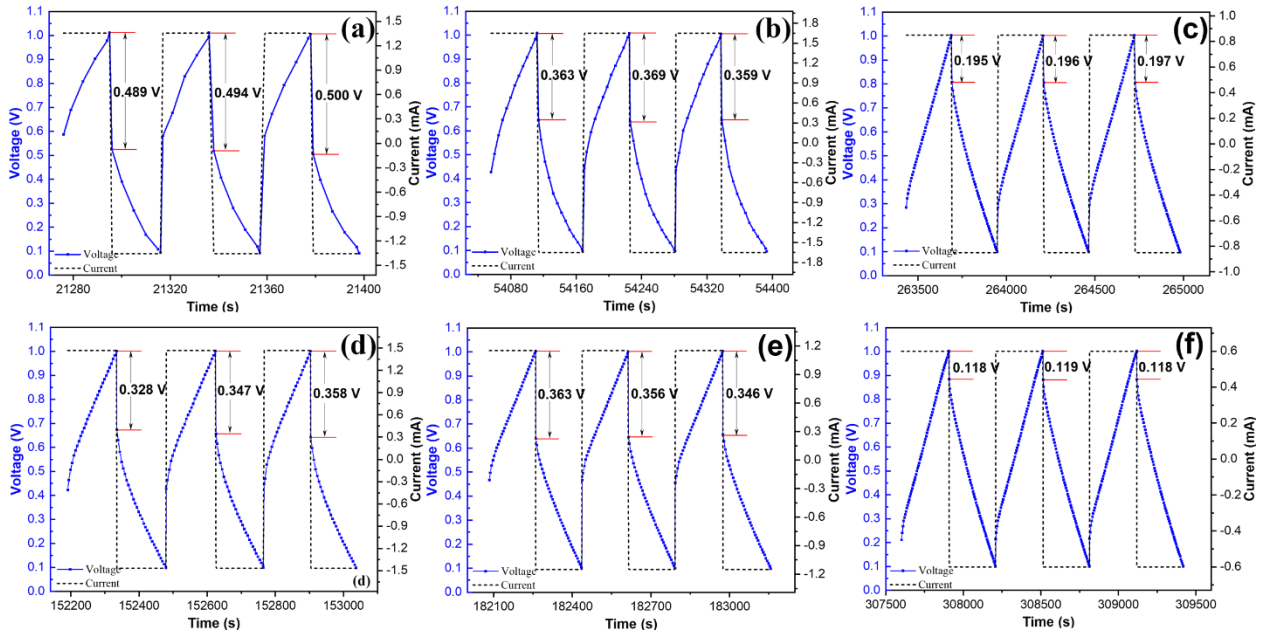


Figure 2. 4. Charge-discharge tests of direct activation samples under constant current density of 100 mA/g: (a) BAC-700-30-D, (b) BAC-700-60-D, (c) BAC-750-30-D, (d) BAC-750-60-D, (e) BAC-800-30-D, and (f) BAC-800-60-D.

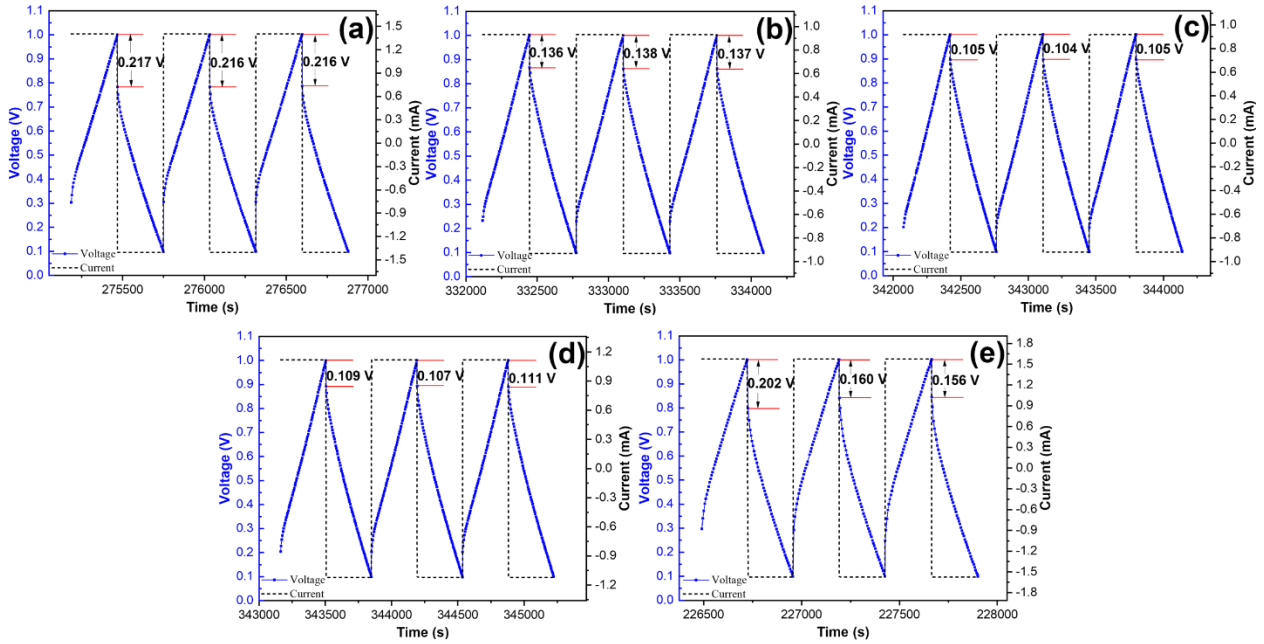


Figure 2. 5. Charge-discharge of indirect activation samples under constant current density of 100 mA/g: (a) BAC-250-I, (b) BAC-350-I, (c) BAC-450-I, (d) BAC-550-I and (e) BAC-750-I.

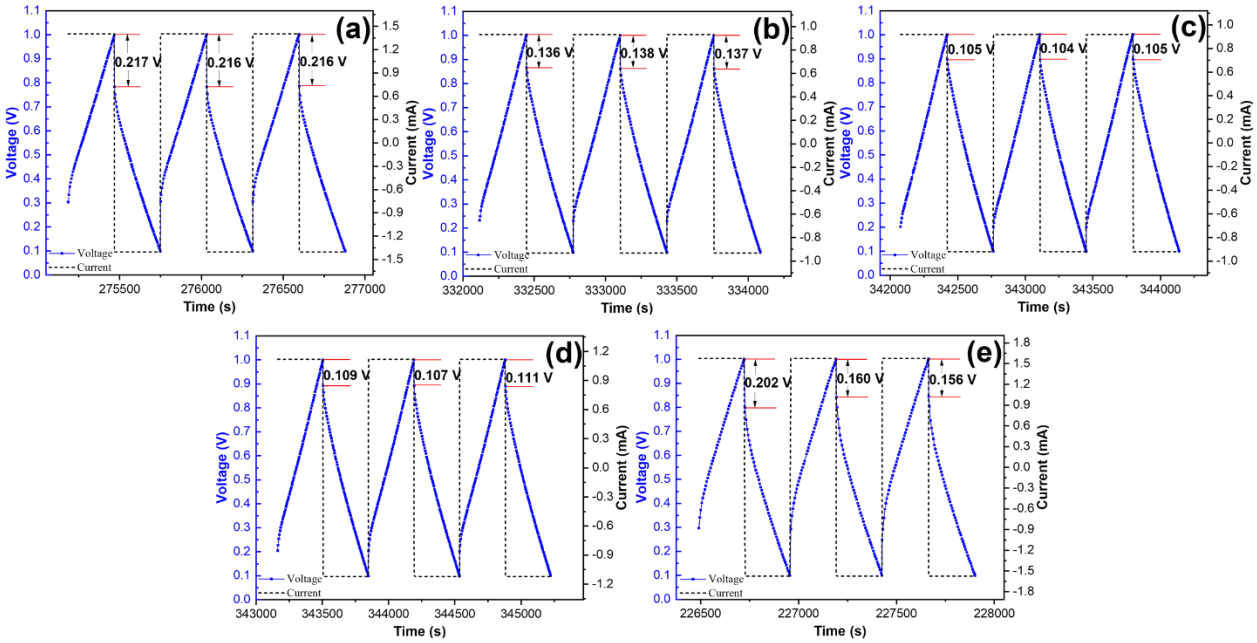


Figure 2. 6. Self-discharge tests of direct activation samples under constant current density of 100 mA/g and an hour rest period: (a) BAC-700-30-D, (b) BAC-700-60-D, (c) BAC-750-30-D, (d) BAC-750-60-D, (e) BAC-800-30-D, and (f) BAC-800-60-D.

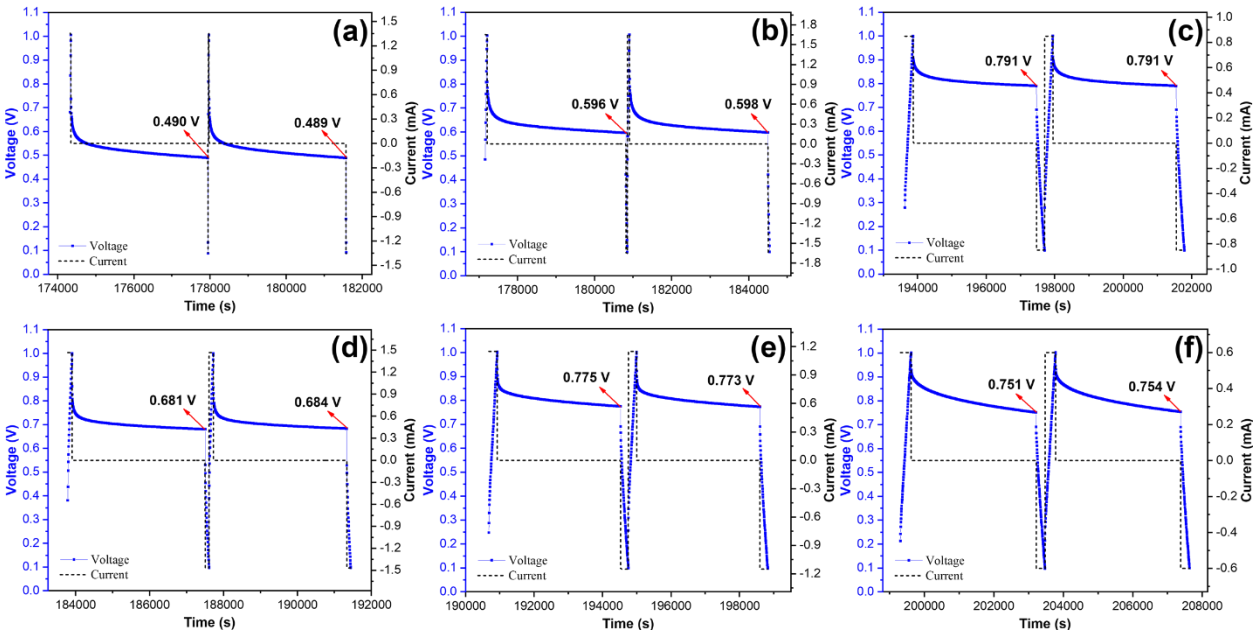


Figure 2. 7. Self-discharge tests of indirect activation samples under constant current density of 100 mA/g and an hour rest period: (a) BAC-250-I, (b) BAC-350-I, (c) BAC-450-I, (d) BAC-550-I, and (e) BAC-750-I.

The self-discharge behavior was additionally investigated under conditions of 100 mA/g current density and an hour rest period over 50 cycles (Figures 2.6 and 2.7). Among all directly activated samples, the voltage decrease was relatively higher (0.40-0.51 V) for the samples activated at 700°C (Fig. 2.6(a-b)). With increasing activation temperature, a better self-discharge capability was achieved, since the voltage decay over an hour rest period after 50 cycles dropped to the range of 0.21-0.32 V. The BAC-750-30-D, BAC-800-30-D and BAC-800-60-D samples clearly exhibited a better self-discharge performance and electrochemical stability (Fig. 2.6(c-e-f)). For all indirectly activated samples, voltage decrease was found to range between 0.15 and 0.22 V (Figure 2.7). Like the constant current charge-discharge results, the samples initially pyrolyzed at 350°-550°C exhibited lower voltage decay and improved self-discharge behavior (Fig. 2.7(b-c-d)). These samples displayed better self-discharge behavior in comparison to the directly activated

carbon samples. It is evident that the initial pyrolysis process can be effectively utilized to improve the overall electrochemical performance of biomass-derived activated carbons.

The specific capacitance of the biomass-derived activated carbon electrodes was calculated from their discharge curves (Figures 2.8 (a-b)). As expected, their specific capacitance decreased with increase of current density at different levels. To summarize the capacitive performance of the activated carbons at 100 mA/g, BAC-800-60-D sample displayed a higher specific capacitance (80.9 F/g), whereas the lowest specific capacitance (9.3-21.0 F/g) values were obtained by BAC-700-30-D and BAC-700-60-D samples. The results demonstrated that their capacitive performance was significantly improved by increasing the activation temperature and time. Similar performance trends can be also seen at 50 and 150 mA/g. Among all indirectly activated carbon samples, similar specific capacitances (89.0-92.7 F/g) were recorded for the samples initially pyrolyzed at the temperatures of 250°-550°C (Fig. 2.8(b)). The specific capacitance of the BAC-750-I, which was initially pyrolyzed at a higher temperature, was 72.7 F/g at 100 mA/g current density. Therefore, it is highly evident that the initial pyrolysis process is effective for enhancing the electrochemical performance when conducted at an optimal temperature.

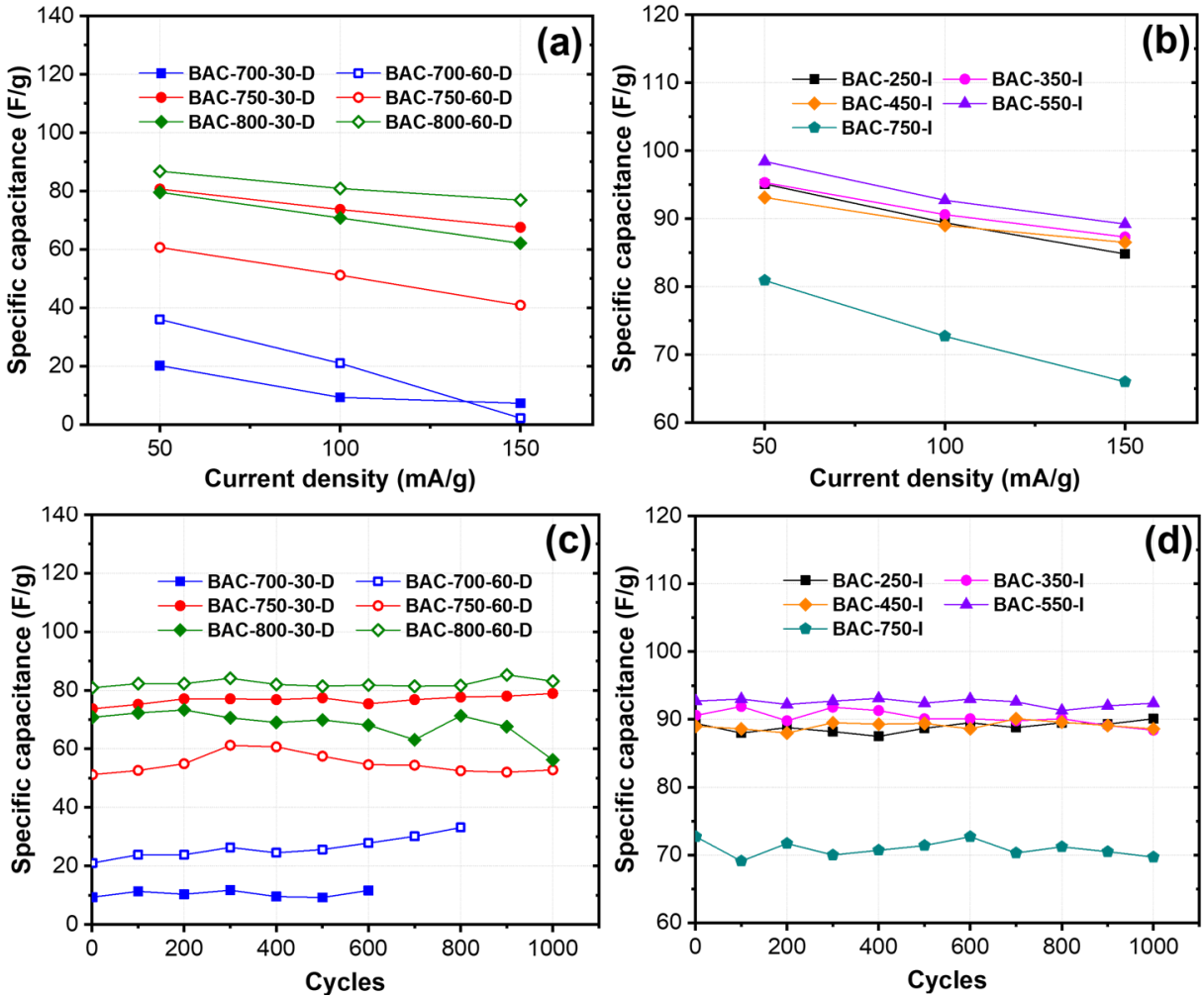


Figure 2. 8. (a-b) Specific capacitances of activated biomass and biochar samples as a function of current density, (c-d) specific capacitances of activated biomass and biochar samples as a function of number of cycles (cycling stability) over 1000 cycles at 100 mA/g constant current density.

Lastly, their cyclic performance was evaluated under the current density of 100 mA/g up to 600-1000 cycles (Figures 2.8(c-d)). All samples (except for the BAC-800-30-D) displayed high electrochemical cycling stability. It should be noted that specific capacitance of the BAC-700-30-D and BAC-700-60-D samples was highly lower compared to the other samples, and thereby, their supercapacitors failed at 600th and 800th cycles, respectively (Fig. 2.8(c)). Interestingly, the specific capacitance of all directly activated carbon samples (except for the BAC-800-30-D and

BAC-250-I) increased by 0.7-12.1 F/g after 1000 cycles charging-discharging. The capacitance retention for the BAC-800-30-D after 1000 cycles was 79.4%, indicating its poor cycling stability among all carbon samples. On the other hand, other indirectly activated carbon samples (BAC-350-I, BAC-450-I, BAC-550-I and BAC-750-I) showed significantly high capacitance retention (95.9-99.7%) after 1000 cycles (Fig. 2.8(d)). This also supports that the optimal pyrolysis temperature should be at the range of 450°-550°C in order to achieve the best cycling stability and electrochemical performance.

### 2.4.6. Chemistry and surface functional groups

The X-ray photoelectron spectroscopy (XPS) survey spectra of the as-prepared activated carbons via direct and indirect activation method are shown in Figure 2.9. The results displayed two main peaks at around 285.3 and 532.0 eV as corresponding to the characteristic C1s and O1s, respectively. The intensity of O1s had a significant increase in BAC-800-60-D compared to other directly activated carbon samples. In addition, slight changes were detected for the C1s peak for these samples (Figure 2.9(a)). On the other hand, for the indirect activation route, the C1s peak intensity highly increased as the pyrolysis performed at higher temperatures (Figure 9(b)).

The Raman spectra of all activated carbons showed two characteristic peaks corresponding to the D and G bands (Figure 2.10). The D band at around 1350 $cm^{-1}$ corresponds to the disordered structure of amorphous carbons, and the G band at near 1590 $cm^{-1}$ relates to the graphite in-plane vibration of sp2 hybridized C atoms (Li et al. 2016). The ratio of the relative intensities of D band and G band ($I_D/I_G$) were calculated to examine the changes in the graphitization degree as a function of the processing routes and conditions. A slight change in the ($I_D/I_G$) ratios indicates that the selected experimental parameters did not have a significant effect on the graphitic basal plane and structural chemistry of the biomass-derived activated carbons. The graphitization degree

relatively increased, and thereby, the degree of disorder and defects decreased with increasing pyrolysis temperature (Figure 2.10a). For the directly activated carbons, the ($I_D/I_G$) ratio varied from 0.89 to 0.98 (Figure 2.10b). The increase in the activation temperature and time typically led to a decrease in the graphitization degree. The reason is that the more carbon will be gasified and more defect within the carbon plane will be created, which leads to the decrease of graphitization degree (Abbas et al. 2018).

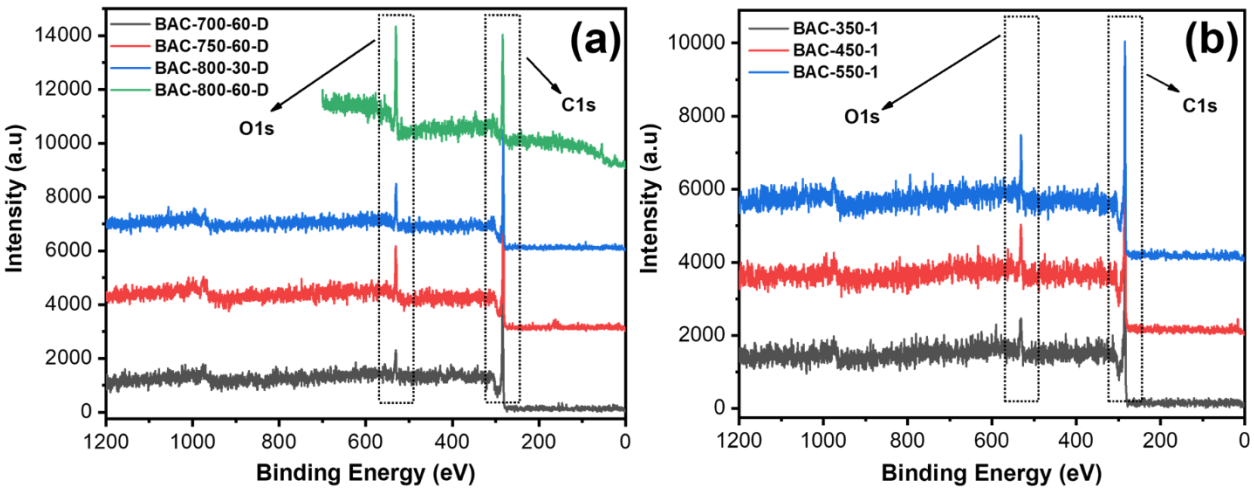


Figure 2. 9. XPS survey spectra of activated carbons prepared by (a) direct activation and (b) indirect activation.

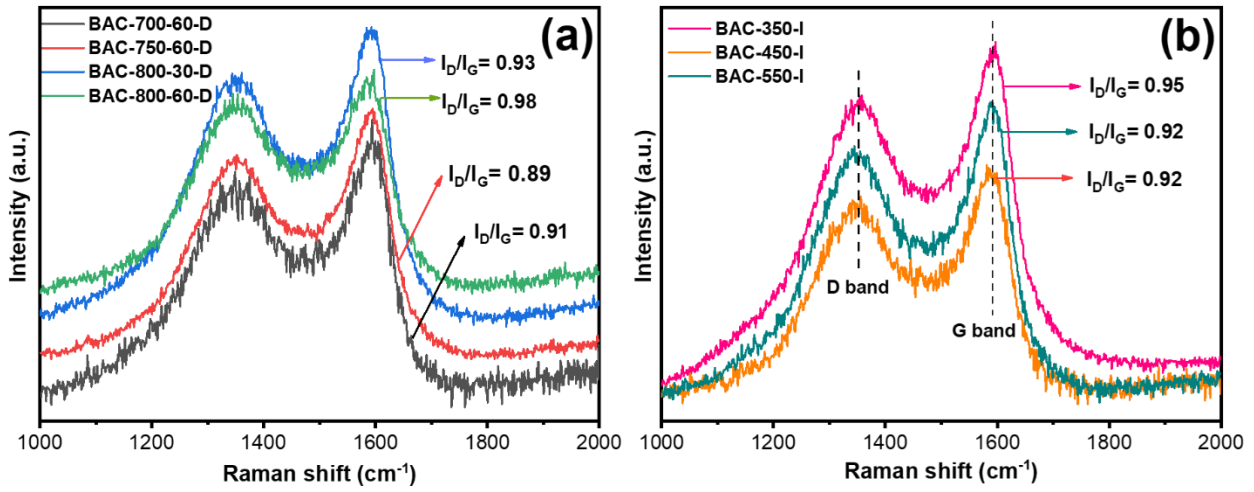


Figure 2. 10. Raman spectra of activated carbons prepared by direct activation (a) and indirect activation (b).

### 2.4.7. Statistical Analysis

Analysis of Variances (ANOVA) has been performed on five parameters of porosity listed in Table 2.2 by different direct activation temperature levels. The global assessment showed that the specific surface area data has a P-value of 0.026 that is less than 0.05, which means that there is a

significant difference between three temperatures (700, 750 and 800 °C). Upon conducting the global assessment on micro-pore area, micro-pore volume, total pore volume and the BET pore size, the results showed P-values of 0.028, 0.025, 0.038 and 0.319, respectively. The P-values indicated that the temperature does not have a significant effect on the pore size while it could significantly affect the specific surface area, micro-pore area, micro-pore volume and total pore volume.

The porosity data of all indirect activated carbons has been listed in Table 2.2 as well. The sample BAC-450-I has the highest surface area and microporous area. Note that all the indirect activation samples listed were prepared at the same carbonization conditions (800 °C for 60 min) from biochar. Although the surface area and microporous area have differences, the microporous volume, total pore volume as well as BET pore size do not have significant differences. The pyrolysis temperature of biochar preparation in indirect activation method has little influence on the micro-pore volume, total pore volume and pore size while it could affect the surface area. The temperature could be optimized based on the pyrolysis temperature of biomass when surface area is a targeted property of the eventual activated carbon.

Table 2. 4 Descriptive statistics of IR drop values of direct activation samples.

| Groups | Count | Sum | Average | Variance |
|---|---|---|---|---|
| BAC-700-30-D | 3 | 1.483 | 0.494 | 3.033-05 |
| BAC-700-60-D | 3 | 1.088 | 0.363 | 3.033-05 |
| BAC-750-30-D | 3 | 0.588 | 0.196 | 1.000-06 |
| BAC-750-60-D | 3 | 1.033 | 0.344 | 2.303-04 |
| BAC-800-30-D | 3 | 1.065 | 0.355 | 7.333-05 |
| BAC-800-60-D | 3 | 0.355 | 0.118 | 3.333-07 |

Table 2. 5 ANOVA of IR drop values of direct activation samples.

| Source of Variation | SS | df | MS | F | P-value | F crit |
|---|---|---|---|---|---|---|
| Between Groups | 0.269 | 5 | 0.054 | 883.604 | 5.772-15 | 3.106 |
| Within Groups | 7.307-04 | 12 | 6.089-05 | | | |
| Total | 0.270 | 17 | | | | |

ANOVA has been conducted using the IR drop values from direct activation samples and indirect activation samples, respectively. The results of ANOVA have been showed in Table 2.4-2.7. Table 2.4-2.5 are the global ANOVA results for the IR drops values of direct activation samples. The P-value is 5.772-15, which is less than 0.05 and indicates that there is a significant difference of IR drops among these six samples. For example, if IR drops of BAC-700-60-D and BAC-800-60-D were compared using ANOVA, the P-value is 1.767-07, which is less than 0.05. It indicates that the sample prepared at 800 °C has a significant lower IR drop than the one prepared at 700 °C.

The Table 2.6-2.7 are the global ANOVA results for the IR drop values of indirect activation samples. The P-value is 1.367-06, which is less than 0.05. It shows that there is significant difference among the IR drop values of these five samples. For example, if IR drops of BAC-250-I and BAC-450-I were compared using ANOVA, the P-value is 1.911-09, which is less than 0.05. It shows that the pyrolysis temperature at 450 °C during indirect activation resulted in a higher IR drop than the one prepared with pyrolysis temperature at 250 °C.

Table 2. 6 Descriptive Statistics of IR drop values of indirect activation samples.

| Groups | Count | Sum | Average | Variance |
|---|---|---|---|---|
| BAC-250-I | 3 | 0.649 | 0.216 | 3.333-07 |
| BAC-350-I | 3 | 0.411 | 0.137 | 1.000-06 |
| BAC-450-I | 3 | 0.314 | 0.105 | 3.333-07 |
| BAC-550-I | 3 | 0.327 | 0.109 | 4.000-06 |
| BAC-750-I | 3 | 0.518 | 0.173 | 6.493-04 |

Table 2. 7 ANOVA of IR drop values of direct activation samples.

| Source of Variation | SS | df | MS | F | P-value | F crit |
|---|---|---|---|---|---|---|
| Between Groups | 0.026 | 4 | 6.598-03 | 50.368 | 1.367-06 | 3.478 |
| Within Groups | 1.310-03 | 10 | 1.310-04 | | | |
| Total | 0.028 | 14 | | | | |

## 2.5. Discussion

### 2.5.1. Reaction Mechanism

The temperature range (700°-800°C) utilized in carbon dioxide activation processes in this study mainly covers the degradation of hemicellulose (two degradation peaks at 230° and 280°C) and cellulose (one degradation peak at ~340 °C). The lignin starts to degrade at a relatively lower temperature (~160 °C) and continues to degrade along the entire thermal process. It is well known that lignin has a relatively stable thermal property than cellulose and hemicellulose (Yang et al. 2007). This is due to that lignin structure has significant amount of thermally stable aromatic rings. For the direct $CO_2$ activation route, the different residence time at 700° or 750°C shows few influences on the yield of AC while it displays visible difference when the temperature is 800°C. The observation indicates that at the temperature less than 750 °C, the activation reaction, essentially gasification of carbon, is not the major reaction. The main reaction should be the pyrolysis in carbon dioxide atmosphere (inert, like nitrogen). It was reported that the edothermic Boudouard reaction (carbon reacts with carbon dioxide and generates carbon monoxide) reaches equilibrium around 700 °C (Mathieu and Dubuisson, 2002). At this very temperature, the samples reside inside the furnace for 30 min or 60 min should not have visible difference of yield. Therefore, when the temperature is 750 °C, the equilibrium should be broken, and the reaction will favor the production of carbon monoxide. Residing for 30 mins and 60 mins should have different yield of

activated carbon. However, this is not consistent with the experimental observation in this study. The Boudouard reaction considers the carbon to be pristine carbon while the reaction in this study starts with biochar. The biochar is not pure carbon since it has oxygen and hydrogen.

The reactions happening and leading the pore development of activated carbon during the direct activation are but not limited to the following. The cellulose mainly undergoes dehydration at temperatures lower than 350°C, depolymerization between 350° and 450°C, and fragmentation above 450°C (Van de Velden et al. 2010). However, the dehydration and depolymerization of the hemicellulose occurs at the temperatures lower than 280°C and higher temperatures, respectively. In the case of lignin, dehydration occurs at the temperatures lower than 500°C, and it decomposes into monomers at higher temperatures. The decomposition of the biomass precursors typically results in the release of volatiles, and thus, leaves the char, that undergoes an intensive gasification process as the temperature reaches above 750°C as presented in this study. The stated reaction of the biochars with carbon dioxide is known as the Boudouard reaction (Ergun 1956) between the fixed carbon within the biochar and $CO_2$. The Boudouard reaction formula (Eq. (2)) is as below:

$$2CO \leftrightarrows CO_2 + C \tag{2}$$

The effect of the temperature on the extent of $CO_2$ and C reaction is assessed by the value of the equilibrium constant. The value of $\log_{10}(K_{eq})$ for the Boudouard reaction as a function of temperature in Kelvin (valid between 500-2200K) is as below in Eq. (3):

$$\log_{10} K_{eq} = \frac{9141}{T} + 0.000224T - 9.595 \tag{3}$$

$\text{Log}_{10}(K_{eq})$ has a value of zero at 975 K (701.85°C), which indicates that the reaction does not consume or form more solid carbon. As the activation temperature increased, the equilibrium constant greatly decreased. This implies that the Boudouard reaction takes place much quickly in favor of forming CO and consuming solid carbon. It is important to note that two additional

activation experiments were conducted in this study at 850° and 900°C for 30 min, but only ashes were obtained instead of activated carbon materials. This could be directly due to relatively lower equilibrium constants at higher temperatures as listed in Table 2.8.

The activation time is directly related to the reaction time between carbon matrix and carbon dioxide. The more time to react, the more carbon could be reacted with $CO_2$ to consume the solid material, and thus, create more pores. During direct activation, when the activation temperature was set at 700 °C, the yield result did not show visible change as the residence time increases. Given the Boudouard reaction kinetics, the unchanged or slightly changed yield indicated that when the residence time increased from 30 to 60 min, the reaction did not take place intensively at both 700 and 750 °C. As the temperature increased from 750 to 800 °C, the reaction became more intense. It is believed that major porosity was created in this stage. When the temperature is at or over 850 °C, the activation time of 30 min might be too long since it was observed that the carbon was totally burnt off. One the other hand, for indirect activation, the biochar pyrolysis temperature is the only variable since the condition for the activation is the same for each sample (800 °C for 60 min). The results of indirect activation showed that higher pyrolysis temperature leads to lower biochar yield. The activation carbon yield percentage from the biochar are increasing as the pyrolysis temperature increases. For example, 9.06 g biochar from pyrolysis at 250 C produces 0.95 g AC (10.5% yield) while 2.36 g biochar from pyrolysis at 750 C produces 1.16 g AC (49.2% yield). This is due to biochar reactivity with carbon dioxide. The activation process is essentially gasification of biochar in carbon dioxide. Higher pyrolysis temperature will reduce the organic functional groups while produce more aromatic ring and graphite structures, resulting in a reduction of char reactivity (Yin et al. 2018).

Table 2. 8 The kinetics of activation process at different temperature

| Temperature (°C) | Temperature (K) | $\log_{10}(K_{eq})$ |
|---|---|---|
| 700 | 973.15 | 0.016 |
| 750 | 1023.15 | -0.432 |
| 800 | 1073.15 | -0.837 |
| 850 | 1123.15 | -1.205 |
| 900 | 1173.15 | -1.540 |

### 2.5.2. Influence of processing parameters on electrochemical performance

The constant current charge-discharge results of the directly activated carbons showed that the activation process at 700°C revealed the highest IR drop. The results clearly implied that 700°C was not sufficient for better surface area and pore development, and resultant electrochemical performance. At higher activation temperatures and processing times, the low IR drop and highly improved retention rate of capacitance were achieved, particularly for the BAC-800-60-D sample. It is known that the IR drop occurs primarily due to the electrolyte resistance, ion diffusion inner resistance and electrode/collector contact resistance (Kang et al. 2012, Zhang et al. 2012). It is evident that the higher activation temperature and time promoted higher specific surface area, total pore and micropore volume, which thereby highly enhanced the electrochemical performance. For the indirectly activated carbon samples, desired triangular charge-discharge curves were achieved for all without depending upon the pyrolysis temperature at the initial stage. This clearly implies that the pore network and the formation of electrochemical double layer are mostly influenced and controlled by the second stage ($CO_2$ activation) of the indirect activation process. On the other hand, it is found that the pyrolysis mainly affects the specific surface area and total pore volume, but not at significant level. The results showed that the highest surface area and total pore volume can be achieved by optimizing the pyrolysis temperature at the initial stage to the range of 450°-

550°C. The charge-discharge, self-discharge and capacitive performance of the biomass-derived activated carbons are shown to be enhanced by this optimal pyrolysis temperature range. The self-discharge curve in Figure 2.6 and 2.7 begins with a rapid decrease in voltage and current. Then the curve will reach to a plateau. Zhou et al (2007) reported a statement for the self-discharge behavior by linking leakage current and self-discharge to the double layer structure on the electrode. The self-discharge behavior showed a dramatic decrease in current and voltage before 15 minutes then stays at a plateau along with the time increase. The performance is related to the double layer that has two parts: one is the compact layer which strongly interacting with the electrode, and the other one only called diffusion layer only weakly interacting with the electrode (Zhou et al. 2007). As the ions move back to the bulk electrolyte from the diffusion layer, the ions of the compact layer move to diffusion layer because of vibration as well as the difference of concentrations between two layers (Chun et al. 2014). Due to that the speed of compact layer to diffusion one is slower than the process from diffusion layer to bulk one, the self-discharge curve, in the first place, increases rapidly but proceeds to a plateau as the times goes (Chun et al. 2014).

### 2.5.3. Effect of surface functional groups on electrochemical performance

In addition to the XPS survey spectra of the activated carbons prepared, the deconvolution of their C1s peaks (Figure 2.11) showed the major presence of graphitic carbon (C=C) (284.4-284.5 eV) at a certain extent (Reddy et al. 2013). Table 2.9 presents the relative graphitization level of the activated carbons. For the indirectly activated carbon samples, as the initial pyrolysis temperature increased from 350° to 550°C, the graphitic carbon concentration significantly decreased from 89.8% to 58.7%. In the case of the direct activation route, the graphitic carbon level was found to be very high (83.9-90.6%) for the samples activated at 700° and 750°C for 60 min. With increasing

activation temperature to 800°C, the graphitic carbon concentration highly decreased to the range of 54.8-57.2%. Therefore, it is evident that the graphitic carbon content was highly influenced by both pyrolysis and activation steps (e.g. temperature, time), while the temperature of pyrolysis and activation was determined to be the main factor. On the other hand, the deconvolution of C1s peaks revealed the presence of the phenolic or ethereal carbon (C-O/C-O-C) at 285.1-285.9 eV as seen in Figure 2.11 (Li et al. 2016). The relative concentration of these functional groups increased up to 41.3-45.2%, when pyrolysis and activation processes were conducted at higher temperatures as also listed in Table 2.8.

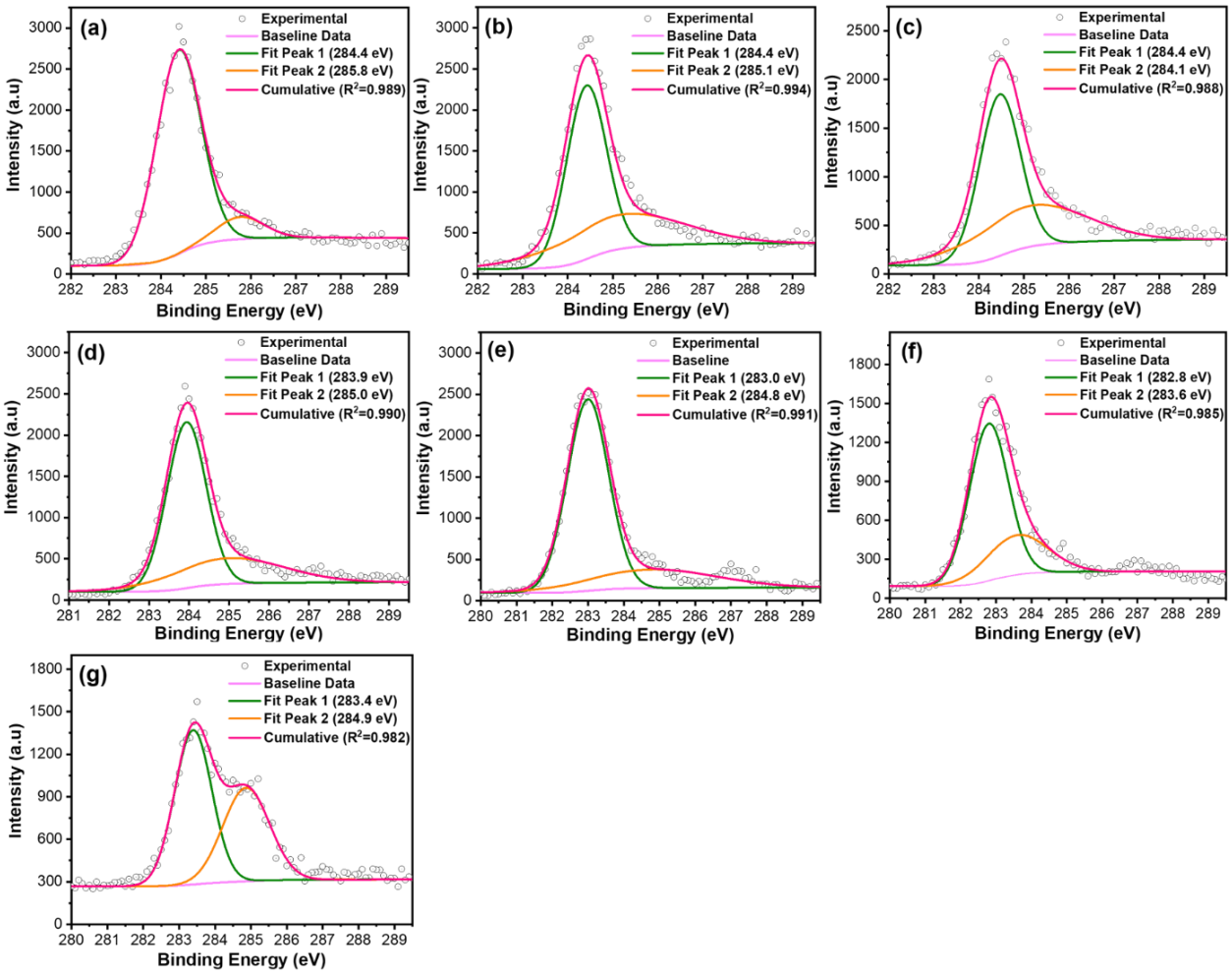


Figure 2. 11. Deconvolution of C1s peaks of all samples: (a) BAC-350-I, (b) BAC-450-I, (c) BAC-550-I, (d) BAC-700-60-D, (e) BAC-750-60-D, (f) BAC-800-30-D, and (g) BAC-800-60-D.

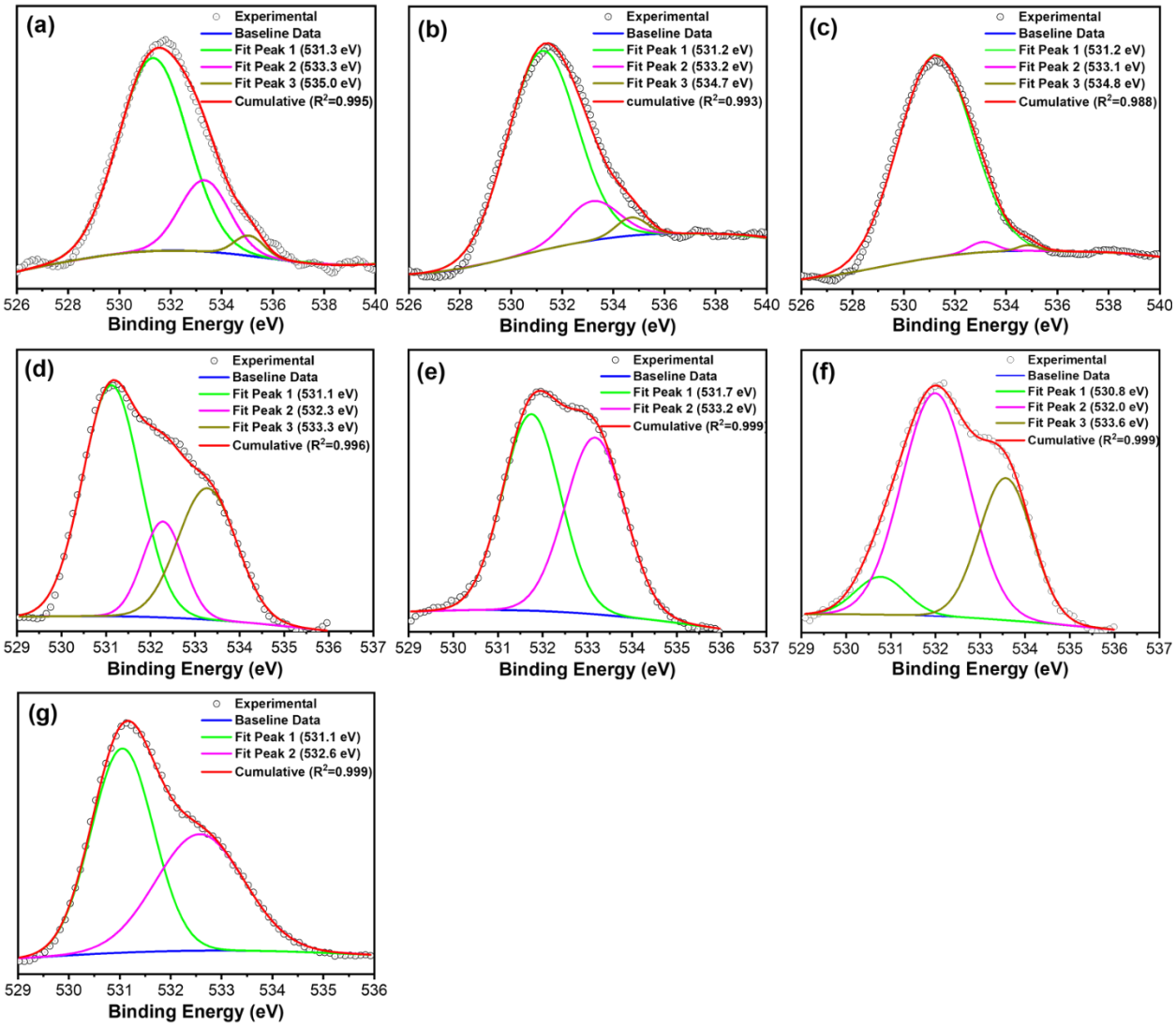


Figure 2. 12. Deconvolution of O1s peaks of all samples: (a) BAC-350-I, (b) BAC-450-I, (c) BAC-550-I, (d) BAC-700-60-D, (e) BAC-750-60-D, (f) BAC-800-30-D, and (g) BAC-800-60-D.

The deconvolution results of the O1s peaks presented three major surface functional groups as presented in Figure 2.12 and also Table 2.10. The peak at the binding energy of 530.8-531.7 eV is assigned to the quinone-type carbonyl groups (O type I, C=O) (531.1 eV). The peak at 532.0-532.6 eV corresponds to the carbonyl O atom in anhydrides and lactones (O type II, C=O) (532.3 eV) and O atoms in the phenolic and ether groups (O type II, C-O/C-O-C) (532.3 eV). The other peak

at 533.1-533.6 eV range can be assigned to the ether O in lactones and anhydrides (O type III, C-O-C) (533.3 eV) (Lennon et al. 2002). The relative concentration of the quinone-type carbonyl groups highly increased from 76.3 to 97.4% with increasing pyrolysis temperature at the initial stage of the indirect activation route. As a result of this effect, the concentration of the ether groups decreased for the indirectly activated carbon samples. In the case of direct activation route, the amount of the quinone-type carbonyl functional groups was found to be much lower (typically around 52-55%) in comparison to the indirect activation route. This clearly indicated that the utilization of the pyrolysis process at the initial stage promoted the formation of these quinone-type carbonyl groups. In addition, the results showed that the type and concentration of the surface functional groups were highly affected by the $CO_2$ activation temperature and time. The increased activation temperature from 700° to 800°C typically resulted in the formation of more phenolic and ether functional groups. It is also evident that the direct activation process without an initial pyrolysis formed relatively more ether functional groups in lactones and anhydrides.

The results clearly presented the significant influence of the processing route and $CO_2$ activation conditions on the surface chemistry and functional groups. It is well known that the oxygen containing surface functional groups also contributes to the electrochemical performance along with the above-discussed properties of the activated carbons (Seredych et al. 2008, Martinez et al. 2005). In particular, the specific capacitance of the activated carbons is highly correlated with the presence of the quinone-type carbonyl groups due to the property being an electron acceptor (Okajima et al. 2005). Therefore, the as-prepared indirectly $CO_2$ activated BAC samples with higher O type I functional groups (quinone-type carbonyl) could be expected to have a higher specific capacitance and better electrochemical performance. Therefore, the BAC-550-I sample revealed the highest specific capacitance, although it showed relatively lower specific surface area,

micropore area and total pore volume. This clearly shows the advantage of the indirect activation route for surface modification, and also proves the significant influence of the surface functional groups on the overall electrochemical performance of the activated carbons.

Table 2. 9 Deconvolution results of C1s peaks of all samples.

| Samples | C=C ($sp^2$) | | | C-OH | | |
|---|---|---|---|---|---|---|
| | BE (eV) | FWHM | % | BE (eV) | FWHM | % |
| BAC-350-I | 284.4 | 1.16 | 89.82 | 285.8 | 1.21 | 10.18 |
| BAC-450-I | 284.4 | 1.04 | 61.09 | 285.1 | 3.36 | 38.91 |
| BAC-550-I | 284.4 | 1.06 | 58.66 | 285.1 | 2.96 | 41.34 |
| BAC-700-60-D | 284.5 | 1.22 | 83.85 | 285.8 | 1.60 | 16.15 |
| BAC-750-60-D | 284.5 | 1.32 | 90.56 | 285.9 | 1.52 | 9.44 |
| BAC-800-30-D | 284.4 | 1.07 | 54.81 | 285.1 | 1.41 | 45.19 |
| BAC-800-60-D | 284.4 | 1.23 | 57.16 | 285.9 | 1.53 | 42.84 |

Table 2. 10 Deconvolution results of O1s peaks of all samples.

| Samples | O type I | | | O type II | | | O type III | | |
|---|---|---|---|---|---|---|---|---|---|
| | BE (eV) | FWHM | % | BE (eV) | FWHM | % | BE (eV) | FWHM | % |
| BAC-350-I | 531.3 | 3.17 | 76.34 | - | - | - | 533.3 | 2.27 | 20.22 |
| BAC-450-I | 531.2 | 3.19 | 84.05 | - | - | - | 533.2 | 2.43 | 12.58 |
| BAC-550-I | 531.2 | 3.35 | 97.42 | - | - | - | 533.1 | 1.23 | 1.83 |
| BAC-700-60-D | 531.1 | 1.52 | 53.36 | 532.3 | 1.08 | 15.70 | 533.3 | 1.55 | 30.94 |
| BAC-750-60-D | 531.7 | 1.52 | 51.77 | - | - | - | 533.2 | 1.57 | 48.23 |
| BAC-800-30-D | 530.8 | 1.32 | 7.76 | 532.0 | 1.76 | 61.21 | 533.6 | 1.40 | 31.03 |
| BAC-800-60-D | 531.1 | 1.44 | 55.33 | 532.6 | 2.04 | 44.67 | - | - | - |

## 2.6. Conclusion

The hybrid willow as a lignocellulosic biomass feedstock was successfully converted into highly porous activated carbon with a dominant microporous structure for use in supercapacitor electrodes. The direct and indirect carbon dioxide activation routes were utilized, and the processing parameters were discussed. The results showed that the optimal pyrolysis temperature

was in the range of 450°-550°C, while the activation conditions were optimized at 800°C and 60 min. The specific surface area, total pore volume as well as micropore volume of activated carbon in direct activation increased as the temperature increase. These texture properties reach its highest value at pyrolysis temperature of 450 °C for indirect activation. The microstructure of activated carbon from direct and indirect activation does not have visible difference. The activated carbons prepared in this study exhibited a specific capacitance of 80.9 and 92.7 F/g at current density of 100 mA/g for the direct and indirect activation routes, respectively. In addition, the capacitance loss was measured to be very low (<0.5%) even after 1000 charge-discharge cycles, indicating the high cycling stability. The results also demonstrated that the final electrochemical performance is not only controlled by pore structure and surface area, but also the oxygen-containing functional groups on the surface.

## 2.7. References

Abbas, Q., Mirzaeian, M., Ogwu, A.A., Mazur, M. and Gibson, D., 2018. Effect of physical activation/surface functional groups on wettability and electrochemical performance of carbon/activated carbon aerogels based electrode materials for electrochemical capacitors. International Journal of Hydrogen Energy.

Abioye, A.M. and Ani, F.N., 2015. Recent development in the production of activated carbon electrodes from agricultural waste biomass for supercapacitors: a review. Renewable and sustainable energy reviews, 52, pp.1282-1293.

Bleda-Martínez, M.J., Maciá-Agulló, J.A., Lozano-Castelló, D., Morallón, E., Cazorla-Amorós, D. and Linares-Solano, A., 2005. Role of surface chemistry on electric double layer capacitance of carbon materials. Carbon, 43(13), pp.2677-2684.

Binder, J.B. and Raines, R.T., 2009. Simple chemical transformation of lignocellulosic biomass into furans for fuels and chemicals. Journal of the American Chemical Society, 131(5), pp.1979-1985.

Bouchelta, C., Medjram, M.S., Bertrand, O. and Bellat, J.P., 2008. Preparation and characterization of activated carbon from date stones by physical activation with steam. Journal of Analytical and Applied Pyrolysis, 82(1), pp.70-77.

Brinchi, L., Cotana, F., Fortunati, E. and Kenny, J.M., 2013. Production of nanocrystalline cellulose from lignocellulosic biomass: technology and applications. Carbohydrate Polymers, 94(1), pp.154-169.

Chen, M., Kang, X., Wumaier, T., Dou, J., Gao, B., Han, Y., Xu, G., Liu, Z. and Zhang, L., 2013. Preparation of activated carbon from cotton stalk and its application in supercapacitor. Journal of Solid State Electrochemistry, 17(4), pp.1005-1012.

Chen, X., Li, Z., Wei, L., Li, X., Liu, S. and Gu, J., 2015. Fabrication of hierarchical cabbage-like carbonaceous materials by one-step cobalt-assisted hydrothermal carbonization of furfural. Microporous and Mesoporous Materials, 210, pp.149-160.

Chang, C.F., Chang, C.Y. and Tsai, W.T., 2000. Effects of burn-off and activation temperature on preparation of activated carbon from corn cob agrowaste by $CO_2$ and steam. Journal of Colloid and Interface Science, 232(1), pp.45-49.

Demirbas, A., 2004. Combustion characteristics of different biomass fuels. Progress in energy and combustion science, 30(2), pp.219-230.

Dutta, S., Bhaumik, A. and Wu, K.C.W., 2014. Hierarchically porous carbon derived from polymers and biomass: effect of interconnected pores on energy applications. Energy & Environmental Science, 7(11), pp.3574-3592.

Ergun, S., 1956. Kinetics of the reaction of carbon dioxide with carbon. J. phys. Chem., 60, pp.480-485.

Guo, S., Peng, J., Li, W., Yang, K., Zhang, L., Zhang, S. and Xia, H., 2009. Effects of $CO_2$ activation on porous structures of coconut shell-based activated carbons. Applied Surface Science, 255(20), pp.8443-8449.

Kang, Y.J., Chung, H., Han, C.H. and Kim, W., 2012. All-solid-state flexible supercapacitors based on papers coated with carbon nanotubes and ionic-liquid-based gel electrolytes. Nanotechnology, 23(6), p.065401.

Klose, W. and Wölki, M., 2005. On the intrinsic reaction rate of biomass char gasification with carbon dioxide and steam. Fuel, 84(7-8), pp.885-892.

Lennon, D., Lundie, D.T., Jackson, S.D., Kelly, G.J. and Parker, S.F., 2002. Characterization of activated carbon using X-ray photoelectron spectroscopy and inelastic neutron scattering spectroscopy. Langmuir, 18(12), pp.4667-4673.

Li, B., Dai, F., Xiao, Q., Yang, L., Shen, J., Zhang, C. and Cai, M., 2016. Nitrogen-doped activated carbon for a high energy hybrid supercapacitor. Energy & Environmental Science, 9(1), pp.102-106.

Hayashi, J.I., Horikawa, T., Muroyama, K. and Gomes, V.G., 2002. Activated carbon from chickpea husk by chemical activation with K2CO3: preparation and characterization. Microporous and Mesoporous Materials, 55(1), pp.63-68.

Hoong, Y.B., Paridah, M.T., Luqman, C.A., Koh, M.P. and Loh, Y.F., 2009. Fortification of sulfited tannin from the bark of Acacia mangium with phenol–formaldehyde for use as plywood adhesive. Industrial Crops and Products, 30(3), pp.416-421.

Lu, H. and Zhao, X.S., 2017. Biomass-derived carbon electrode materials for supercapacitors. Sustainable Energy & Fuels, 1(6), pp.1265-1281.

Mathieu, P. and Dubuisson, R., 2002. Performance analysis of a biomass gasifier. Energy conversion and management, 43(9-12), pp.1291-1299.McKendry, P., 2002. Energy production from biomass (part 1): overview of biomass. Bioresource technology, 83(1), pp.37-46.

Mi, B., Chen, X., Jiang, C., Wang, J., Chen, X., Zhang, B., Liu, X., Liu, Z. and Fei, B., 2018. Nitrogen-Doped Porous Carbon Derived from Bamboo Shoot as Solid Base Catalyst for Knoevenagel Condensation and Transesterification Reactions. Catalysts, 8(6), p.232.

Nobert, H.A., McGill, D.W., Grushecky, S.T., Skousen, J.G. and Schuler, J.L., 2016. Salix spp. as a biomass crop: investigating its potential on mined lands and the use of biochar as a soil amendment. Journal American Society of Mining and Reclamation, 5(2), pp.58-76.

Okajima, K., Ohta, K. and Sudoh, M., 2005. Capacitance behavior of activated carbon fibers with oxygen-plasma treatment. Electrochimica Acta, 50(11), pp.2227-2231.

Olivares-Marín, M., Fernández-González, C., Macías-García, A. and Gómez-Serrano, V., 2012. Preparation of activated carbon from cherry stones by physical activation in air. Influence of the chemical carbonisation with H2SO4. Journal of analytical and applied pyrolysis, 94, pp.131-137.

Poddar, S., Kamruzzaman, M., Sujan, S.M.A., Hossain, M., Jamal, M.S., Gafur, M.A. and Khanam, M., 2014. Effect of compression pressure on lignocellulosic biomass pellet to improve fuel properties: Higher heating value. Fuel, 131, pp.43-48.

Reddy, P.M.K., Mahammadunnisa, S.K., Ramaraju, B., Sreedhar, B. and Subrahmanyam, C., 2013. Low-cost adsorbents from bio-waste for the removal of dyes from aqueous solution. Environmental Science and Pollution Research, 20(6), pp.4111-4124.

Seredych, M., Hulicova-Jurcakova, D., Lu, G.Q. and Bandosz, T.J., 2008. Surface functional groups of carbons and the effects of their chemical character, density and accessibility to ions on electrochemical performance. Carbon, 46(11), pp.1475-1488.

Song, S., Ma, F., Wu, G., Ma, D., Geng, W. and Wan, J., 2015. Facile self-templating large scale preparation of biomass-derived 3D hierarchical porous carbon for advanced supercapacitors. Journal of Materials Chemistry A, 3(35), pp.18154-18162.

Sudaryanto, Y., Hartono, S.B., Irawaty, W., Hindarso, H. and Ismadji, S., 2006. High surface area activated carbon prepared from cassava peel by chemical activation. Bioresource technology, 97(5), pp.734-739.

Tarves, P.C., Serapiglia, M.J., Mullen, C.A., Boateng, A.A. and Volk, T.A., 2017. Effects of hot water extraction pretreatment on pyrolysis of shrub willow. Biomass and Bioenergy, 107, pp.299-304.

Tay, T., Ucar, S. and Karagöz, S., 2009. Preparation and characterization of activated carbon from waste biomass. Journal of Hazardous Materials, 165(1-3), pp.481-485.

Thommes, M., Kaneko, K., Neimark, A.V., Olivier, J.P., Rodriguez-Reinoso, F., Rouquerol, J. and Sing, K.S., 2015. Physisorption of gases, with special reference to the evaluation of surface area and pore size distribution (IUPAC Technical Report). Pure and Applied Chemistry, 87(9-10), pp.1051-1069.

Van de Velden, M., Baeyens, J., Brems, A., Janssens, B., & Dewil, R. (2010). Fundamentals, kinetics and endothermicity of the biomass pyrolysis reaction. Renewable energy, 35(1), 232-242.

Volk, T.A., Heavey, J.P. and Eisenbies, M.H., 2016. Advances in shrub‐willow crops for bioenergy, renewable products, and environmental benefits. Food and Energy Security, 5(2), pp.97-106.

Wang, Z., Qie, L., Yuan, L., Zhang, W., Hu, X. and Huang, Y., 2013. Functionalized N-doped interconnected carbon nanofibers as an anode material for sodium-ion storage with excellent performance. Carbon, 55, pp.328-334.

Wang, K., Zhao, N., Lei, S., Yan, R., Tian, X., Wang, J., Song, Y., Xu, D., Guo, Q. and Liu, L., 2015. Promising biomass-based activated carbons derived from willow catkins for high performance supercapacitors. Electrochimica Acta, 166, pp.1-11.

Yang, H., Yan, R., Chen, H., Lee, D.H. and Zheng, C., 2007. Characteristics of hemicellulose, cellulose and lignin pyrolysis. Fuel, 86(12-13), pp.1781-1788.

Yin, Y., Yin, J., Zhang, W., Tian, H., Hu, Z., Ruan, M., Song, Z. and Liu, L., 2018. Effect of Char Structure Evolution During Pyrolysis on Combustion Characteristics and Kinetics of Waste Biomass. Journal of Energy Resources Technology, 140(7), p.072203.

Zhang, T., Walawender, W.P., Fan, L.T., Fan, M., Daugaard, D. and Brown, R.C., 2004. Preparation of activated carbon from forest and agricultural residues through $CO_2$ activation. Chemical Engineering Journal, 105(1-2), pp.53-59.

Zhang, X., Wang, X., Su, J., Wang, X., Jiang, L., Wu, H. and Wu, C., 2012. The effects of surfactant template concentration on the supercapacitive behaviors of hierarchically porous carbons. Journal of Power Sources, 199, pp.402-408.

Zhou, S.Y., Li, X.H., Wang, Z.X., Guo, H.J. and Peng, W.J., 2007. Effect of activated carbon and electrolyte on properties of supercapacitor. Transactions of Nonferrous Metals Society of China, 17(6), pp.1328-1333.

# Chapter 3. Biomass Derived Porous Carbon Materials for Barium Removal from Shale Gas Flowback Water

### 3.1. Abstract

Biomass derived porous carbon materials with high surface areas can be used in various industrial cases, one of which is to remove organics and metal ions from shale gas flowback water. In this work, three biomasses derived porous carbon (BPC) materials with different specific surface areas were fabricated from hybrid willow biomass particles less than 1 mm. The porous materials were labelled as BC, BPC-1 and BPC-2. The biochar (BC) was prepared by pyrolysis of the biomass at 450 °C for 30 minutes. The BPC-1 was prepared by directly carbonizing the mixture of biomass powders and KOH at 800 °C in nitrogen. The BPC-2 was prepared by carbonizing the mixture of biomass char and KOH at 800 °C in nitrogen. The residence time of both carbonizations are 60 minutes. The ratios of the precursor to the activation agent KOH are both 2:1. Based on original weight of the biomass, the yield of BC, BPC-1 and BPC-2 were 21.7%, 18.2% and 14.8%, respectively. Three porous carbon materials were characterized with N2 adsorption and desorption to determine the porosity. The results showed that BC, BPC-1 and BPC-2 have specific areas of 261.9, 1071.4 and 776.6 m2/g, respectively. Then the carbon materials were applied to remove Barium from actual shale gas flowback water. The concentration of Barium was tested with inductively coupled plasma optical emission spectrometry (ICP-OES). Although the porous carbon materials are considered less effective to remove alkali metal ions when compared to removing organics, the results showed that the barium concentration was decreased by 2.5%, 11.3% and 3.3%, respectively, at a relatively low carbon to water ratio (0.4g : 15ml) by BC, BPC-1 and BPC-2. The porous carbon materials after adsorption were also characterized with scanning electron microscopy (SEM) and energy-dispersive X-ray spectroscopy (EDAX). The results showed that adsorbates were observed on porous carbon surfaces with significant Barium peaks which could confirm the adsorption behavior of Ba.

## 3.2. Introduction

Utilizing biomass to produce value-added products has been studied for decades and is still trending in current biomass research (Danish and Ahmad 2018). One of the value-added biomass derived products is the porous carbon material which includes biochar and activated carbon (Kwapinski et al. 2010, Williams and Reed 2006). These porous carbon materials have been widely used in soil preservation and drinking water purification (Woolf et al. 2010, Velten et al. 2011).

Among these porous carbon materials, biochar is less porous. To create porous structure with higher surface area and more porosity, physical and chemical methods have been applied in activation of biomass derived carbon materials. Steam and carbon dioxide are typical activation agents during carbonization of biomass (Savova et al. 2001, Tay et al. 2009). Physical activation is believed to be clean and low cost, but the surface area obtained from the final carbon product is relatively lower than chemical activation. Common activation agents for biomass derived carbon production include KOH, NaOH, $ZnCl_2$, $H_3PO_4$, $K_2CO_3$, etc (Liou 2010, Bagheri and Abedi 2009, Kilic et al. 2012). The process for chemical activation typically includes two types. The first one is two stages activation, or indirect activation. The process starts with biochar preparation at a lower temperature. Then the biochar will be mixed with KOH and activated at a higher temperature. The other one is one stage activation, or direct activation. The biomass will be mixed with KOH and directly activated at a higher temperature. Two-stage process could have higher energy and operational cost. Therefore, the BPC processing could be optimized if the final product of one stage process yields similar or higher properties as the two-stage process.

Regarding to the application of biomass derived porous carbon materials, industrial practices have demonstrated many potential cases. Currently, BPCs were mainly used for environmental applications with a focus on water and air purification. Other applications involve gas purification

(Sakanishi et al. 2005), energy storage (Dutta et al. 2014), and catalysis synthesis (Lee et al. 2004). In shale gas $N_2$ adsorption and desorption test, scanning electron microscope, energy-dispersive X-ray spectroscopy, and Barium adsorption test. The main objective is to optimize the fabrication process of biomass derived activated carbon as well as to apply the resulted activated carbon materials on Barium removal from actual shale gas flowback water.

## 3.3. Material and Method

### 3.3.1. Materials

Hybrid willow was selected as porous carbon precursor in this study. Hybrid willow (Salix spp.) chips as received were provided by Cornell University Agricultural Experiment Station. Belleville SV1 Rep 1 and Bellville Owasco Rep 2 are the two cultivars of hybrid willow. The hybrid willow chips were milled with a 1 mm size sieve to particles. Nitrogen gas was selected to process the biomass porous carbon materials. The nitrogen gas in this work were purchased from Matheson Tri Gas. The KOH was purchased from Sigma Aldrich (Reagent grade). The shale gas flowback water in this study was provided by West Virginia University Water Research Institute.

### 3.3.2. Preparation of Porous Carbon Materials

Three porous carbon materials were prepared and labelled as BC, BPC-1 and BPC-2. The char (BC) was prepared by pyrolysis of hybrid willow biomass in nitrogen at 450 °C for 30 min. The biomass within a ceramic boat was placed into a tube furnace (Lingdberg Model: 23-891, Watertown, WI). The furnace was heated to 450 °C and held for 30 min. The ramping rate was 10 °C/min. Then the heat was removed, and the furnace was naturally cooled down to room temperature.

The BPC-1 was prepared with direct carbonization of the hybrid willow biomass. The biomass was mixed with KOH solution and dried in an oven at 110 °C to remove the water. The biomass and KOH were evenly mixed together. The solid mass ratio of biomass to KOH is 2:1 for BPC-1. The mixture was contained in one ceramic boat. Then the ceramic boat was placed into a tube furnace. The furnace was heated to 800 °C and hold for 60 min. The ramping rate was 10 °C/min. The carbonization was run with a steady nitrogen flow to protect the biomass from burning. Upon carbonization, the heat was removed, and the furnace was cooled down naturally to room temperature.

The BPC-2 was prepared by indirect carbonization of the hybrid willow biomass. The biomass was converted to biochar (BC) first which is the same with previous biochar preparation process mentioned above. Then the char was mixed with KOH solution and the mixture was dried in an oven at 110 °C to remove the water content. The solid mass ratio of biochar to KOH is 2:1. The dried mixture was contained in a ceramic boat and placed into a tube furnace. The furnace was heated to 800 °C and held for 60 min. The ramping rate was 10 °C/min.

After carbonization of biomass or biochar, the final product was collected from the ceramic boat and washed with deionized water to remove impurities. The pH of the washed sample was tested and recorded until reaching neutral. The activated carbon was collected and dried in an oven at 80 C°. The final mass of activated carbon or char as well as the original feedstock mass were obtained and used for yield calculations. We should note that the BPC-2 yield was calculated both on biochar and original biomass weights. The yield was calculated by the ratio of final porous carbon materials to the original weight of biomass.

### 3.3.3. $N_2$ Adsorption and Desorption

A Micromeritics ASAP2020 surface area analyzer was used for $N_2$ physisorption tests. Nitrogen sorption at 77 K will be conducted on a Micromeritics ASAP 2020 surface area and porosimetry system (Micromeritics Instrument Corporation, Norcross, GA) to obtain the adsorption-desorption isotherm of each sample. The Brunauer-Emmett-Teller (BET) specific surface area, total pore volume, volume of meso-pores, volume of micro-pores, and pore-size distributions were calculated from the nitrogen sorption isotherm using the data reduction software included with the system. The samples were outgassed at 300 °C for 6 hours before the tests. Specific surface area and other pore related parameters were obtained from this step.

### 3.3.4. Barium Removal Efficiency Test

The BC, BPC-1 and BPC-2 were applied to remove Ba from actual shale gas flowback water from Marcellus shale wells near West Virginia University in Morgantown, West Virginia. The 15 ml water was pipetted into a 30 ml vial and different carbon material loads were applied, which are 0.1, 0.2 and 0.4 g of each type of carbon materials. The Ba concentration of untreated water was tested three times and used as control. Each Ba concentration after the treatment was tested and repeated for three times. BPC-1 has the highest removal rate at 0.4 g carbon loading among the three type of carbon materials. Later, the BPC-1 was selected to study the influence of pH on the Ba removal from the flowback water as well as the effect of the adsorption time. The 20 ml water was pipetted into a 50 ml vial and different pH were created with nitric acid and KOH solution. The original pH of the flowback water in this work is 5, which is acidic. After being treated with 0.5 g of carbon materials, the mixture of water and carbon materials was filtered with filter paper. The filtered clear water was collected with a 50 ml vial and characterized with inductively coupled

plasma optical emission spectrometry (ICP-OES) to determine the concentration of Ba. The Ba concentrations for the effects of pH and adsorption time were tested once for each sample.

### 3.3.5. SEM and EDAX

The porous carbon materials were characterized with Hitachi S-4700 SEM. The accelerating voltage was set at 5.0 kV. The magnification ranges from 3 μm to 600 μm. The scanning electron microscopy was used to image the surface of the porous carbon materials before and after the water treatment. The SEM experimental section in this study is to display a general micrometer level morphology of the three porous materials. The energy-dispersive X-ray analysis was used to qualitatively determine the barium existence on the carbon materials after water treatment. The known characteristic peaks of Ba were used to compare with the Ba detected from the porous carbon materials (He et al. 2012).

### 3.3.6. Statistical Analysis

The reduction of the barium concentration has been analyzed using Statistical Analysis System (SAS) by SAS Institute, Inc. (Cary, NC) to determine if the activated carbon in this study has significantly decrease the barium from the shale gas flowback water. ANOVA has been conducted on Barium concentrations of different treatments as well as interaction between treatments and carbon loading (alpha=0.05). Furthermore, Duncan's multiple range test was adopted to determine the Duncan grouping and significance between the groups.

## 3.4. Results

### 3.4.1. Processing and Yield

The yields of these process are listed in Table 3.1. The result showed that the char yield is 21.70%. The direct activation process in this study has a yield of 18.20% for BPC-1 based on the weight of original biomass. The yield of BPC-2 is 68.08% based on the weight of char and 14.77% based on the weight of original biomass. Therefore, based on the original biomass weight, the route of BPC-1 has a higher yield and less stages for preparation.

Table 3. 1. Yields of char and activation carbon production.

| Sample and Process | Initial Solid Weight (g) | Final Solid Weight (g) | Yield (%) |
|---|---|---|---|
| BC, Pyrolysis | 100.00 | 21.70 | 21.70 |
| BPC-1, Carbonization | 30.00 | 5.46 | 18.20 |
| BPC-2, Carbonization | 59.91 | 8.85 | 14.77 |

### 3.4.2. $N_2$ Adsorption-desorption Isotherms and Pore Characteristics

As shown in Figure 3.1(a), (b) and (c), a dramatic increase of the nitrogen adsorption appears in all three adsorption isotherms at the low relative pressure region. This is due to improved adsorbent-adsorptive interactions in narrow micropores (Thommes et al. 2015), which results in micropores filling at very low relative pressure. According to the revised IUPAC report (Thommes et al. 2015), the adsorption isotherms in char and both activated carbons displayed a mixture of both type I and type II isotherm. Type I isotherms are commonly found in materials with a broad range of pore size distribution including wider micropores and possible narrow mesopores (less than 2.5 nm). Relative pressure (P/P0) refers to the ratio of partial vapor pressure to saturated pressure: P is partial vapor pressure of N2 in equilibrium with the surface at 77.4K. P0 is saturated

pressure of N2. This isotherm applies to each porous carbon material when the P/P0 is less than 0.8. However, the type I isotherm usually approaches a limiting value which makes the adsorption line parallel to the relative pressure axe. Type II isotherm are given by the adsorption of nitrogen on macroporous or nonporous adsorbents. Type II isotherm could explain the uptake increase after the P/P0 value between 0.8 and 1.0. The unrestricted monolayer-multilayer adsorption taken place at high relative pressure leads to this observation. The curvature in three carbon samples are slowly changed which means that the monolayer coverage and multilayer adsorption onset has a substantial amount of overlapping (Thommes et al. 2015).

Presence of previous isotherm types could not explain the existing difference observed between adsorption and desorption isotherms in each case. Hysteresis was observed in all three isotherm combinations. Hysteresis, mainly due to the capillary condensation, exists as the pore width surpass a critical threshold (usually >4 nm) (Thommes et al. 2015). The hysteresis showed that the isotherm combinations relatively fit into H4 loop very well. The H4 loop means that the adsorption curve is a combination of Types I and II which proves the previous description of isotherm types. H4 loops are often found within micro-mesoporous carbon. Figure 3.1(d) shows the adsorption amount curves at different relative pressures for three porous carbon materials. The average amount of quality adsorbed for BC, BPC-1 and BPC-2 are 75.1, 304.2 and 221.6 $cm^3/g$ at standard conditions for temperature and pressure (STP). STP refers to the condition of being at 273.15 K and an one absolute pressure of atmosphere which is 101.325 kPa. 1 Å means 1 Angstrom. (Equals 0.1 nm). BPC-1 has the highest observation of quality adsorbed. This is due to its highest total volume and relatively high micropore volume (Table 3.2).

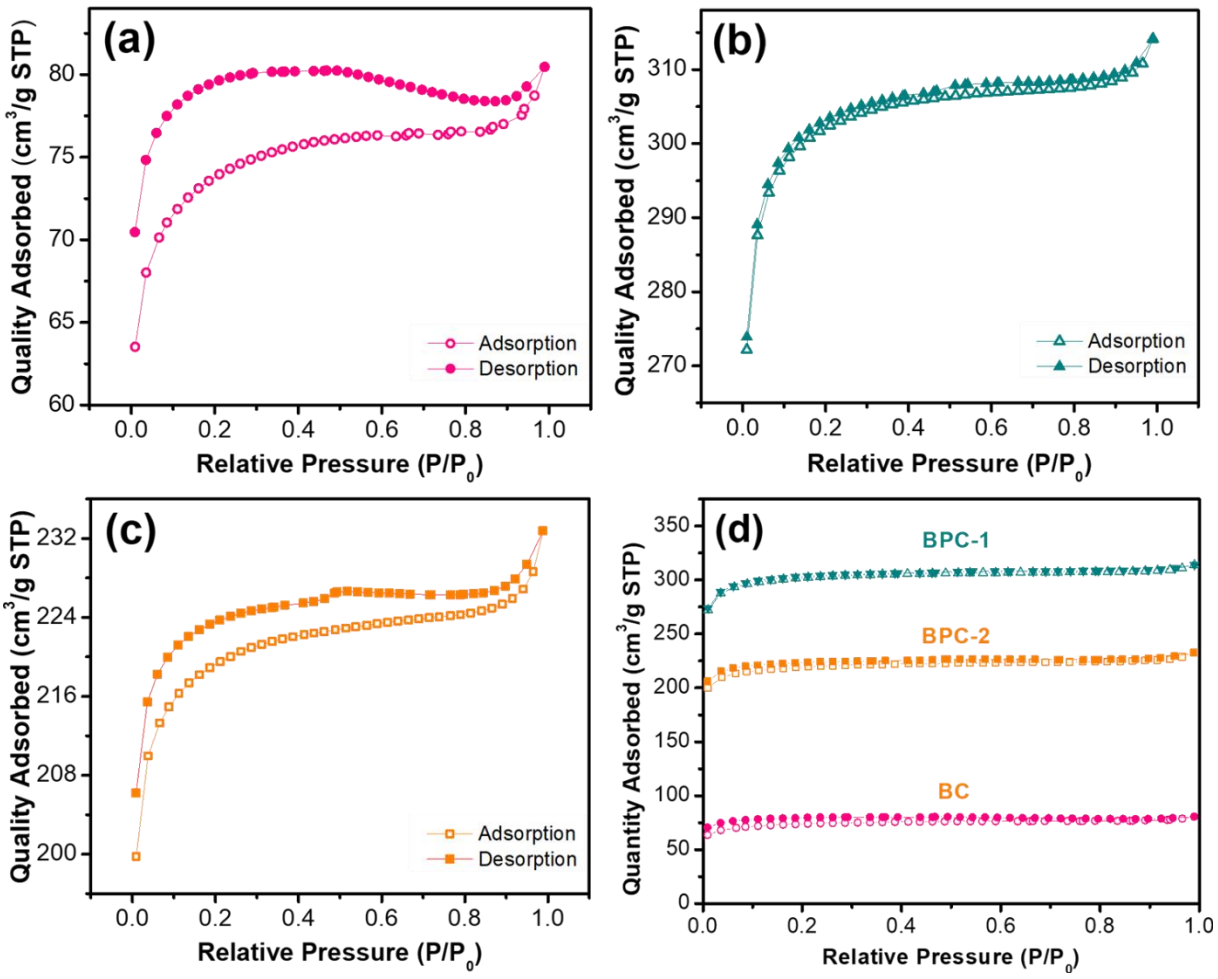


Figure 3. 1. The adsorption-desorption isotherms of porous carbon materials: (a) BC, (b) BPC-1, (c) BPC-2, and (d) all three porous carbon materials with different adsorbed amount levels.

Table 3. 2. The pore characterization of three porous carbons.

| Sample | Surface Area [a] ($m^2/g$) | Micropore Area [b] ($m^2/g$) | Micropore Volume [c] ($cm^3/g$) | Total Pore Volume [d] ($cm^3/g$) | Average Pore Diameter [e] (nm) |
|---|---|---|---|---|---|
| BPC-1 | 1071.43 | 887.60 | 0.39 | 0.49 | 1.81 |
| BPC-2 | 776.59 | 653.65 | 0.29 | 0.36 | 1.85 |
| BC | 261.95 | 192.98 | 0.084 | 0.12 | 1.90 |

a. BET surface area
b. t-Plot micropore area
c. t-Plot micropore volume
d. Single point adsorption
e. BET adsorption average pore diameter.

The pore characterization results from Micromeritics ASAP2020 surface area analyzer were listed in Table 3.2. The BC, BPC-1 and BPC-2 showed a BET surface area of 261.95, 1071.43 and 776.59 $m^2/g$, respectively. The direct carbonization of biomass in this study showed that it could create higher surface area when compared with indirect carbonization. The total micropore volume was respectively 0.49, 0.36 and 0.12 $cm^3/g$. The BPC-1 has a significantly higher total pore volume while the BC has the lowest. The same trend was observed in micro pore volume of three porous carbon materials. The micropore volume percentage of BC, BPC-1 and BPC-2 is 79.6%, 80.1% and 70%. It could be stated that the direct and indirect carbonization routes did not differ significantly in terms of the micropore volume proportion. BPC-1 had a higher micropore area, micropore volume as well as total pore volume. The average pore diameter by the Brunauer-Emmett-Teller (BET) method provided by the surface analyzer is relatively similar for both BCP-1 and BCP-2 porous carbons.

Pore size distribution (PSD) of porous carbon materials can be calculated using gas adsorption and desorption isotherms. The pore size distribution in this work was analyzed with NLDFT (Non-Local Density Functional Theory) (Kupgan et al. 2017). The analysis was conducted with SAIEUS software from Micrometrics Instrument Corporation using Caron-$N_2$, 2D-NLDFT Heterogeneous Surface model. It was widely used in activated carbon which has a high fraction of micropores (Landers et al. 2013). The Figure 3.2(a) showed that the char has a wide range of pores which include micropores (< 2nm) and mesopores (2-50 nm). The pore range observed from NLDFT is 0.4-3.0 nm. A majority of its pores were in microporous range and only a very small portion of accumulative pore volume was attributed to mesoporous range. Figures 3.2(b) and (c) showed that the BPC-1 and BPC-2 are mainly microporous. The pore diameter ranged 0.4-1.5 nm. All three porous materials have a PSD peaked at 0.7 nm.

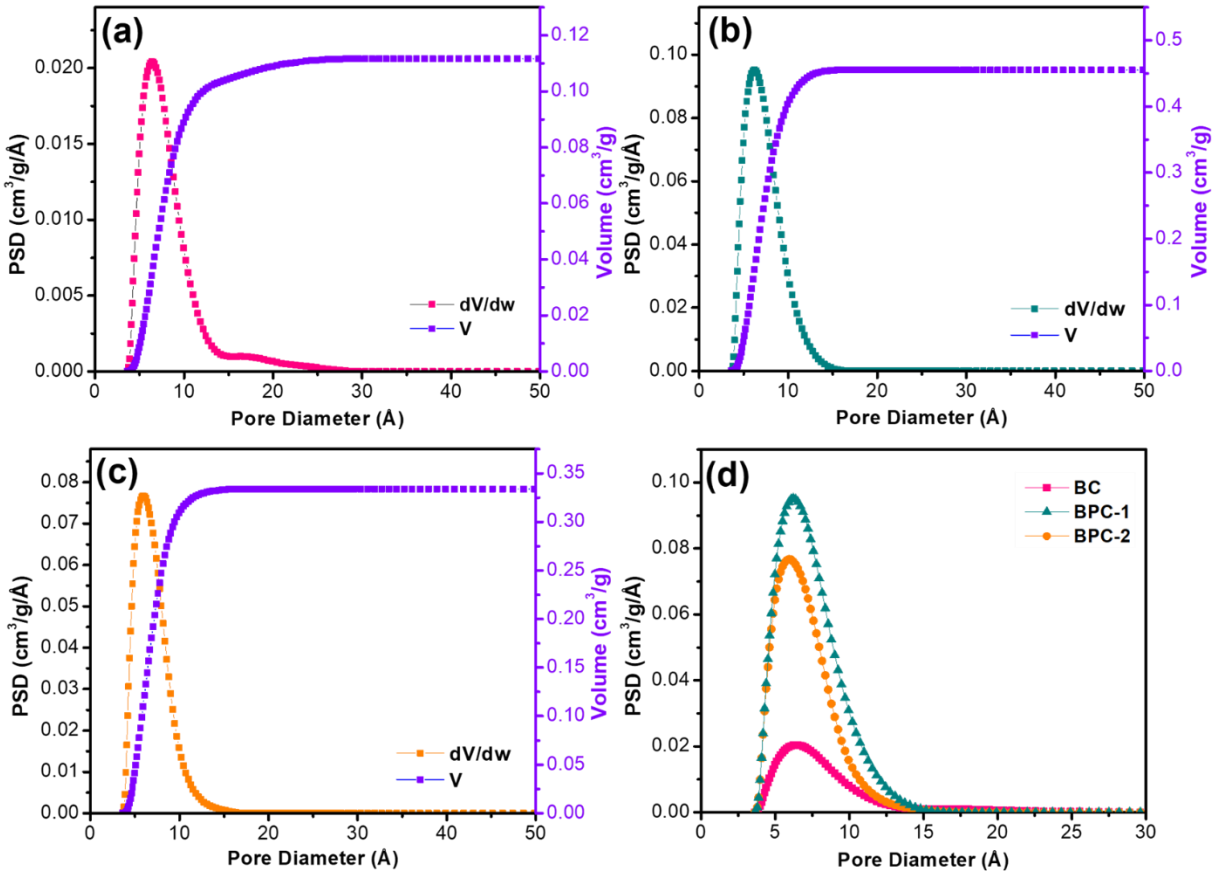


Figure 3. 2. The pore size distribution of different porous carbon materials: (a) BC, (b) BPC-1, (c) BPC-2, and (d) comparison of PSD for three porous carbons.

### 3.4.3. Barium Removal Application

Three different loads (0.1, 0.2 and 0.4 g) of porous carbon materials into a certain volume of wastewater (15 ml). The experimental results showed that all three porous carbon materials could adsorb the barium from actual shale gas water (Figure 3.3). At a relative low ratio of adsorbent to wastewater (≤0.4g:15ml), the barium concentration has decreased 11.3%. The lower carbon load generally gives lower concentration reduction. At the load of 0.4 g, the BPC-1 with a specific

surface area of 1071.43 $m^2/g$ has the highest removal or Ba concentration reduction of 11.3%. The char and BPC-2 did not demonstrate much reduction on Ba concentration with a reduction of Ba concentration of 2.5% and 3.3%, respectively. Although the porous carbon materials are generally considered not performing well when it comes to alkali metal ion removal, our result suggests that it is still a potential way that the removal of Ba could be optimized.

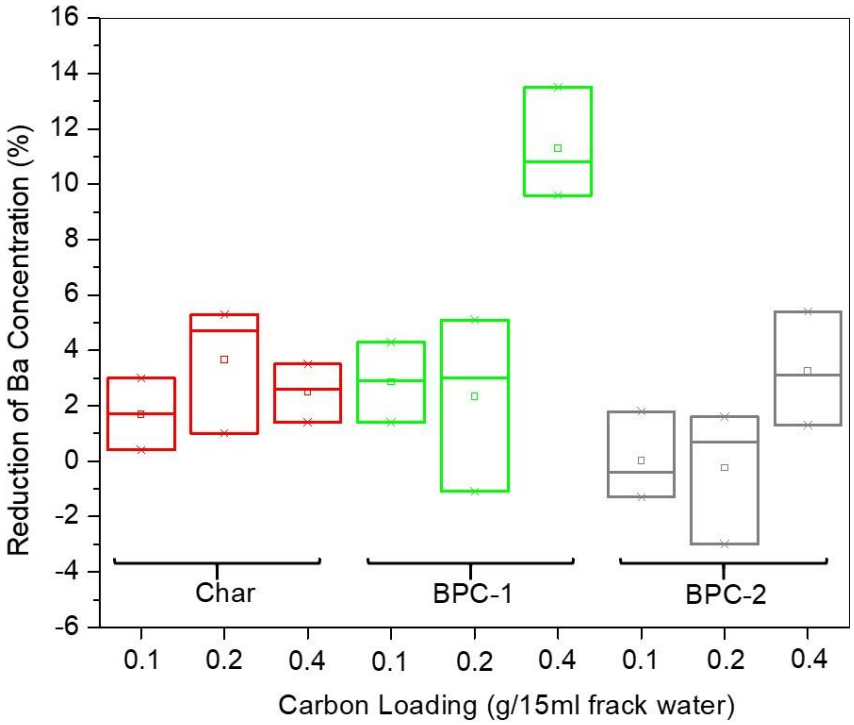


Figure 3. 3. Influence of porous carbon type and load on Ba removal.

Furthermore, the pH effect on the Ba removal was examined in this study using BPC-1 since it has the best performance from previous results. The load in this case is 0.5 g in 20 ml of wastewater for all treatments (Table 3.3). The original pH of the wastewater was 5. Four different pH were created with adjustment of nitric acid and KOH (Table 3.3). The volume change from those

adjustment is negligible. Two adsorption time were applied to the treatment which were 4 hours and 24 hours (Table 3.4). The control water is the original water without any treatment.

Table 3. 3 Ba Reduction at different pH of flowback water.

| Treatment | pH | Static adsorption time | Ba concentration (mg/L) | Reduction (%) |
|---|---|---|---|---|
| 1 | 5, initial | 4 hours | 3153.84 | 3.65 |
| 2 | 1, adjusted | 4 hours | 2985.91 | 8.78 |
| 3 | 7, adjusted | 4 hours | 2988.38 | 8.70 |
| 4 | 10, adjusted | 4 hours | 3059.54 | 6.53 |
| 5 | 13, adjusted | 4 hours | 2883.90 | 11.90 |

Table 3. 4 Ba reduction at different adsorption time.

| Treatment | pH | Static adsorption time | Ba concentration (mg/L) | Reduction (%) |
|---|---|---|---|---|
| Control | 5, initial | - | 3273.29 | - |
| 1 | 5, initial | 4 hours | 3153.84 | 3.65 |
| 2 | 5, initial | 24 hours | 3041.79 | 7.07 |

The results showed that pH did affect the removal of Ba from wastewater. Both acidic (pH<7) and basic (pH>7) have more reduction on Ba concentration when compared with the pH of the initial actual shale gas flowback water (pH=5). From initial pH 5, as the pH increases, more hydroxide ion exists in the solution which covers the surface of metal ions, resulting in higher reduction rates generally when compared with initial pH 5. However, as the pH increases, precipitation was observed when adjusting pH of the wastewater. The removal of metal ions attributed more to chemical precipitation rather than adsorption behavior from the porous carbon. Based on the results shown, the pH 7 is believed to be the optimized pH for better performance on Ba removal.

In addition, significant precipitation was not observed when adjusting the pH to neutral. Besides pH. The results also showed that the time of static adsorption affected the removal of Ba. Allowance of adsorption for 24 hours resulted in a higher concentration decrease when compared to 4 hours of adsorption. The concentration decrease was 7.1% and 3.7% for 24 hours and 4 hours, respectively.

### 3.4.4. Surface Morphology and EDAX

The porous carbon materials of 0.4 g loading were selected to perform the SEM and EDAX. The flowback water has many alkali salts which are both mono-valent and di-valent ions. Typical mono-valent ions include K, Na, Li. Typical di-valent ions include Mg, Ca, Sr, Ba. The anions in the water are chloride and sulfate. The prepared porous carbon materials were characterized with SEM as shown in Figures 3.4, 3.5, as well as 3.6(a) and (b) with magnification of 30 μm and 3 μm, respectively. The porous carbon materials after water treatment were characterized with SEM (Figure 3.4, 3.5, as well as 3.6(c) and (d)). It can be observed in Figure 3.4(c) and (d) that apparent snowflake like salt crystals occurred on the surface. This is due to the adsorption of the salts from the wastewater. The countless crystal flakes observed in Figure 3.4(c) and (d) reveals that the pores on the surface adsorbed salts from the wastewater. The imaging analysis of BPC-1 sample showed that many macro-pores were observed on the surface of the carbon material (Figure 3.5) which was not observed in biochar and BPC-2 (Figures 3.4 and 3.6). Generally, this is due to the etching process taken place on biomass by KOH (Wu and Tseng 2006). Because of the complicated plenty variables of operational parameter as well as the reactivity of different carbon precursor, the mechanism of KOH activation was not well comprehended by far, given it has already been a widely adopted method (Wang and Kaskel 2012). It is generally believed that the reaction between

carbon and potassium hydroxide begins with solid phase then solid-liquid phase involving K reduction, the oxidation of C to $CO_2$ and carbonates and other reactions for active intermediates (Reddy et al. 2015).

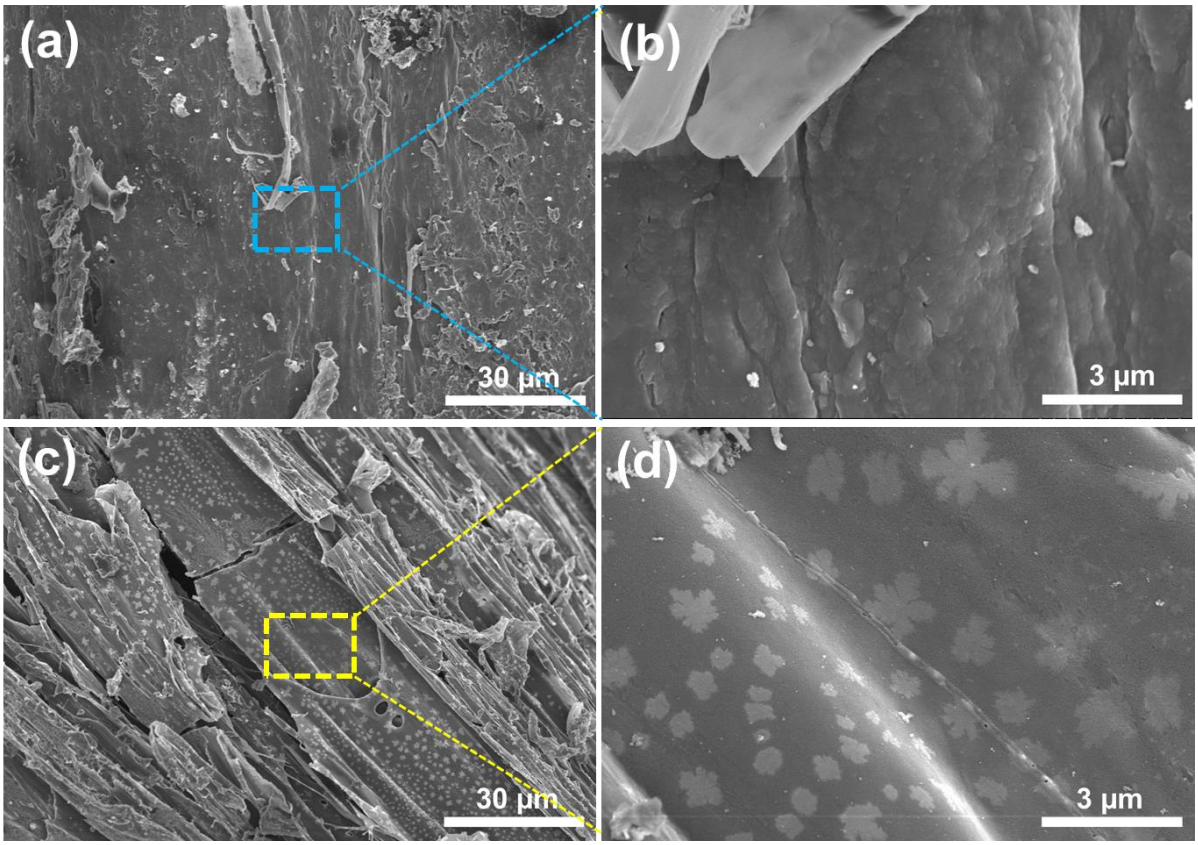


Figure 3. 4 SEM of BC: (a) and (b) before adsorption; (c) and (d) after adsorption.

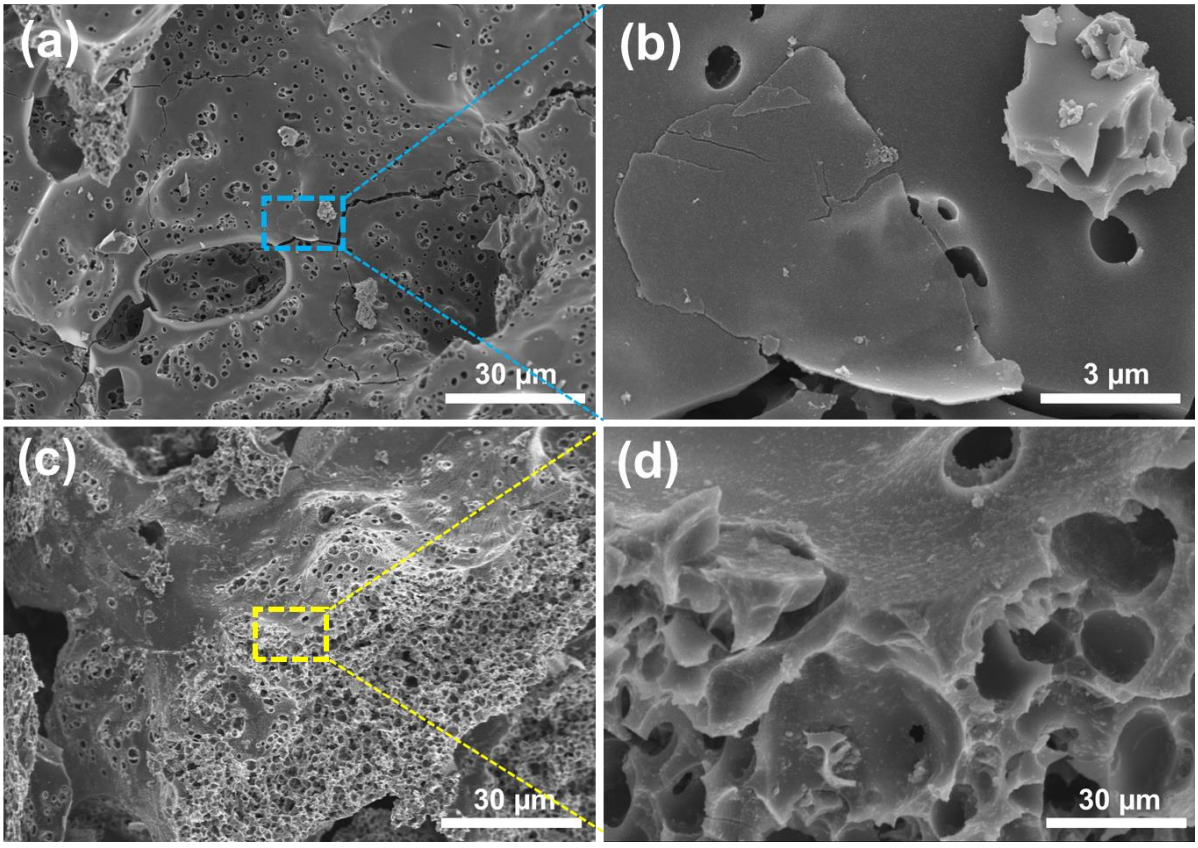


Figure 3. 5 SEM of BPC-1: (a) and (b) before adsorption; (c) and (d) after adsorption.

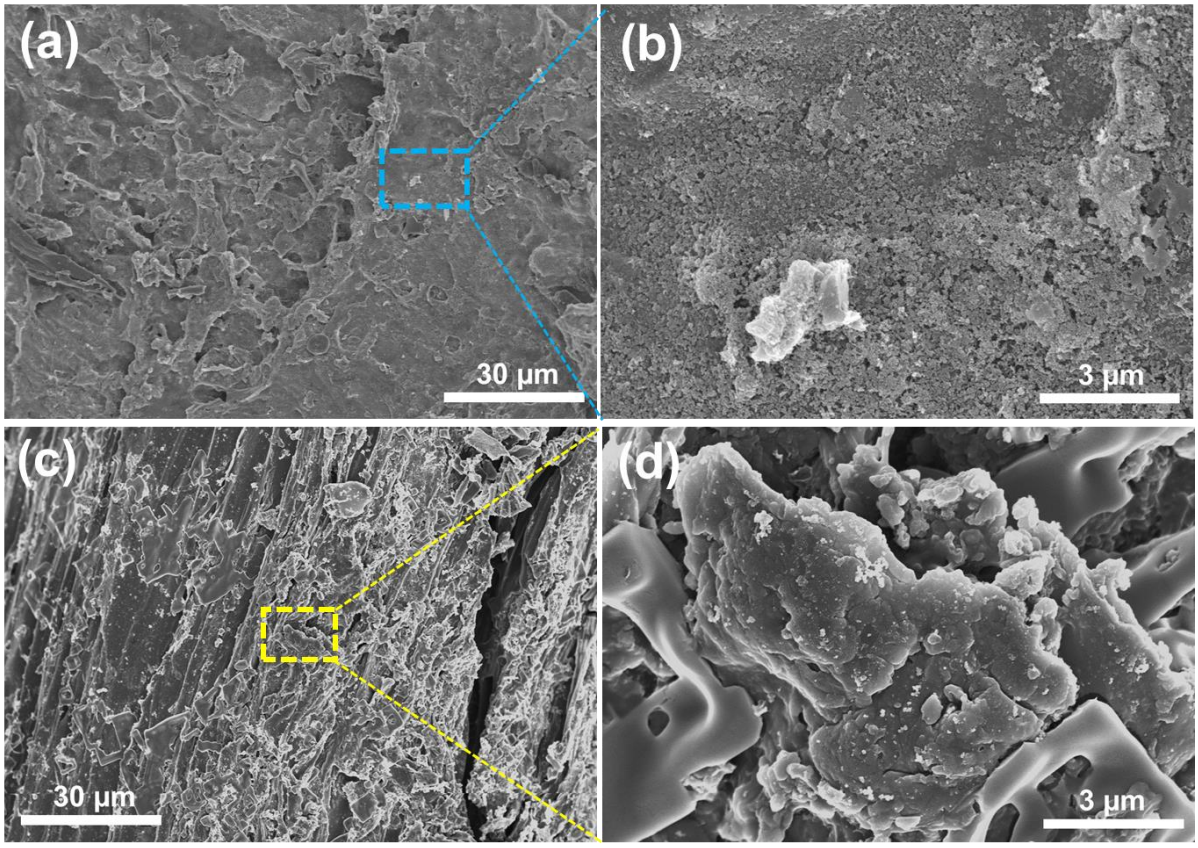


Figure 3. 6. SEM of BPC-02: (a) and (b) before adsorption; (c) and (d) after adsorption.

The typical barium characteristic peaks occurred consecutively four times at 4.5, 4.8, 5.2 and 5.5 keV. The barium peaks were not observed in the spectra of the pristine BPC-1 while these peaks were found in BPCs after wastewater treatment. This observation lays down a proof for adsorption of Ba onto porous carbon materials. The EDAX is considered a qualitative way rather than a quantitative one to characterize the elemental composition of the porous carbon materials. The relative intensity of EDAX showed that BPC-1 and BC has a higher value than BPC-2 which means that there is relatively more Ba being adsorbed on BPC-1 and BC than BPC-2 at the same carbon loading. In addition, the spectra of pristine porous carbon materials confirmed the absence of Ba, which could avoid the influence of pre-existed Ba in porous carbon materials.

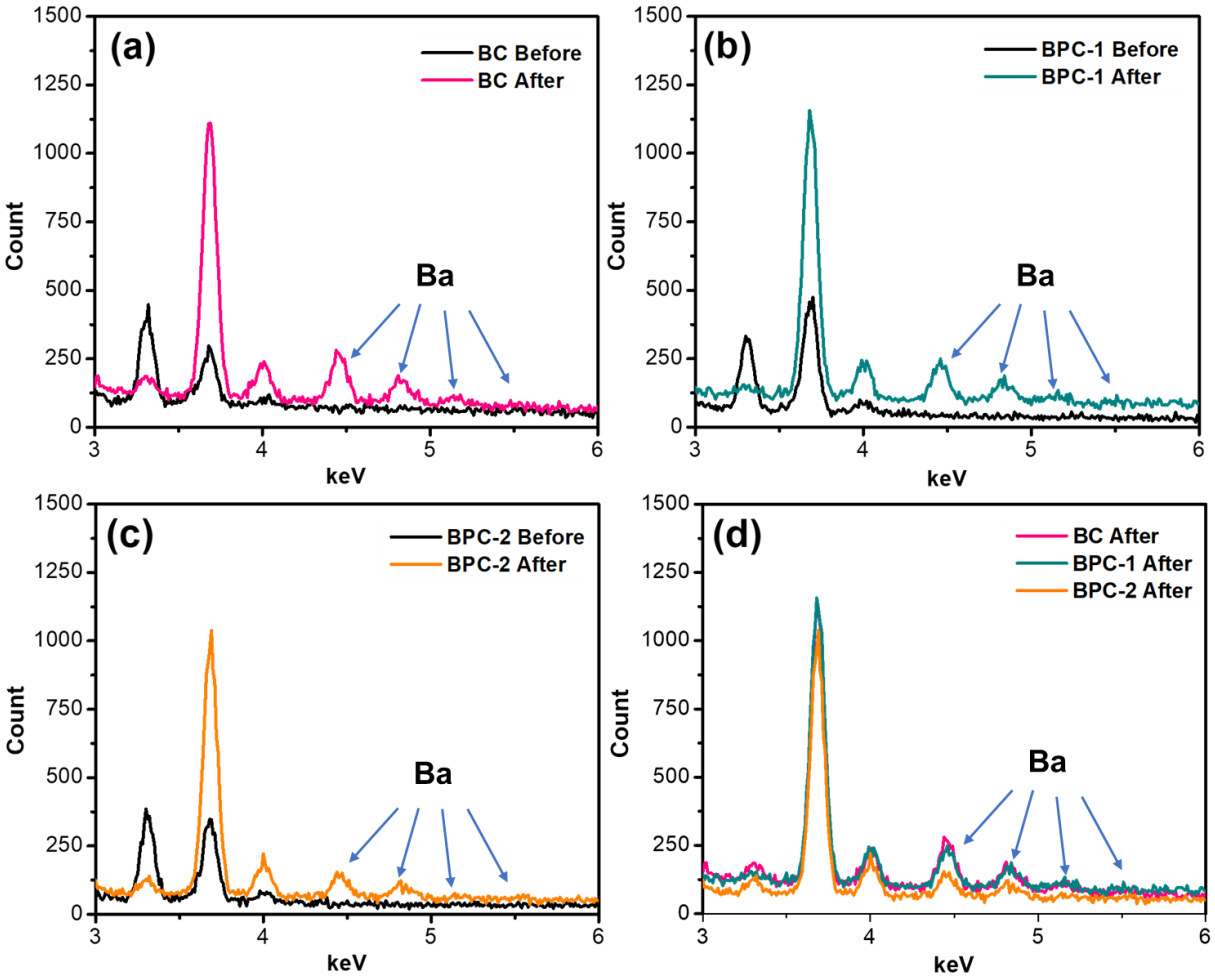


Figure 3. 7. EDAX of three porous carbon materials before and after adsorption of Ba from flowback water.

## 3.5. Discussion

### 3.5.1. Surface Functional Groups and Adsorption

The effectiveness of activated carbon in cleaning up metal ions in polluted water is due to well-developed porosity structures and the existence of various surface functional groups (Lee et al.2018). When it comes to the functional groups of activated carbon derived from hybrid willow biomass, it usually refers to the groups formed from heteroatoms of O and N. A typical content of N is less than 2%, resulting in that the dominant functional groups are actually oxygen containing

groups. Therefore, the surface functional groups that have the most adsorption effort would be oxygen containing groups. The common oxygen containing groups being found in activated carbon have been listed in Figure 3.8, according to the Figueiredo and Pereira (2010). The actual shale gas flowback water has many metal ions. This study has targeted alkali metals with a focus on barium as a represented ion. The barium ion being adsorbed on to surface of the activated carbon materials is mainly due to the surface functional groups which can act as electron donor. Among these oxygen-containing functional groups, pyrone, carbonyl, quinone, and chromene are typical electron donating groups (Montes-Moran et al. 2004, Li et al. 2011). These functional groups were serving as active sites to adsorb Barium ions. Some of the functional groups carry negative charges on the surface, which could serve as binding sites for metal ions (Wilson et al. 2006). There are various mechanisms for the adsorption of Ba from solution. The typical mechanism of biochar or activated carbon includes physical adsorption, electrostatic attraction, complexation, surface precipitation and cation exchange (Li et al. 2017). The Ba adsorption could be attributed mainly to surface precipitation due to the observation of precipitation on the biochar in SEM section. The activated carbon after the treatment does not show visible precipitation, which means that the adsorption of Ba should be mainly physical adsorption and electrostatic attraction (Wilson et al. 2006). The functional groups in Figure 3.8 could serve as active sites to immobilize Ba by complexation such as carbonyl group. As the precipitation grows, the initial crystal of Barium salts ($BaCl_2$ in this work due to overwhelming chlorides showed in EDX results) acts as nucleus and form larger crystal. This could explain the observation of snowflake-like substance on the biochar surface. Due to the well-spread functional groups on the surface of biochar, uniformly precipitation of Ba salts has been formed instead of aggregation. Physical adsorption is another important factor

which could determine the Ba removal, which is highly related to the surface area of the biochar or activated carbon (Halim et al. 2010).

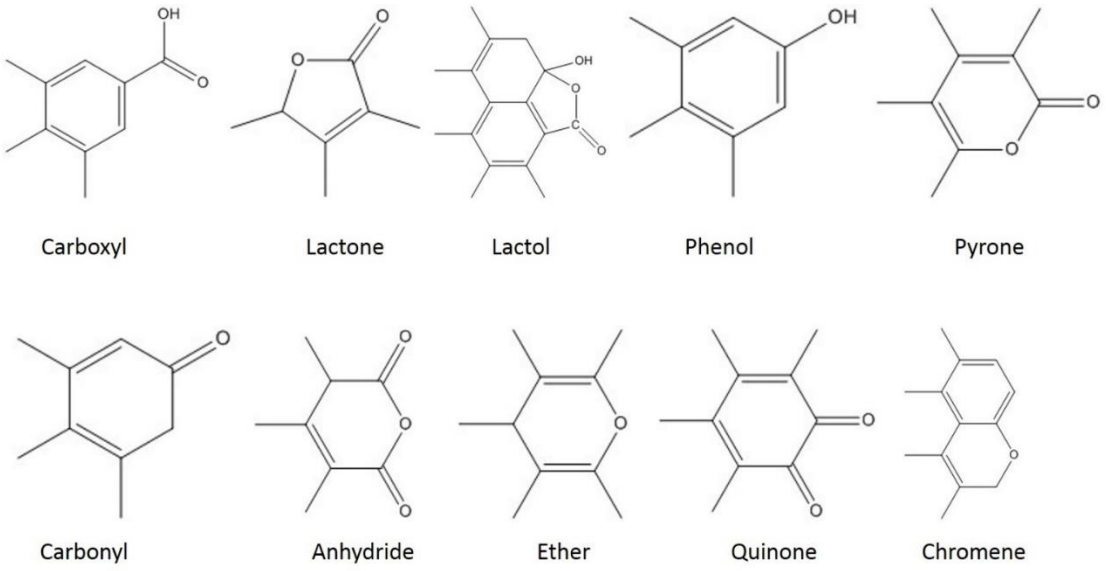


Figure 3. 8 Typical oxygen functional groups found on activated carbon.

### 3.5.2. Direct and Indirect KOH Activation

The conventional process for converting biomass to activated carbon is to first convert the biomass to carbon-rich biochar, which is later activated (Sevilla and Mokaya 2014). The BPC-2 in the current work has been processed in the same way as the conventional method. It has been observed in this study that the direct KOH activation could result in activated carbon (BPC-1) with higher specific surface area and pore volume. Direct KOH activation leading to better porosity is in consistent with the work reported by Balahmar et al (2017).

It is worth noting that for both fabrication methods, the activation of biomass or biochar proceeded according to the following two reactions (Balahmar et al. 2017). The K generated in the step (1) is intercalated within the carbon layers, while $K_2CO_3$ decomposes at high temperature. The porosity in the activated carbon is created by C etching and the release of produced $CO_2$. In addition, the generated $CO_2$ is reacting with the C matrix and yielding CO. The washing process upon activation could further remove any inorganic residues which creates more porosity.

$$KOH + C \rightarrow K + H_2 + K_2CO_3 \quad (1)$$

$$K_2CO_3 \rightarrow K_2O + CO_2 \quad (2)$$

It can be observed from the SEM of both activated carbons prepared by direct and indirect KOH activation that the difference of surface pores. The pores on the surface of BPC-1 is more developed than BPC-2, which means that direct activation from a higher porosity than indirect activation. This work proposes two reasons for this observation. One is related to the wettability of the starting materials. It is believed that the biochar is more hydrophobic than raw biomass since it has less hydrophilic groups than the biomass. These hydrophilic groups could be critical to allow KOH reaching internal matrix. Therefore, the matrix of biomass might be easier for KOH to have a better deposition than the one of biochar. It could lead to more intense reaction of C etching on biomass than biochar, which allow direct KOH activation to have higher specific surface area and pore volume. The other one is regarding reactivity of starting materials. The reactivity of biomass with KOH is relatively higher than the one of biochar with KOH. The main reason is the basal plane of biochar is made of more stable aromatic rings while the structural bone of biomass is made of cellulose chains. Although the biochar has oxygen containing functional groups on the surface, it is just less reactive when compared to side chains of cellulose and hemicellulose in biomass.

Activated carbon prepared from KOH activation has a different surface chemical structure when compared with the biochar prepared by pyrolysis. The effect of KOH activation on the activated carbon product was compared with biochar previously (Oh et al. 2013). The results from this referred work showed that the direct activated carbon has a much higher oxygen content in the forms of carbonyl (C=O), methoxy (C-O), and carboxyl (O-C=O) groups. It indicates that the KOH activation process is beneficial to the development of more O containing functional groups.

The biochar and activated carbon have many differences in term of porosity and surface functional groups. The surface area of biochar is usually much lower than the activated carbon. The surface area of biochar typically ranges from 1 to 200 $m^2/g$ while the activated carbon has 500-1500 $m^2/g$. Pore volume of biochar is about 0.12 $cm^3/g$ in this study while the activated carbon can reach 0.5 $cm^3/g$. It is worth noting that the dominant pore structure of both biochar and activated carbon are both microporous. They can both be used to treat wastewater due to the presence of surface functional groups. It was confirmed by the EDAX that Ba element existing on both materials have similar intensity. Huggins et al (2016) have compared the wood derived biochar and activated carbon for real wastewater treatment. They reported that both biochar and activated carbon could be used for adsorption of alkali metals such as K, Ca and Mg. Biochar is usually applied without further modification after the preparation. Therefore, when compared with highly refined activated carbon, it costs less energy, capital and feedstock to produce (Huggins et al. 2016).

### 3.5.3. Statistical analysis

Analysis of variance (ANOVA) was conducted to test for differences in Ba in relation to treatment and the interaction between treatment and carbon loading. Duncan's multiple range test was used to determine individual differences in treatment and the interaction between treatment and carbon

level. The treatment was assigned as Char, BPC-1 and BPC-2. The interaction with each treatment is the carbon loading which is 0.1 g, 0.2 g, and 0.4 g for each carbon products in 15 ml flowback water. The mean of Ba concentration after BPC-1 treatment has the lowest value. To determine if there is a significant difference between the concentrations, ANOVA was conducted (Table 3.5). Since the results of treatment in terms of carbon type have a P-value of 0.0009<0.05, there is a significant difference on the Ba concentration among different treatments without considering carbon loading. Further analysis using Duncan's multiple range test shows that BPC-1 has a P-value of 0.0012 (<0.05). Table 3.6 indicates that treatment of BPC-1 has a significant difference among three carbon types. From the results above, it is safe to say that the resulted Ba concentration of BPC-1 is significantly lower than the one untreated or treated by BPC-2 and char. The interaction between treatments and carbon amount should be investigated here. To determine the parameter that leading to the difference, the Duncan's multiple range test was conducted (Table 3.7). The distribution of Ba concentration is displayed in the Figure 3.9. The Table 3.7 shows that there is no significant difference in Ba concentrations between 0.1 g and 0.2 g loading of BPC-1. BPC-1 with carbon loading of 0.4 g has resulted a significantly lower Ba concentration than the 0.1 g or 0.2 g loadings since it has a P-value of 0.0001(<0.05). However, this observation only applies to BPC-1. It does not show significant difference in Char nor BPC-2.

Table 3. 5 ANOVA of Ba concentration (mg/L) after adsorption considering treatment and treatment interaction with carbon loading (R-square=0.76).

| Source | DF | Sum of Squares | Mean Square | F-Value | Pr>F |
|---|---|---|---|---|---|
| Treatment | 3 | 102812.40 | 34270.80 | 8.25 | 0.0009 |
| Treatment*Carbon loading | 6 | 155542.53 | 25923.75 | 6.24 | 0.0008 |
| Error | 20 | 83044.16 | 4152.21 | | |
| Corrected Total | 29 | 341399.09 | | | |

Table 3. 6 Descriptive statistics of Ba concentration (mg/L) after treatments with different carbon types.

| Treatment | N | Mean | Standard Deviation | Duncan Grouping |
|---|---|---|---|---|
| Untreated | 3 | 2944.43 | 97.84 | A |
| Char | 9 | 2913.82 | 49.13 | A |
| BPC-1 | 9 | 2866.60 | 140.95 | B |
| BPC-2 | 9 | 2781.65 | 71.76 | A |

Table 3. 7 Descriptive statistics of Ba concentration (mg/L) after treatments with different carbon type at different carbon loading.

| Carbon loading | N | Mean | STDEV | Duncan Grouping |
|---|---|---|---|---|
| Untreated | 3 | 2944.43 | 97.84 | A |
| Char-0.1g | 3 | 2893.63 | 37.73 | A |
| Char-0.2g | 3 | 2836.46 | 69.30 | A |
| Char-0.4g | 3 | 2869.70 | 30.92 | A |
| BPC-1-0.1g | 3 | 2859.79 | 42.59 | A |
| BPC-1-0.2g | 3 | 2874.11 | 92.87 | A |
| BPC-1-0.4g | 3 | 2611.05 | 58.20 | B |
| BPC-2-0.1g | 3 | 2942.50 | 46.67 | A |
| BPC-2-0.2g | 3 | 2950.50 | 71.36 | A |
| BPC-2-0.4g | 3 | 2848.47 | 60.58 | A |

### 3.6. Conclusion

Activated carbons from two different routes of KOH carbonization have been successfully fabricated. The yield study showed that the direct KOH carbonization has a higher yield than indirect carbonization. The porosity parameters of activated carbon such as specific surface area, total pore volume and microporous volume are relatively higher in direct KOH activation. The Barium adsorption test showed that both activated carbons can be used to adsorb Ba from actual shale gas flowback water. The activated carbon from direct KOH carbonization has a higher

reduction rate which is 11.3% at a relatively low carbon loading (carbon to water mass ratio at 1:38).

### 3.6. References

Bagheri, N. and Abedi, J., 2009. Preparation of high surface area activated carbon from corn by chemical activation using potassium hydroxide. Chemical engineering research and design, 87(8), pp.1059-1064.

Balahmar, N., Al-Jumialy, A.S. and Mokaya, R., 2017. Biomass to porous carbon in one step: directly activated biomass for high performance CO 2 storage. Journal of Materials Chemistry A, 5(24), pp.12330-12339.

Budinova, T., Savova, D., Tsyntsarski, B., Ania, C.O., Cabal, B., Parra, J.B. and Petrov, N., 2009. Biomass waste-derived activated carbon for the removal of arsenic and manganese ions from aqueous solutions. Applied Surface Science, 255(8), pp.4650-4657.

Danish, M. and Ahmad, T., 2018. A review on utilization of wood biomass as a sustainable precursor for activated carbon production and application. Renewable and Sustainable Energy Reviews, 87, pp.1-21.

Dutta, S., Bhaumik, A. and Wu, K.C.W., 2014. Hierarchically porous carbon derived from polymers and biomass: effect of interconnected pores on energy applications. Energy & Environmental Science, 7(11), pp.3574-3592.

Figueiredo, J.L. and Pereira, M.F.R., 2010. The role of surface chemistry in catalysis with carbons. Catalysis Today, 150(1-2), pp.2-7.

He, H., Bleby, T.M., Veneklaas, E.J., Lambers, H. and Kuo, J., 2012. Precipitation of calcium, magnesium, strontium and barium in tissues of four Acacia species (Leguminosae: Mimosoideae). PLoS one, 7(7), p.e41563.

Halim, A.A., Aziz, H.A., Johari, M.A.M. and Ariffin, K.S., 2010. Comparison study of ammonia and COD adsorption on zeolite, activated carbon and composite materials in landfill leachate treatment. Desalination, 262(1-3), pp.31-35.

Huggins, T.M., Haeger, A., Biffinger, J.C. and Ren, Z.J., 2016. Granular biochar compared with activated carbon for wastewater treatment and resource recovery. Water research, 94, pp.225-232.

Kadirvelu, K., Thamaraiselvi, K. and Namasivayam, C., 2001. Removal of heavy metals from industrial wastewaters by adsorption onto activated carbon prepared from an agricultural solid waste. Bioresource technology, 76(1), pp.63-65.

Kılıç, M., Apaydın-Varol, E. and Pütün, A.E., 2012. Preparation and surface characterization of activated carbons from Euphorbia rigida by chemical activation with ZnCl2, K2CO3, NaOH and H3PO4. Applied surface science, 261, pp.247-254.

Kobya, M., Demirbas, E., Senturk, E. and Ince, M., 2005. Adsorption of heavy metal ions from aqueous solutions by activated carbon prepared from apricot stone. Bioresource technology, 96(13), pp.1518-1521.

Kupgan, G., Liyana-Arachchi, T.P. and Colina, C.M., 2017. NLDFT pore size distribution in amorphous microporous materials. Langmuir, 33(42), pp.11138-11145.

Kwapinski, W., Byrne, C.M., Kryachko, E., Wolfram, P., Adley, C., Leahy, J.J., Novotny, E.H. and Hayes, M.H., 2010. Biochar from biomass and waste. Waste and Biomass Valorization, 1(2), pp.177-189.

Landers, J., Gor, G.Y. and Neimark, A.V., 2013. Density functional theory methods for characterization of porous materials. Colloids and Surfaces A: Physicochemical and Engineering Aspects, 437, pp.3-32.

Lee, K.K., Han, G.Y., Yoon, K.J. and Lee, B.K., 2004. Thermocatalytic hydrogen production from the methane in a fluidized bed with activated carbon catalyst. Catalysis Today, 93, pp.81-86.

Lee, C.L., H'ng, P.S., Paridah, M.T., Chin, K.L., Rashid, U., Maminski, M., Go, W.Z., Nazrin, R.A.R., Rosli, S.N.A. and Khoo, P.S., 2018. Production of bioadsorbent from phosphoric acid pretreated palm kernel shell and coconut shell by two-stage continuous physical activation via N2 and air. Royal Society open science, 5(12), p.180775.

Li, H., Dong, X., da Silva, E.B., de Oliveira, L.M., Chen, Y. and Ma, L.Q., 2017. Mechanisms of metal sorption by biochars: biochar characteristics and modifications. Chemosphere, 178, pp.466-478.

Li, N., Ma, X., Zha, Q., Kim, K., Chen, Y. and Song, C., 2011. Maximizing the number of oxygen-containing functional groups on activated carbon by using ammonium persulfate and improving the temperature-programmed desorption characterization of carbon surface chemistry. Carbon, 49(15), pp.5002-5013.

Liou, T.H., 2010. Development of mesoporous structure and high adsorption capacity of biomass-based activated carbon by phosphoric acid and zinc chloride activation. Chemical Engineering Journal, 158(2), pp.129-142.

Meng, R., Chen, T., Zhang, Y., Lu, W., Liu, Y., Lu, T., Liu, Y. and Wang, H., 2018. Development, modification, and application of low-cost and available biochar derived from corn straw for the

removal of vanadium (v) from aqueous solution and real contaminated groundwater. RSC Advances, 8(38), pp.21480-21494.

Montes-Morán, M.A., Suárez, D., Menéndez, J.A. and Fuente, E., 2004. On the nature of basic sites on carbon surfaces: an overview. Carbon, 42(7), pp.1219-1225.

Oh, G.H., Yun, C.H. and Park, C.R., 2003. Role of KOH in the one-stage KOH activation of cellulosic biomass. Carbon letters, 4(4), pp.180-184.

Reddy, K.S.K., Al Shoaibi, A. and Srinivasakannan, C., 2015. Impact of process conditions on preparation of porous carbon from date palm seeds by KOH activation. Clean Technologies and Environmental Policy, 17(6), pp.1671-1679.

Sakanishi, K., Wu, Z., Matsumura, A., Saito, I., Hanaoka, T., Minowa, T., Tada, M. and Iwasaki, T., 2005. Simultaneous removal of H2S and COS using activated carbons and their supported catalysts. Catalysis Today, 104(1), pp.94-100.

Savova, D., Apak, E., Ekinci, E., Yardim, F., Petrov, N., Budinova, T., Razvigorova, M. and Minkova, V., 2001. Biomass conversion to carbon adsorbents and gas. Biomass and Bioenergy, 21(2), pp.133-142.

Shaffer, D.L., Arias Chavez, L.H., Ben-Sasson, M., Romero-Vargas Castrillón, S., Yip, N.Y. and Elimelech, M., 2013. Desalination and reuse of high-salinity shale gas produced water: drivers, technologies, and future directions. Environmental science & technology, 47(17), pp.9569-9583.

Tay, T., Ucar, S. and Karagöz, S., 2009. Preparation and characterization of activated carbon from waste biomass. Journal of Hazardous Materials, 165(1-3), pp.481-485.

Thommes, M., Kaneko, K., Neimark, A.V., Olivier, J.P., Rodriguez-Reinoso, F., Rouquerol, J. and Sing, K.S., 2015. Physisorption of gases, with special reference to the evaluation of surface area and pore size distribution (IUPAC Technical Report). Pure and Applied Chemistry, 87(9-10), pp.1051-1069.

Velten, S., Boller, M., Köster, O., Helbing, J., Weilenmann, H.U. and Hammes, F., 2011. Development of biomass in a drinking water granular active carbon (GAC) filter. Water Research, 45(19), pp.6347-6354.

Wang, J. and Kaskel, S., 2012. KOH activation of carbon-based materials for energy storage. Journal of Materials Chemistry, 22(45), pp.23710-23725.

Williams, P.T. and Reed, A.R., 2006. Development of activated carbon pore structure via physical and chemical activation of biomass fibre waste. Biomass and Bioenergy, 30(2), pp.144-152.

Wilson, K., Yang, H., Seo, C.W. and Marshall, W.E., 2006. Select metal adsorption by activated carbon made from peanut shells. Bioresource technology, 97(18), pp.2266-2270.

Woolf, D., Amonette, J.E., Street-Perrott, F.A., Lehmann, J. and Joseph, S., 2010. Sustainable biochar to mitigate global climate change. Nature communications, 1, p.56.

Wu, F.C. and Tseng, R.L., 2006. Preparation of highly porous carbon from fir wood by KOH etching and CO2 gasification for adsorption of dyes and phenols from water. Journal of Colloid and Interface Science, 294(1), pp.21-30.

# Chapter 4. Chemical and Structural Variation of Lignocellulosic Biomass during Oxidative Torrefaction

## 4.1. Abstract

Four lignocellulose biomass feedstocks have been treated with mediate oxidative torrefaction at 250 °C in air flow with different heating rates (5, 1 and 0.5 °C/min). The treated samples were characterized by thermogravimetric analysis (TGA), elemental analysis, Fourier-transform infrared spectroscopy (FTIR) as well as the scanning electron microscope (SEM). The yield study showed that lower heating rates resulted in decreased weight of biochar. The thermal degradation curves revealed that as the heating rate slows down, the decomposition process of all lignocellulose biomass feedstocks peaked at lower temperatures. The elemental analysis indicated that the lower heating rates could decrease the H/C ratio. The infrared spectroscopy also showed a reduced holocellulose intensity occurred as the heating rate decreased. SEM images of all treated samples showed that the pore development was observed even at mediate level of torrefaction. The oxidative torrefaction could be used as a feedstock improvement for biomass conversion to biochar and activated carbon.

## 4.2. Introduction

Torrefaction is commonly used in the pre-treatment of biomass feedstock for thermal conversions. It is typically classified to three levels as light (200-235 °C), mediate (235-275 °C) and severe (275-300 °C) torrefaction (Chen et al. 2015). It is essentially a mild pyrolysis process. The torrefaction is typically conducted in nitrogen or with low contents of oxygen at temperature 200-300 °C. It was previously reported that the thermal degradation temperatures of three major components of biomass are 220-315 °C for hemicellulose, 315-400 °C for cellulose and from 160 up to 900 °C for lignin (Yang et al. 2007). Therefore, hemicellulose and lignin are speculated to be degraded during mediate level torrefaction.

Torrefaction process could turn the biomass into a more water-resistible solid substance that having a higher energy density (Uslu et al. 2008, Rousset et al. 2012). The efficiency of the pyrolysis of torrefied biomass is higher than that of untreated raw biomass (Chen et al. 2012, Meng et al. 2012). However, the additional operating costs are required because of energy consumption and nitrogen supply. The cost could be saved by carrying out the operation in air atmosphere, namely oxidative torrefaction. Oxidative torrefaction is conducted in the presence of oxygen. Different from nitrogen torrefaction, the oxidative gas could facilitate the depolymerization of the feedstock and oxidize the released volatiles generated along with it, which affects the char yield. (Rousset et al. 2012). The mechanism behind two types of torrefaction are slightly different. The traditional nitrogen torrefaction, non-oxidative, was compared with the air torrefaction, oxidative, at various superficial velocities (Chen et al. 2013). The other study by the same author reveal that thermal degradation of biomass in nitrogen was manipulated by the internal heat and mass transfer while the surface oxidation was dominating the oxidative torrefaction of biomass (Chen et al. 2014). Oxidative torrefaction has been studied on sawdust with a TG and fluidized bed reactor (Wang et al. 2013). It has been compared with the traditional torrefaction which takes place in nitrogen. They found that there is no major difference between oxidative and traditional non-oxidative methods in terms of density, heating value and energy yield.

Biomass is a common source for production of high porous carbon materials. Wood, particularly, has a natural porous structure which could be a great advantage for producing activated carbon (Greil et al. 1998, Gibson 2012). Activated carbon can be fabricated by plenty of forest operational residue. Logs are usually the major values of a tree, while the remaining, still a substantial amount, is usually treated as waste that later being used as fuel such as tops, branches, stump and bark (Wang et al. 2017).

Theoretically, wood has many natural structures which could form pores after pyrolysis. In softwood, pore forming structure includes resin canals, longitudinal tracheids (20-70μm) and radial ray tracheids, which could be seen by human eyes with simple magnification tools. Smaller pore forming structure includes parenchyma cells, pit and. In hardwood, major pore forming structures are vessels, tracheid, ray cells, perforation plates and pits. Grass are natural plants which could produce a large amount of biomass. In the Northeast United States, switchgrass (*Panicum virgatum*), a perennial warm season bunchgrass, is one of the dominant species. It is primarily used for soil conservation, forage production, game cover, fiber, heat production and more recently as a bioenergy crop for ethanol and butanol. *Miscanthus giganteus* is another species which could provide a large amount of biomass. It is a perennial grass hybrid of *miscanthus sinensis* and *miscanthus sacchariflorus*. This grass is a full sun plant which can grow 8-12 ft (240-360 cm) tall each year. The grass also has a porous structure which could be utilized to prepare porous carbon products. For examples, the microstructure of miscanthus grass stalk shows countless natural pores around 0.2 μm (Klimek et al. 2018).

In general, these biomass feedstocks tend to absorb moisture from air and are not easy to grind. Many drawbacks are not beneficial to the processing and storage, such as high water contents, a low energy densities and large bulk volumes (Chen et al. 2011a). Due to these drawbacks, the potential of biomass being used to convert to high porous carbon materials has been concerned. It is worth noting that one critical property improved during the torrefaction process is the grind-ability of the biomass. Since the conversion of biomass feedstock to targeted products such as activated carbon materials could be affected by the original particle size, the grinding property could improve the feedstock by decreasing the energy consumption by easier process to reduce the feedstock size. It has been reported that torrefaction of biomass at 300 °C could reduce the grinding

energy to the lowest (Phanphanich and Mani 2011). Therefore, to improve the quality of raw biomass, oxidative torrefaction can be introduced before any other processing. There are several parameters which will influence the yield and properties of the treated biomass such as biomass composition, particle size, residence temperature and time, ramping rate and the gas atmosphere.

The heating rate influence on the torrefied biomass have been rarely studied in the oxidative torrefaction. The main objective of this work is to investigate the heating rate effect on the oxidative torrefaction of four biomass species which are widely presented in the Northeast United States. These biomass feedstocks include two wood species, eastern white pine and hybrid willow as well as two grassy species, miscanthus grass and switchgrass. Three different heating rates (5, 1, 0.5 °C/min) have been applied to investigate the effect on structural and chemical changes taking placing in different biomasses. Yield study, thermal decomposition, elemental analysis, surface function groups, as well as morphology was examined.

## 4.3. Material and Method

### 4.3.1. Materials

Eastern white pine, hybrid willow, miscanthus grass and switchgrass were four lignocellulosic biomasses selected in this study. Eastern white pine (*Pinus strobus*) was provided by West Virginia University Research Forest. The hybrid willow (*Salix spp.*) was selected since it is a potential short rotation crop in the Northeast US region. Switchgrass (*Panicum virgatum*) was chosen due to its abundance across the whole US. The miscanthus grass (*Miscanthus x giganteus*) could serve as a supplementary energy source for switchgrass and was promoted as a high biomass yield crop. The four lignocellulosic biomasses were chipped and milled into particles less than 1.0 mm before further processing.

### 4.3.2. Torrefaction Process

The original 10 g of each biomass species were placed into the 450 ml alumina combustion boat (203 mm×102 mm, AdValue Technology, Tucson, AZ). The biomass boat was then placed on the heating zones of a tube furnace (Lindberg, Model 23-891). The torrefaction process used in this study included three stages. The first stage was the low temperature rapid increase from room temperature (20 °C) to 110 °C. The ramping rate in this stage was 10 °C/min. The second stage was the torrefaction stage where temperature was increased from 110 to 250 °C. The ramping rate was 5.0, 1.0, and 0.5 °C/min, respectively. The third stage was the resident stage where the samples were held at 250 °C for 2 hours. Then the furnace was cooled down to room temperature. The final weight of the biomass char after torrefaction was recorded which was then used for yield calculation.

### 4.3.3 Thermogravimetric Analysis (TGA)

The 5-10 mg of biomass were weighted in an aluminum pan. The biomass was heated inside the TG chamber with a certain nitrogen flow (20 ml/min). The heating rate was 10 °C/min. The temperature was raised from 25 to 800 °C. Then the sample was cooled down with a decreasing temperature rate of 10 °C/min.

### 4.3.4. Elemental Analysis

The elemental analysis was carried out with a CHNS elemental analyzer. Each biomass was tested for three times and a mean value of elemental composition was collected. The test was carried out

with ASTM standard D-5373-08. Oxygen content was later calculated based on the weight percentage sum of these four elements.

### 4.3.5. Fourier-transform Infrared Spectroscopy (FTIR)

Digilab FTS 7000/UMA 600 Fourier Transform Infra-Red (FTIR) Spectrometer was used in this study. The torrefied biomass samples along with the untreated were grinded with a mortar grinder into even fine particles. The transmittance spectra were collected for all the samples tested.

### 4.3.6. Scanning Electron Microscope (SEM)

The torrefied biomass samples were characterized with Hitachi S-4700 SEM. The accelerating voltage was set at 5.0 kV. The magnification ranges from 5 μm to 100 μm. The scanning electron microscope was used to image the surface of the torrefied biomass. The SEM experimental section in this study is to display a general micrometer level morphology of the torrefied biomass.

## 4.4. Results

### 4.4.1. Yield by Different Heating Rates

The influence of torrefaction heating rates on the weight loss of the four biomass species were listed in Table 4.1. The slower the heating rate the lower the yield of torrefied char. When the heating rate decreased from 5 to 0.5 °C/min, the yield of torrefied biomass was decreased from 71.6% to 67.7% for hybrid willow. This is mainly due to the longer heating time and further loss of the volatiles. The yield was decreased 5.3, 3.7, 7.0 and 3.9%, for miscanthus grass, eastern white pine, switchgrass and hybrid willow, respectively. The woody biomass was less affected by the

torrefaction rates than herbaceous biomass. It is worth nothing that the yield of eastern white pine presented a slight difference under 1 and 0.5 °C/min. Among the four lignocellulosic biomass feedstocks, switchgrass is the most susceptible to the torrefaction process while the eastern white pine is the least.

Table 4. 1. Yield by species after air torrefaction under different ramping rates.

| | Heating Rates (°C/min) | | |
|---|---|---|---|
| Species | 5 | 1 | 0.5 |
| Miscanthus Grass, % | 74.4 | 72.9 | 69.1 |
| Eastern White Pine, % | 80.8 | 76.9 | 77.1 |
| Switchgrass, % | 65.7 | 61.0 | 58.7 |
| Hybrid Willow, % | 71.6 | 70.3 | 67.7 |

### 4.4.2. Thermo-gravimetrical Analysis (TGA)

Thermal degradation processes of four species in nitrogen have been plotted in Figure 4.1. The lower temperatures (200-330 C°) began the thermal degradation of hemicellulose and lignin, resulting in the evaporation of individual compounds. At higher temperatures (330-400 °C), the steep curve indicated the degradation of cellulose. Above 400 °C, a semi-coke was formed by removal of carbonyl, carboxylic groups as well as hydrogen, along with the methyl groups being reduced, was the resulted from removal of oxygen in char and reduction of aliphatic frames (Jeguirim et al. 2010, Collura et al. 2015).

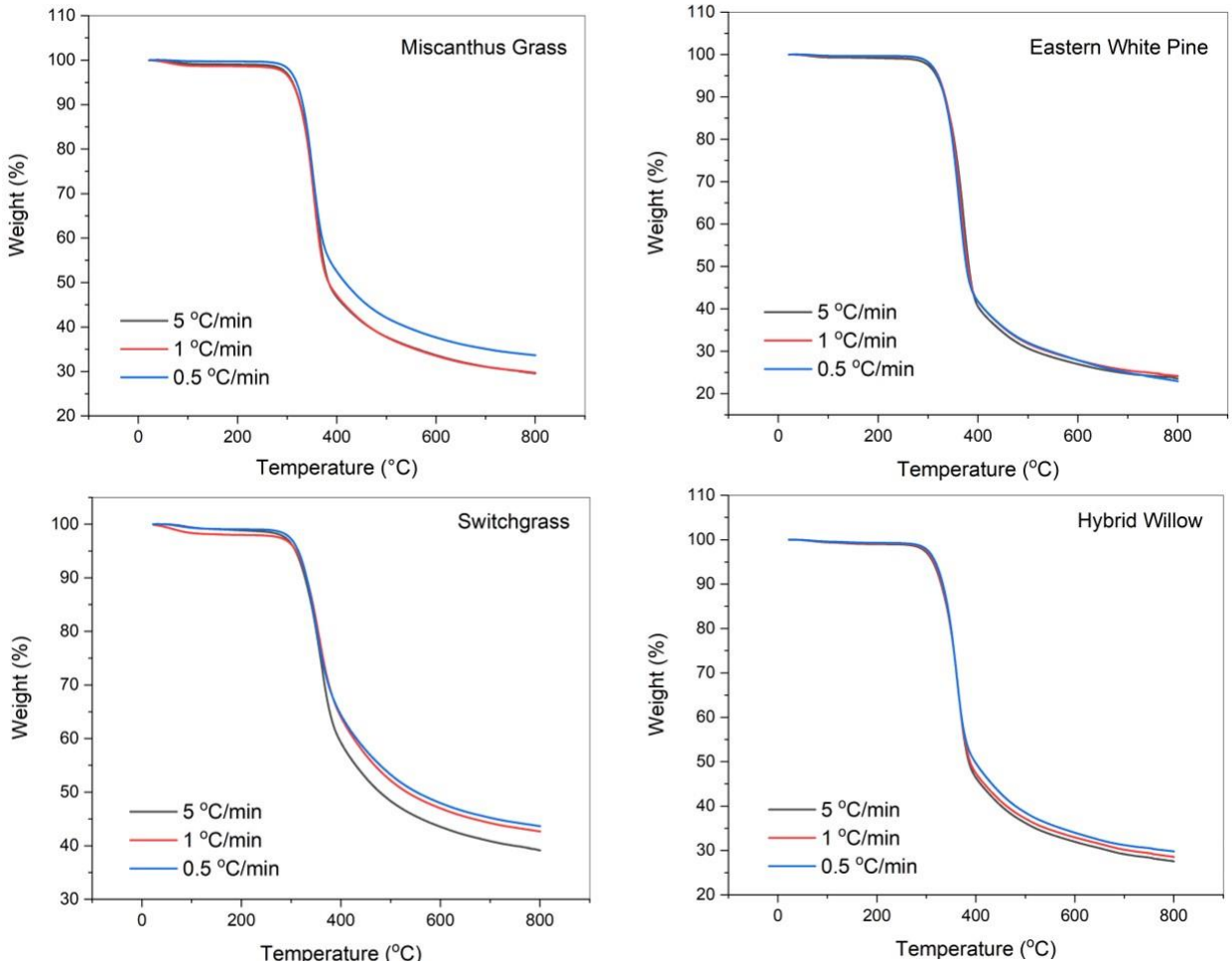


Figure 4. 1. TGA of four lignocellulosic biomasses.

As shown in Table 4.2, the major degradation peaks are in a temperature range of 350-371 °C for all four species at different heating rates. As the rate decreased, the major degradation peak shifted to lower temperature for all species. When the heating rate decreased from 5 to 0.5 C/min, the degradation peak decreased 9 and 10 °C for eastern white pine and switchgrass, respectively. The residue amount generally increased in all species except eastern white pine. However, the residue mass percentage of eastern white pine at different heating rates are similar while the other three has a decreasing residue mass percentage as the heating rates decreases. It indicated that the heating

rate presented the least influence on eastern white pine residue among all species while it affected the most on switchgrass. The results showed that slower heating rate yielded higher residue amount in general. Oktaee et al. (2017) investigated the willow degradation and found that the willow biomass has a degradation peak at 365 °C, which is similar to what we found in this work, the willow degradation peak shifted to lower temperatures (360-364 °C). The peak shift indicated that lower heating rate could make willow easier to degrade during the pyrolysis.

Table 4. 2. Pyrolysis parameters of four species by TGA.

| | Heating Rate (°C/min) | Peak (°C) | Residue (%) |
|---|---|---|---|
| Miscanthus grass | 5 | 356 | 29.5 |
| | 1 | 354 | 29.7 |
| | 0.5 | 351 | 32.8 |
| Eastern white pine | 5 | 371 | 23.6 |
| | 1 | 366 | 24.2 |
| | 0.5 | 362 | 23.0 |
| Switchgrass | 5 | 360 | 39.1 |
| | 1 | 355 | 42.7 |
| | 0.5 | 350 | 43.6 |
| Hybrid willow | 5 | 364 | 27.6 |
| | 1 | 362 | 28.5 |
| | 0.5 | 360 | 29.8 |

### 4.4.3. Elemental Analysis

Since the degradation peaks have been significantly shifted in the torrefied eastern white pine and switchgrass samples when the heating rate alters, they were selected to conduct elemental analysis to further investigate the effect of the heating rates on biomass. When the torrefaction was carried out, the hydrogen content in both species decreased as the heating rate slows. The influence on O and C does not have a general trend with regard to eastern white pine. However, in switchgrass, the C weight percentage has increased while the O weight percentage has decreased as the heating rate drops. As it shows in the atomic ratio ($C_xH_yO_z$), the H/C ratios decrease as the heating rate

decreases. The H/C ratio for eastern white pine ranged from 1.30 to 1.34 and for switchgrass. It was between1.04 abd 1.18. The O/C ratio for eastern white pine was from 0.62 to 0.67 and for switchgrass varied from 0.66 to 0.69. The O ratio decreased in switchgrass while it no general trend was observed for eastern white pine. Our results showed that the influence of the heating rate affected more on hydrogen than on oxygen content.

Table 4. 3. Elemental analysis of biomass treated with three different heating rates.

| Sample | C (wt.%) | H (wt.%) | O (wt.%) | N (wt.%) | $C_xH_yO_z$ |
|---|---|---|---|---|---|
| Pine-5 | 51.32 | 5.75 | 42.43 | 0.50 | $CH_{1.34}O_{0.62}$ |
| Pine-1 | 51.88 | 5.64 | 41.62 | 0.86 | $CH_{1.30}O_{0.60}$ |
| Pine-0.5 | 49.71 | 5.39 | 44.30 | 0.60 | $CH_{1.30}O_{0.67}$ |
| SG-5 | 49.04 | 4.83 | 45.35 | 0.78 | $CH_{1.18}O_{0.69}$ |
| SG-1 | 49.60 | 4.60 | 44.70 | 1.09 | $CH_{1.11}O_{0.68}$ |
| SG-0.5 | 50.51 | 4.38 | 44.19 | 0.92 | $CH_{1.04}O_{0.66}$ |

### 4.4.4. Surface Functional Groups of Torrefied Biomass.

The surface function groups of torrefied biomass were investigated with FTIR (Figures 4.2-4.4). The functional groups varied between 750 and 4000 $cm^{-1}$ and the fingerprint area was from 750-2000 $cm^{-1}$. Holocellulose characteristic peaks can be found at several wavenumbers. The characteristic band of 3600-3200 refers to the O-H stretching on the cellulose and hemicellulose molecule. As show in Figure 4.2, the peak of this band decreased as the heating rate lowered. The C-H stretching at 2900 $cm^{-1}$ also presented decreased peak intensity along with the declining heating rate. In the fingerprint area, the most import characteristic peak of holocellulose occurred at 1022 $cm^{-1}$ that signaled the decreased intensity of C-O bond as the heating rate slowed down, due to more holocellulose was degraded. The peak shift at 1720 $cm^{-1}$ was another proof that the holocellulose was degraded. It is worth noting that the hemicellulose is a major component that has been degraded during torrefaction process at 250 °C. Cellulose is relatively more thermal stable

than hemicellulose. It is believed only part of the cellulose was degraded during this process. The weakened peak at 897 $cm^{-1}$ reveals that the amorphous cellulose was degrading (Figure 4.2). It is believed that the crystal cellulose does not degrade at this temperature. The fingerprint area further reveals that the lignin degradation by appearing peak was at both 1590 and 1506 $cm^{-1}$. The FTIR analysis of hybrid willow showed similar results as switchgrass stated previously (Figure 4.3). The results on miscanthus and eastern white pine indicated that the characteristic peak at 1022 $cm^{-1}$ showed both species having degradation of holocellulose at temperature 250 °C (Figure 4.4). However, the peak intensity does not change dramatically like the other two species.

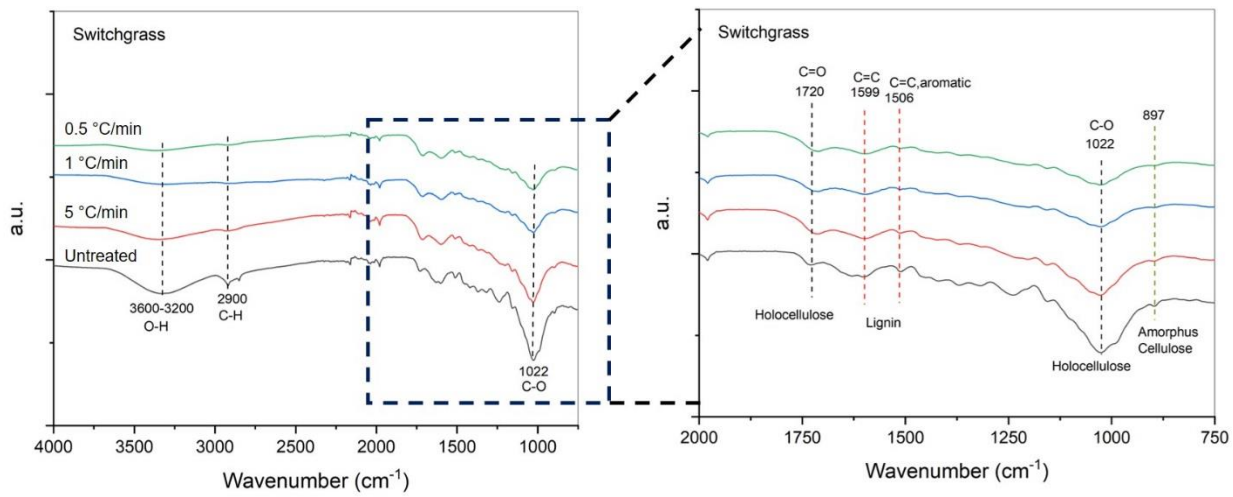


Figure 4. 2. FTIR analysis of switchgrass biomass under torrefaction treatment with different heating rates.

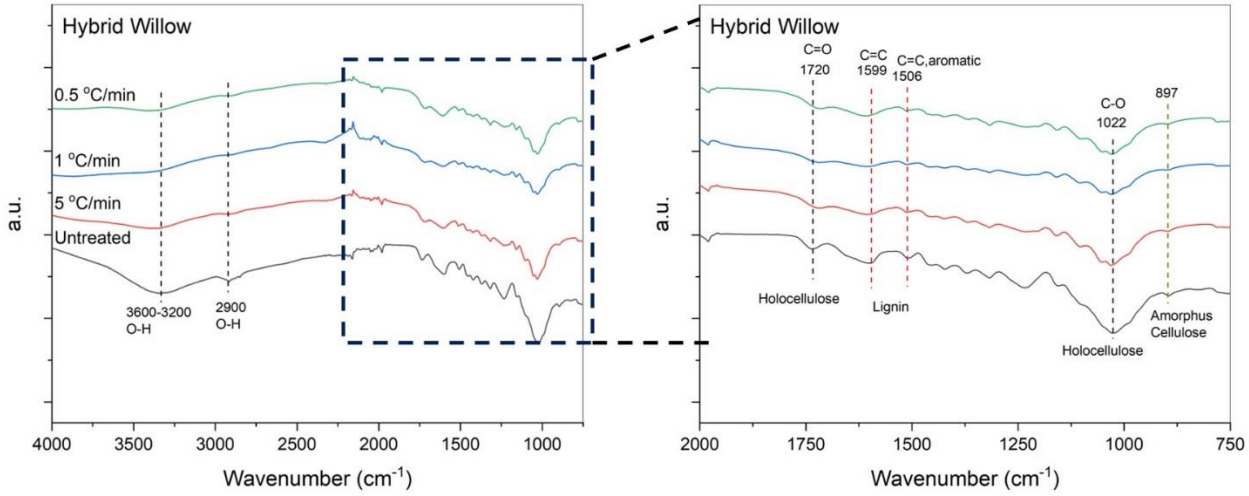


Figure 4. 3. FTIR analysis of hybrid willow biomass under torrefaction treatment with different heating rates.

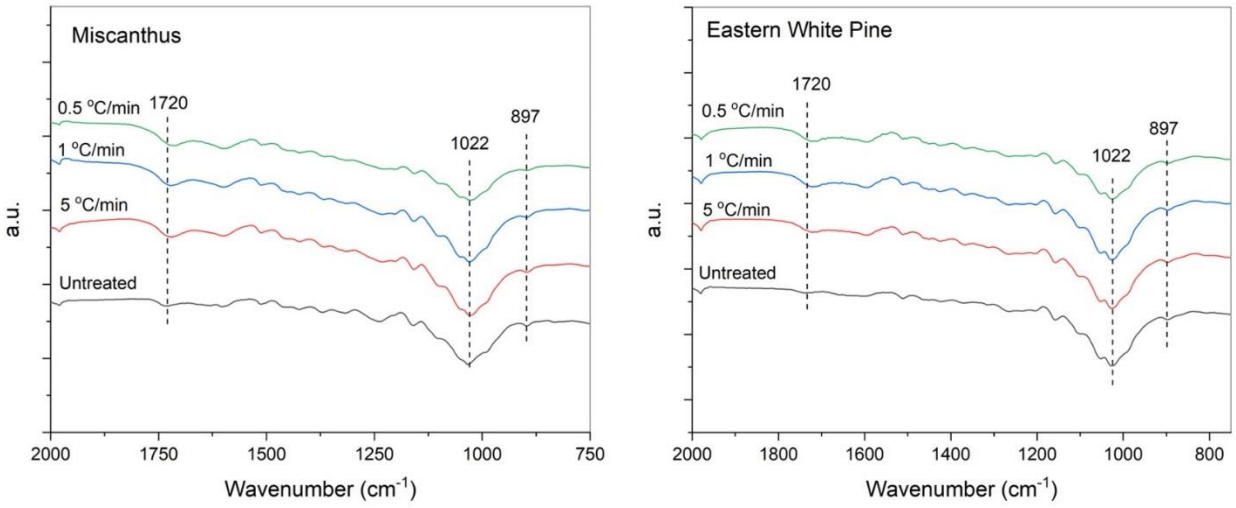


Figure 4. 4. FTIR analysis of miscanthus grass and eastern white pine.

### 4.4.5. Morphology

The morphology was imaged for two herbaceous species (Figure 4.5) and two woody species (Figure 4.6) treated at different heating rates. For miscanthus grass, the pores at the surface of the plant cell wall started to open due to the low thermal stability of the pore membrane components. At the heating rate of 0.5 °C/min, clear pores emerged on the plant cell wall surface. It is observed that the pores of switch grass started to open at 0.5 °C/min while no surface pores presented at 5 °C/min. It is observed that the open pores of the eastern white pine occurred on the cell wall due to the degradation of the pits on the tracheids. However, the hybrid willow displayed very limited pore development. The vessels and pits area remained closed despite of being treated with different heating rates. The oxidative torrefaction under different heating rates does not change the tubular structure of biomass.

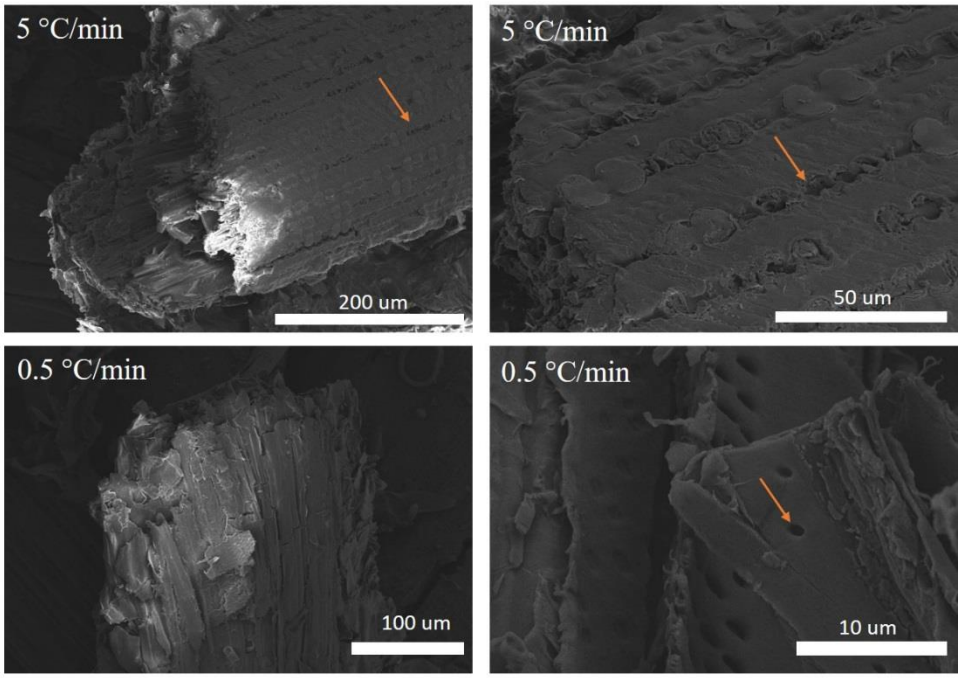


Figure 4. 5. SEM image of two grass species after torrefaction at 250 °C with heating rates of 5 and 0.5 °C/min.

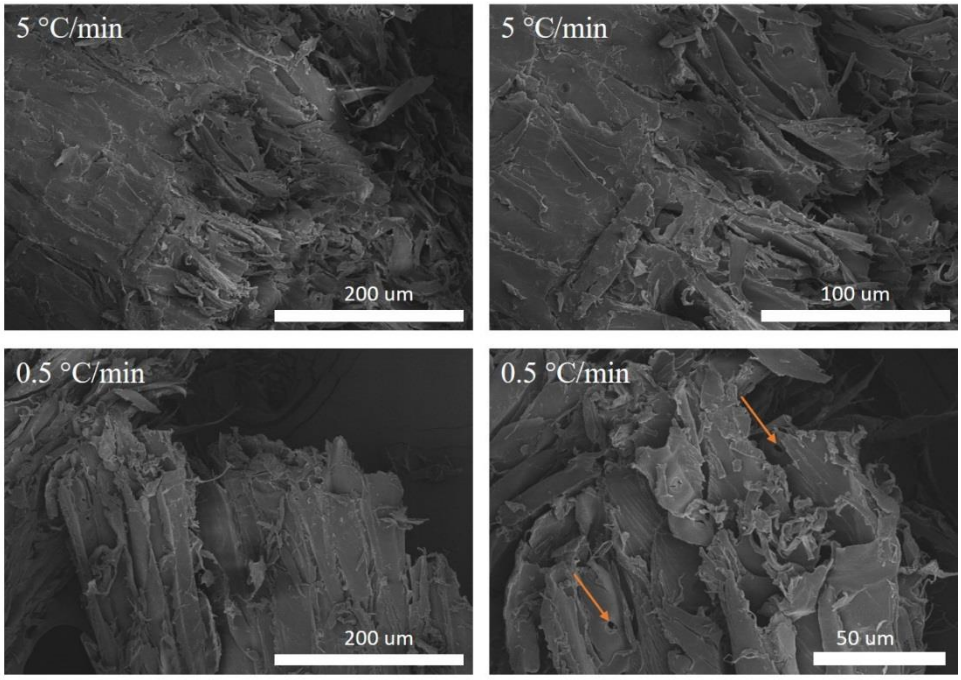


Figure 4. 6. SEM image of two wood species after torrefaction at 250 °C with heating rates of 5 and 0.5 °C/min.

## 4.5. Discussion

### 4.5.1. Effect of oxidative torrefaction

The oxidative torrefaction used in this study is mediate level. It was chosen since light level cannot provide significant effect on biomass structure and chemicals while severe level could result in too much weight loss. The similar results were found in a study that biomass was pretreated at three levels: light (220 °C), mild (250 °C) and severe (280 °C) (Chen et al. 2011b). The mediate process in this work typically resulted in a brown solid, a condensable liquid with high water content, acetic acid as well as other oxygenates, along with gas volatiles such as $CO_2$, CO and a low amount methane (Tumuluru et al. 2012). The pyrolyzed char yield in this work showed that the residual amount generally increased along with the increased heating rates. Therefore, the torrefaction could be used to increase the yield of the final pyrolyzed char. This is due to the more holding time which eventually leads to more degradation of the lignocellulosic biomass. The result is in consistence with a previously reported work (Wang et al. 2013). Another study showed that more residence time could increase the char yield of treated sawdust due to that more cross-linking reaction could take place as the holding time increase. (Tapasvi et al. 2012).

### 4.5.2. Surface chemistry and pore development

The heating rate affected the hydrogen more than on the oxygen content. It is in consistence with a previous work (Chen et al. 2012) that revealed the similar outcome as well as a close range of H/C and O/C ratios. It is worth noting that besides O atom, the tested two species showed the other heteroatom N with a weight range from 0.5 to 1.09%. The N element is beneficial to form diverse functional groups from O atom which is critical in common applications such as energy storage and adsorption (Liu et al. 2016, Horikawa et al. 2012).

This work found that the torrefied char retained its functional groups after mediate torrefaction despite of the decreased intensity of certain functional groups due to degradation. This is consistent with the work reported by Zheng et al. (2017). Their results indicated that as the heating rates decreases, the cellulose and hemicellulose have undergone dehydration and thermal degradation reactions, which decrease the free hydroxyl content from the molecules surface. The acetyl groups on the chain of hemicellulose have been detached from the main molecule and become acetic acid. The degradation of lignin evidenced by the peak shift at 1599 and 1506 $cm^{-1}$ in this study further proved lignin was thermally decomposed. Regarding to the lignin molecule, the ether bond was broken and released methoxy. The slower torrefaction pretreatment could promote the reduction of hydroxyl group and cause more decarboxylation.

It was reported that the same miscanthus grass had clear open pores under thermal treatment from 240-280 °C torrefaction (Gucho et al. 2015). Awoyemi and Jones (2011) investigated the western red cedar under heat treatment at 220 °C for 1 hour and 2 hours. The wood anatomy under SEM also indicated that at even lower temperature compared to this work, the pits were open on the tracheids. The opening of the pores was mainly caused by the degradation of the hemicellulose. The tubular structure of the biomass in this work was not changed after the torrefaction treatment. This is due to that the frame inside the lignocellulosic biomass is not easily influenced by the oxidative reaction (Chen et al. 2014). The oxidation process only decomposes hemicellulose and a limited part of lignin while it does not degrade the major bone structure which is cellulose.

### 4.6. Conclusion

The weight of the torrefied char decreased duo to further release of moisture and volatiles of biomass. The thermal degradation of different biomass demonstrated a peak shift to lower

temperatures because of the hemicellulose degradation during oxidative torrefaction. The H/C decreased with reduced heating rates. The H/C ratio in selected wood and grass species decreased from 1.34 to 1.30 and 1.18 to 1.04, respectively. The hemicellulose, amorphous cellulose and lignin were decomposed based on the weakened characteristic peaks or shifted peaks. The oxidative torrefaction could reserve the tubular structure of biomass and create porosity at mediate level of 250 °C. The oxidative torrefaction is a potential pretreatment to improve biomass quality for further conversion.

## 4.7. References

Awoyemi, L. and Jones, I.P., 2011. Anatomical explanations for the changes in properties of western red cedar (Thuja plicata) wood during heat treatment. Wood science and technology, 45(2), pp.261-267.

Chen, W.H. and Kuo, P.C., 2011a. Torrefaction and co-torrefaction characterization of hemicellulose, cellulose and lignin as well as torrefaction of some basic constituents in biomass. Energy, 36(2), pp.803-811.

Chen, W.H., Hsu, H.C., Lu, K.M., Lee, W.J. and Lin, T.C., 2011b. Thermal pretreatment of wood (Lauan) block by torrefaction and its influence on the properties of the biomass. Energy, 36(5), pp.3012-3021.

Chen, W.H., Lu, K.M. and Tsai, C.M., 2012. An experimental analysis on property and structure variations of agricultural wastes undergoing torrefaction. Applied energy, 100, pp.318-325.

Chen, W.H., Lu, K.M., Liu, S.H., Tsai, C.M., Lee, W.J. and Lin, T.C., 2013. Biomass torrefaction characteristics in inert and oxidative atmospheres at various superficial velocities. Bioresource technology, 146, pp.152-160.

Chen, W.H., Lu, K.M., Lee, W.J., Liu, S.H. and Lin, T.C., 2014. Non-oxidative and oxidative torrefaction characterization and SEM observations of fibrous and ligneous biomass. Applied energy, 114, pp.104-113.

Chen, W.H., Peng, J. and Bi, X.T., 2015. A state-of-the-art review of biomass torrefaction, densification and applications. Renewable and Sustainable Energy Reviews, 44, pp.847-866.

Collura, S., Azambre, B. and Weber, J.V., 2005. Thermal behaviour of Miscanthus grasses, an alternative biological fuel. Environmental Chemistry Letters, 2, pp.95-99.

Gibson, L.J., 2012. The hierarchical structure and mechanics of plant materials. Journal of the royal society interface, 9(76), pp.2749-2766.

Greil, P., Lifka, T. and Kaindl, A., 1998. Biomorphic cellular silicon carbide ceramics from wood: I. Processing and microstructure. Journal of the European Ceramic Society, 18(14), pp.1961-1973.

Gucho, E., Shahzad, K., Bramer, E., Akhtar, N. and Brem, G., 2015. Experimental study on dry torrefaction of beech wood and miscanthus. Energies, 8(5), pp.3903-3923.

Horikawa, T., Sakao, N., Sekida, T., Hayashi, J.I., Do, D.D. and Katoh, M., 2012. Preparation of nitrogen-doped porous carbon by ammonia gas treatment and the effects of N-doping on water adsorption. Carbon, 50(5), pp.1833-1842.

Jeguirim, M., Dorge, S., Loth, A. and Trouvé, G., 2010. Devolatilization kinetics of miscanthus straw from thermogravimetric analysis. International Journal of Green Energy, 7(2), pp.164-173.

Klímek, P., Wimmer, R., Meinlschmidt, P. and Kúdela, J., 2018. Utilizing Miscanthus stalks as raw material for particleboards. Industrial crops and products, 111, pp.270-276.

Liu, S., Chen, X., Li, X., Huo, P., Wang, Y., Bai, L., Zhang, W., Niu, M. and Li, Z., 2016. Nitrogen- and oxygen-containing micro–mesoporous carbon microspheres derived from m-aminophenol formaldehyde resin for supercapacitors with high rate performance. RSC Advances, 6(92), pp.89744-89756.

Meng, J., Park, J., Tilotta, D. and Park, S., 2012. The effect of torrefaction on the chemistry of fast-pyrolysis bio-oil. Bioresource technology, 111, pp.439-446.

Oktaee, J., Lautenschläger, T., Günther, M., Neinhuis, C., Wagenführ, A., Lindner, M. and Winkler, A., 2017. Characterization of willow bast fibers (Salix spp.) from short-rotation plantation as potential reinforcement for polymer composites. BioResources, 12(2), pp.4270-4282.

Phanphanich, M. and Mani, S., 2011. Impact of torrefaction on the grindability and fuel characteristics of forest biomass. Bioresource technology, 102(2), pp.1246-1253.

Rousset, P., Macedo, L., Commandré, J.M. and Moreira, A., 2012. Biomass torrefaction under different oxygen concentrations and its effect on the composition of the solid by-product. Journal of Analytical and Applied Pyrolysis, 96, pp.86-91.

Tapasvi, D., Khalil, R., Skreiberg, Ø., Tran, K.Q. and Grønli, M., 2012. Torrefaction of Norwegian birch and spruce: an experimental study using macro-TGA. Energy & Fuels, 26(8), pp.5232-5240.

Tumuluru, J.S., Sokhansanj, S., Wright, C.T. and Kremer, T., 2012. GC Analysis of Volatiles and Other Products from Biomass Torrefaction Process, Advanced Gas Chromatography-Progress in Agricultural, Biomedical and Industrial Applications, Mustafa Ali Mohd (Ed.), ISBN: 978-953-51-0298-4, InTech.

Uslu, A., Faaij, A.P. and Bergman, P.C., 2008. Pre-treatment technologies, and their effect on international bioenergy supply chain logistics. Techno-economic evaluation of torrefaction, fast pyrolysis and pelletisation. Energy, 33(8), pp.1206-1223.

Wang, C., Peng, J., Li, H., Bi, X.T., Legros, R., Lim, C.J. and Sokhansanj, S., 2013. Oxidative torrefaction of biomass residues and densification of torrefied sawdust to pellets. Bioresource technology, 127, pp.318-325.

Wang, L., Barta-Rajnai, E., Skreiberg, Ø., Khalil, R., Czégény, Z., Jakab, E., Barta, Z. and Grønli, M., 2017. Impact of torrefaction on woody biomass properties. Energy Procedia, 105, pp.1149-1154.

Zheng, Y., Tao, L., Yang, X., Huang, Y., Liu, C., Gu, J. and Zheng, Z., 2017. Effect of the torrefaction temperature on the structural properties and pyrolysis behavior of biomass. BioResources, 12(2), pp.3425-3447.

# Chapter 5. Effect of Intermediate Pyrolysis Temperature for Lignocellulosic Biochar on the Physicochemical Properties of Eventual Activated Carbon

## 5.1. Abstract

Lignocellulosic biomass is a critical resource for the production of activated carbon with high specific surface area and well-developed porosity. It has a great potential to be used in many industrial applications such as energy storage and adsorption. In this work, four species of lignocellulosic biomass were converted to activated carbon materials using an intermediate pyrolysis process. Two pyrolysis temperatures were applied in this process at 450 and 1000 °C to study the differences of resulted biochar and activated carbon materials. Nitrogen adsorption and desorption test, scanning electron microscope as well as Raman spectroscopy were used to characterize the samples. The results showed that the samples from all species showed a higher specific surface area and a better porosity development at 450 °C than at 1000 °C. The SEM showed that intermediate pyrolysis of 1000 °C could lead to the observed collapse of the pore development. The increased $I_D/I_G$ ratio from Raman spectra of both biochar and activated carbon samples indicated that the higher pyrolysis temperature could result in the increase of amorphous portion in the carbon rich materials and the decrease of graphitization degree.

## 5.2. Introduction

Environmental and energy policies have been a driving factor that increases the global demand of activated carbon, which is a common adsorbent in many industry sectors and has a great potential of being used for energy storage and agricultural operations (Pallarés et al. 2018). The typical sources as starting materials to prepare activated carbon include coal (Chingombe et al. 2015), biomass (Abioye et al. 2015), polymers (Hayashi et al. 2000) and other organic chemicals (Chen et al. 2015). A new demand for this material is to be produced with renewable, affordable and abundant source to replace the fossil ones (Pallarés et al. 2018).

A typical preparation for activated carbon is to thermally degrade the biomass precursor to biochar then be activated by either physical or chemical activation agent (Ahmadpour et al. 1996). The physical activation agents typically include carbon dioxide and steam (Chang et al. 2000). The chemical activation agents could be KOH, $ZnCl_2$, $H_2SO_4$, $H_3PO_4$, etc. (Bagheri and Abedi 2009; Liou 2010; Karagoz et al. 2008). The chemical activation could yield better pore development and higher specific surface area. However, it always comes with extra steps for cleaning the final product and creates contaminants. The physical activation is more environmentally friendly despite that this type of activation produces moderate porosity and surface area.

Many previous studies were conducted on converting biomass to carbon rich byproduct such as biochar and activated carbon that are focusing on the temperature effect of the pyrolysis. One study converted oak wood particles to biochar through an intermediate pyrolysis at 500 and 800 °C then to activated carbon and found that the biochar had over 80 wt.% of C and pH around 8 (Jung and Kim, 2014). The biochar prepared at 500 ° has a higher H/C ratio than the one prepared at 800 °C, which indicates that the biochar prepared at 500 C had a lower aromaticity. The carbon prepared through the intermediate pyrolysis in nitrogen at 500 °C did not have substantial pore development while the surface area of 800 °C biochar was increased. They also indicated that SEM confirmed a more developed and organized microporous characteristics at the higher pyrolysis temperature than at the lower temperature. Pallarés et al. (2018) found that when barley straw was under pyrolysis temperature of from 500 to 600 °C, the surface area of final activated carbon was decreased from 789 to 704 $m^2/g$. This trend is also applicable to total volume and micropore volume. It was believed by the authors in this study that, generally, higher temperature during pyrolysis could generate more release of volatile matter from biochar, leading to more new pores being created in the activation step (Pallarés et al. 2018). However, pyrolysis temperature cannot

be too high in order to avoid the reduction of microporous structures, which is resulted from the blocking effect of large molecular volatiles being softened and sintered (Pallarés et al. 2018, Lua et al. 2006). The heating rate is another factor which could influence the surface area. It is well reported that the increased heating rates resulted in an increase of surface area, total volume and micropore volume (Lua et al. 2004 and 2006, Bouchelta et al. 2012).

Regarding to the chemical changes in the biochar based on different temperature, solid state $^{13}C$ NMR analysis has showed that the condensed aromatic structures increases as the pyrolysis temperature gets higher, while the surface area and pore volume decreases (Park et al. 2013). Yuan et al. (2011) has investigated the pH of the biochar from different biomass sources by different pyrolysis temperature from 300-700 °C. They found that as the pyrolysis temperature goes up, the pH of the biochar increases. The zeta potential showed that the biochar surface carries negative charges and the potential dropped as the temperature increases, which could be used to manipulate the negative charges of biochar (Yuan et al. 2011). The oxygen containing functional groups like carboxylic and hydroxyl contributed considerably to the surface charge of the biochar (Chiang and Juang, 2017).

The objective of this study is to investigate the effects of pyrolysis temperature in the preparation of biochar on the eventual activated carbon physicochemical properties. A deep understanding on these effects could better optimize the quality of activated carbon derived from lignocellulosic biomasses.

## 5.3. Material and Method

### 5.3.1. Materials

Four lignocellulosic biomasses have been selected in this study to represent wood and grass species. Eastern white pine and hybrid willow are representing softwood and hardwood, respectively. The switchgrass is a widely spread grass species while the miscanthus grass could provide larger biomass yield and is a supplementary to switchgrass. Eastern white pine and miscanthus grass were provided by Division of Forestry and Natural Resources and Division of Plant and Soil Science at West Virginia University, respectively. Hybrid willow was provided by the Geneva Agricultural Station of Cornell University. Switchgrass was provided by Department of Horticulture at Rutgers University. The four lignocellulosic biomasses were chipped and milled into particles less than 1.0 mm before any processing.

### 5.3.2. Processing

The activated carbon was prepared using a traditional two-step method. The first phase is to conduct pyrolysis in nitrogen flow to prepare biochar. The first step is usually referred as intermediate pyrolysis. Ten grams of biomass were contained in an aluminum combustion boat (203 mm×102 mm, AdValue Technology, Tucson, AZ) later placed into a tube furnace (Lindberg, Model 23-891). The pyrolysis temperatures were 450 °C and 1000 °C. The resident time of pyrolysis was 30 min for all samples. The second step is to place the cooled biochar into a carbon dioxide flow then activate them. In the second step, the 3 grams cooled biochar was placed into the container then activated physically in carbon dioxide at 800 °C. The residence time of activation was 60 mins for all samples. The heating rate of 10 °C/min was set for both pyrolysis and activation processes.

### 5.3.3. $N_2$ Adsorption and Desorption NLDFT Pore Size Distribution

A Micromeritics ASAP2020 surface area analyzer was used for $N_2$ physisorption tests. Nitrogen sorption at 77 K was carried out on a Micromeritics ASAP 2020 surface area and porosimetry system (Micromeritics Instrument Corporation, Norcross, GA) to obtain the adsorption-desorption isotherm of each sample. The Brunauer-Emmett-Teller (BET) specific surface area, total pore volume, volume of meso-pores, volume of micro-pores. Pore size distributions were calculated from the nitrogen sorption isotherm using the nonlocal density functional theory (NLDFT). The samples were degassed at 105 °C for 24 hours before the tests. Specific surface area and other pore related parameters were obtained from this step.

### 5.3.4. Scanning Electron Microscope (SEM)

The samples were characterized with Hitachi S-4700 SEM. The accelerating voltage was set at 5.0 kV. The magnification ranges from 5 μm to 100 μm. The scanning electron microscope was used to image the surface of the biochar and activated carbon. The SEM experimental section in this study is to display a general micrometer level morphology of the biochar and activated carbon materials.

### 5.3.5. Raman Spectroscopy

The biochar and activated carbon samples from four biomasses were investigated with Renishaw InVia Raman Microscope. The instrument was operated with less than 1 micrometer lateral spatial resolution and 532 nm excitation wavelengths at 100 mW maximum power. During the spectra

sampling, the power of the lazar was set at 10% for all samples to avoiding potential interference or destruction of the samples. The spectra were collected by using the centered mode around 1500 $cm^{-1}$, which resulting a coverage wavenumber of 1100-1850 $cm^{-1}$. The exposure time was 5 s for each sample and three collecting accumulations were adopted.

## 5.4. Results

### 5.4.1. Yield

The yield study showed a clearly trend that higher intermediate pyrolysis temperature could increase the yield of the final activated carbon based on the weight of initial biomass feedstock. Among four species, hybrid willow has the lowest yield value of activated carbon at both pyrolysis temperatures. Regarding to the pyrolysis yield, the 450 °C gives a higher yield of biochar than 1000 °C. This is due to that biomass is less degraded at 450 °C than at 1000 °C. It was reported in many reports that the increased pyrolysis temperature could increase the carbon content, pH and electrical conductivity of biochar (Marra et al. 2018). It is observed that in the activation process, the yield of biochar to activated carbon is higher when using char from intermediate 1000 °C pyrolysis samples than the 450 °C ones. This could be explained by the more chemical stable structure found in biochar from 1000 °C pyrolysis.

Table 5. 1. The yields of activated carbon from char prepared at 450 and 1000 °C.

| Yield | Pyrolysis | Activation | Total |
|---|---|---|---|
| HWAC450 | 29.7% | 31.0% | 9.2% |
| HWAC1000 | 22.5% | 63.4% | 14.3% |
| EWPAC450 | 27.1% | 51.7% | 14.0% |
| EWPAC1000 | 23.0% | 80.5% | 18.5% |
| MGAC450 | 27.5% | 51.3% | 14.1% |
| MGAC1000 | 21.3% | 90.7% | 19.3% |
| SGAC450 | 31.7% | 42.7% | 13.5% |
| SGAC1000 | 26.1% | 71.5% | 18.7% |

### 5.4.2. $N_2$ Adsorption and Desorption

The Figure 5.1 displays the isotherms for adsorption and desorption of nitrogen by testing all the activated carbon materials. It is observed that all isotherms belong to a mixture of Type I and Type II isotherm, according to the standard diagram from IUPAC (Thommes et al. 2015). This is based on the shape of these isotherms. Firstly, these is a sharp increase at low relative pressure and soon becomes flat when it comes to mediate relative pressure. This is typical Type I isotherm characteristics. However, at high relative pressure (0.8-1.0), instead of being flat, the isotherm keeps increasing. This is a sign for having macro-porous structure, which refers to the presence of Type II isotherm. The hysteresis loop observed in these isotherms are typical H4 type. This is the direct evidence that these activated carbons have a composite of Type I and II.

The Table 5.2 listed the porosity parameters of eventual activated carbon from all four species. As the intermediate pyrolysis temperature increases, all four biomass species showed a significant decreased BET specific surface area, total pore volume, and micro-pore volume. It is observed that the micro-/total volume ratio has slightly decreased in hybrid willow while it has increased in other three species, especially in eastern white pine and miscanthus grass.

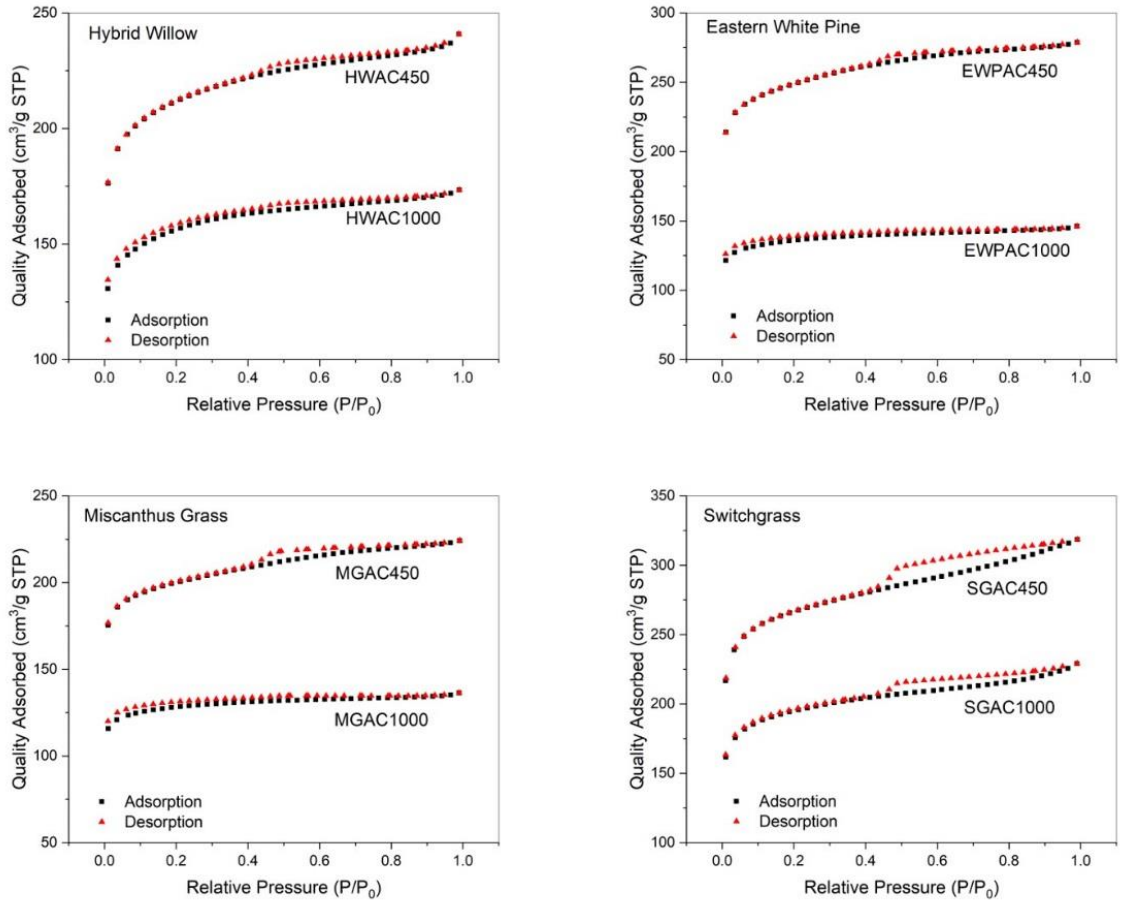


Figure 5. 1. The adsorption and desorption isotherms of activated carbon from char prepared at 450 and 1000 °C.

Table 5. 2. Porosity parameters of activated carbon from char prepared at 450 and 1000 °C.

| | SSA (BET) ($m^2/g$) | Pore Vol. ($cm^3/g$) | Micropore Vol. ($cm^3/g$) | Pore Size (BET) (nm) |
|---|---|---|---|---|
| HWAC450 | 750.7 | 0.37 | 0.22 | 1.98 |
| HWAC1000 | 553.2 | 0.27 | 0.15 | 1.94 |
| EWPAC450 | 876.0 | 0.43 | 0.27 | 1.96 |
| EWPAC1000 | 481.7 | 0.23 | 0.17 | 1.87 |
| MGAC450 | 707.7 | 0.35 | 0.23 | 1.96 |
| MGAC1000 | 454.3 | 0.21 | 0.16 | 1.85 |
| SGAC450 | 946.1 | 0.49 | 0.27 | 2.08 |
| SGAC1000 | 691.4 | 0.35 | 0.20 | 2.05 |

### 5.4.3. NLDFT Pore Size Distribution

The NLDFT pore size distribution was conducted with Micromeritics SAIEUS software. The model of the analysis was Carbon-$N_2$, 2D-NLDFT heterogeneous surface. The adsorption data of each sample was used to analyze its pore size distribution. The important parameters during the analysis were listed in Table 3 and the pore size distributions were plotted in Figure 5.2. The pore size distribution scale is 0-100 Å. The pore size range is 3.6 to 500 Å.

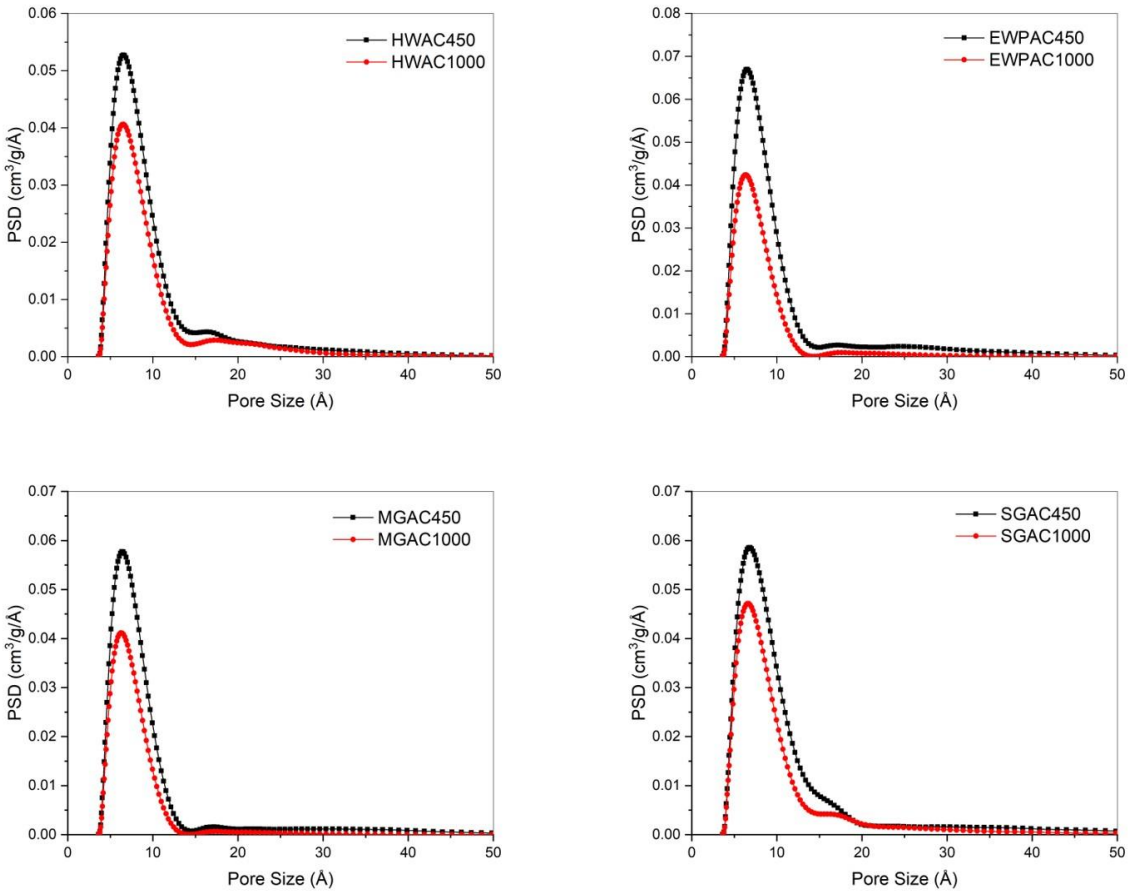


Figure 5. 2. Pore size distribution of resulted activated carbon by NLDFT method.

Pore size distribution of microporous structure dictates the efficiency of membrane or adsorbents in separation process, due to that it is directly affects the molecules transportation. (Kupgan et al. 2017, Khulbe et al. 2008). NLDFT is one of the most widely used way to create the isotherm of adsorption in ideal geometries of pores based on a classical fluid density functional theory (Kupgan et al. 2017). Generally, the pore size distribution from NLDFT method will be determined by the selected smoothing parameter λ (Kupgan et al. 2017).

Table 5. 3. The pore size distribution parameters by NLDFT method.

| Samples | Peak (Å) | λ |
|---|---|---|
| HWAC450 | 6.53 | 1.25 |
| HWAC1000 | 6.53 | 1.25 |
| EWPAC450 | 6.53 | 1.25 |
| EWPAC1000 | 6.37 | 1.25 |
| MGAC450 | 6.37 | 1.25 |
| MGAC1000 | 6.21 | 1.25 |
| SGAC450 | 6.86 | 1.25 |
| SGAC1000 | 6.53 | 1.25 |

As shown in Figure 5.2, the pore size of four species has a dominant portion of microporous range which is less than 2 nm (20Å). When the pore size is getting close to 5 nm, the pore size distribution is closing to 0 $cm^3/g/Å$. It indicates that the almost all the pores are less than 5 nm. It is worth noting that the NLDFT solution has a pore size range pre-set for analysis which is 3.6 to 500 Å. The larger pores are not simulated in this very solution. The peaks of the PSD and the smoothing parameter (λ) were listed in Table 5.3. The λ were self-generated by the SAIEUS software during fitting. Since λ is an adjustable parameter, all the values from different samples have been adjusted to the same value of 1.25 in order to compare. The peak shift showed that the majority of the pores does not shift in hybrid willow while does shift to lower size in other three species as the intermediate pyrolysis temperature increases. The peak values of all samples are within 6.2-6.9 Å.

### 5.4.4. Morphology

The microstructures of all samples were shown in Figure 5.3 and 5.4. The eastern white pine and switchgrass were selected to represent the wood and grass species, respectively. They were both observed with a pore size shift according to the pore size distribution analysis despite that SEM is not able to visually observe the micro- level change. However, it is still a useful tool to see the general textural change for biochar and activated carbon at different intermediate pyrolysis temperatures.

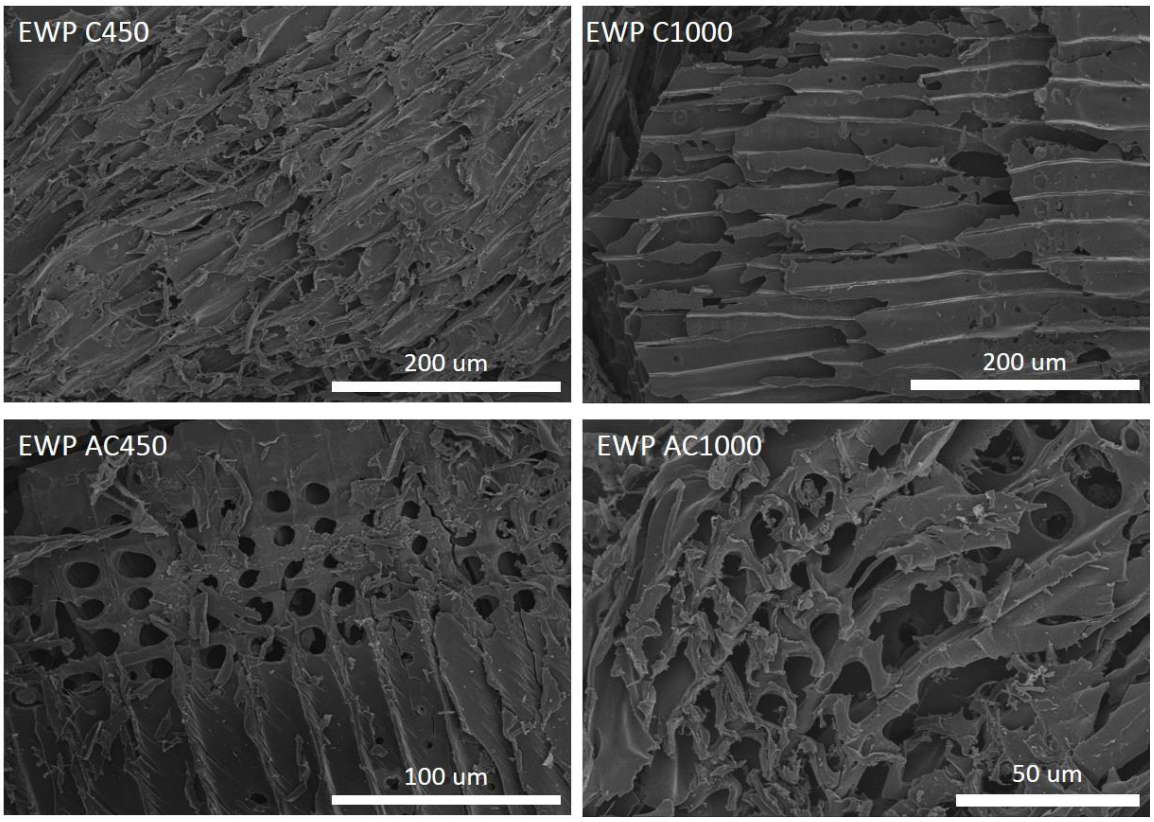


Figure 5. 3. SEM image of eastern white pine biochar and activated carbon.

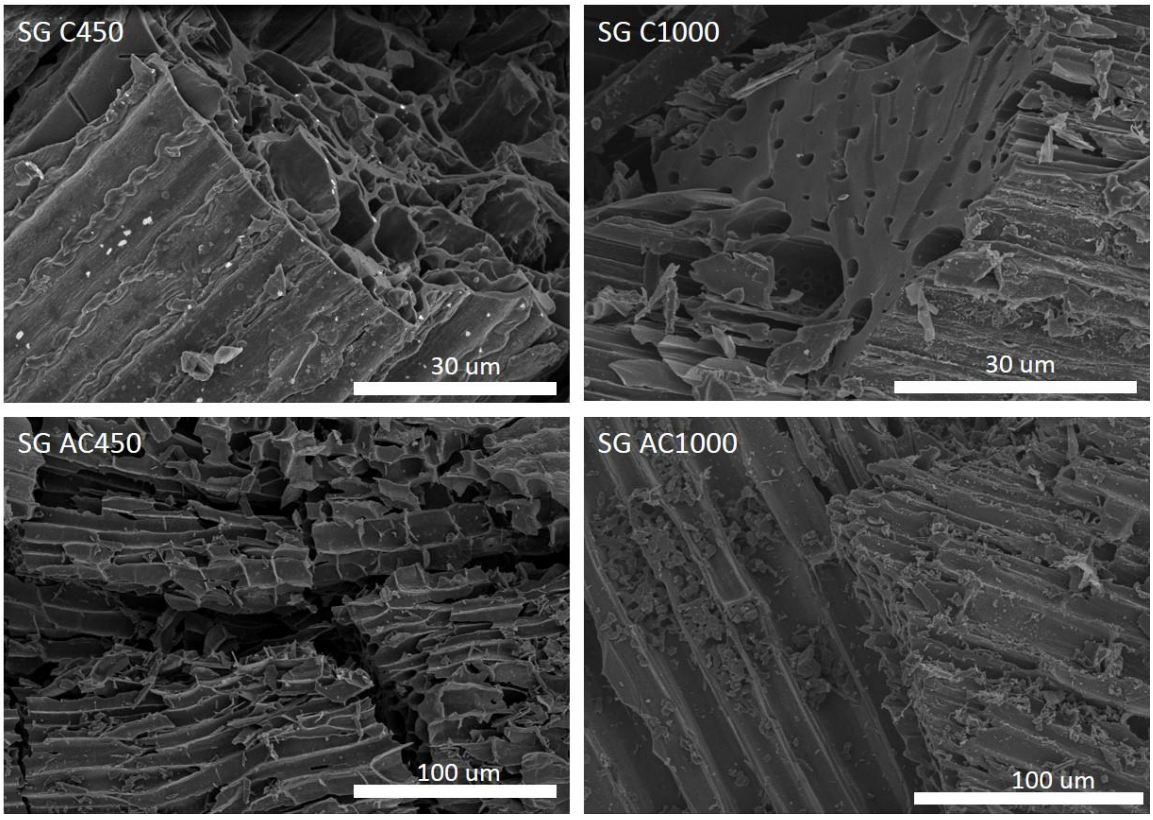


Figure 5. 4. SEM image of switchgrass biochar and activated carbon.

In Figure 5.3, for biochar, the eastern white pine shows a rigid texture at 1000 °C with relatively more pits open on the wood cell wall than 450 °C. This could be explained by biomass not being completely degraded at 450 °C. The observation becomes reverse when it comes to activated carbon. After activation, the activated carbon from 450 °C biochar has clearly rigid structure and the pores of the initial biomass structure were largely preserved. However, the activated carbon from 1000 °C biochar was observed with a likely collapsed structure despite of partly preserved structure.

### 5.4.5. Raman Spectroscopy

Raman spectroscopy is typically used for analyzing amorphous and crystalline carbon materials. The technique was applied to investigate the structure figures of biochar and corresponding activated carbons from four lignocellulosic biomass. Figure 5.5 shows the Raman spectra taken via centered mode which covers the wavenumber 1100-1850 $cm^{-1}$ of four lignocellulosic biomass derived biochar and activated carbon. The two broad bands observed in each spectrum at 1350 and 1580 $cm^{-1}$ were observed, which are referring to the D and G band of carbon materials, respectively.

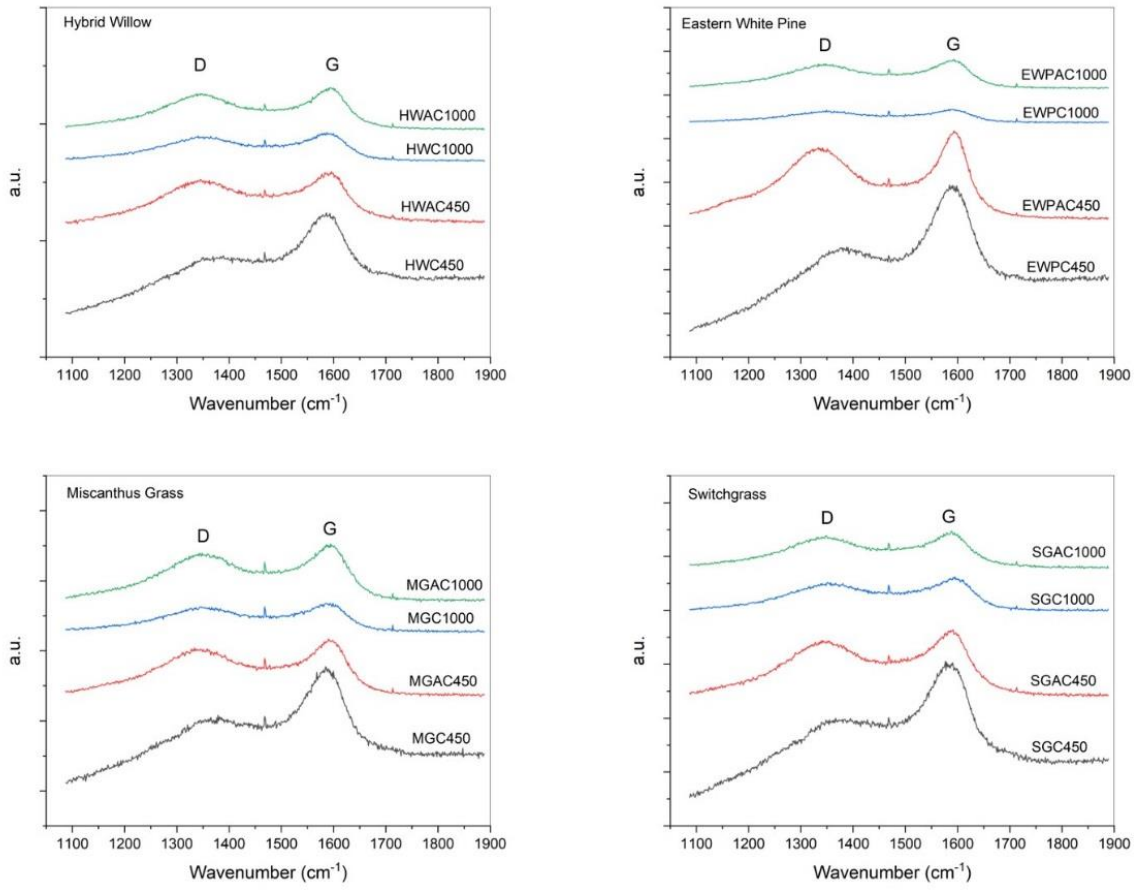


Figure 5. 5. Raman spectroscopy of both biochar and resulted activated carbon.

These spectra of biochar and activated carbon showed the existence of aromatic carbon, which group them to non-graphitic carbon materials. The biomass derived biochar or activated carbon materials have oxygen and different aliphatic compounds, which separate them from the highly ordered carbon materials like graphite (Azargohar et al. 2014, Keown et al. 2007). The D and G bands each should be grouped to polyaromatic and graphitic carbons, respectively (Guerrero et al. 2008). The D band showed the existence of aromatic rings that have six or more rings and disordered graphitic lattice (Azargohar et al. 2014, Li et al. 2016).

Table 5. 4 .Raman spectroscopy parameters of biochar and resulted activated carbon.

| | D peak | G peak | $I_D/I_G$ |
|---|---|---|---|
| HWC450 | 1388 | 1583 | 0.71 |
| HWAC450 | 1353 | 1585 | 0.86 |
| HWC1000 | 1352 | 1585 | 0.82 |
| HWAC1000 | 1348 | 1588 | 0.91 |
| EWPC450 | 1383 | 1588 | 0.71 |
| EWPAC450 | 1337 | 1589 | 0.85 |
| EWPC1000 | 1349 | 1589 | 0.96 |
| EWPAC1000 | 1345 | 1587 | 0.86 |
| MGC450 | 1379 | 1583 | 0.74 |
| MGAC450 | 1348 | 1588 | 0.85 |
| MGC1000 | 1353 | 1585 | 0.88 |
| MGAC1000 | 1352 | 1588 | 0.84 |
| SGC450 | 1384 | 1581 | 0.73 |
| SGAC450 | 1348 | 1582 | 0.86 |
| SGC1000 | 1358 | 1588 | 0.90 |
| SGAC1000 | 1348 | 1582 | 0.95 |

The Table 5.4 listed the $I_D/I_G$ ratios of all samples. It was observed that a sudden increase which means a dramatic structure change in biochar when pyrolysis temperature was raised from 450 to 1000 °C. The ratio has increase from 0.71 to 0.82, 0.71 to 0.96, 0.74 to 0.88, and 0.73 to 0.90 in hybrid willow, eastern white pine, miscanthus grass and switchgrass. The observation could be attributed to the increasing number of aromatic rings caused by the dehydrogenation of aromatics

due to high temperature (Azargohar et al. 2014, Li et al. 2016). The increasing $I_D/I_G$ ratios reveals the defect portion inside the carbon materials increases while the graphite portion decreases. However, it is merely a relative change rather than an actual change. It is safe to conclude that the as the intermediate temperature goes up, the amorphous carbon has an increasing trend in both biochar and activated carbon.

## 5.5. Discussion

### 5.5.1. Effect of intermediate pyrolysis temperature on porosity

Based on the porosity parameters showed in results part, the intermediate pyrolysis temperature does affect the specific surface area, microporous volume and total volume. The lower temperature at 450 °C has higher values of three parameters than at 1000 °C. Although it is the activation process that plays a dominant role in pore development, the biochar preparation does have a preliminary effect on the final porosity. This could be evidenced by the morphology observation previously described. The result could also be proofed by a study which has conducted surface area and pore volumes analysis of biochar prepared from 400 to 600 °C. The reported work showed that when the pyrolysis temperature was increased from 400 to 500 °C, the specific surface area, microporous volume and total volume have reached their maxima (Angin 2013). It added on to display that when the temperature rose above 550 °C, the porosity has a decreasing trend. At intermediate pyrolysis temperature 450 °C, as volatiles was released, pore volume and specific surface area increased with a specific jump in microporous structure (Angin 2013). Above 500 °C, a reduction in porosity parameters was observed due to the increase of ordered structure, wider pores and pore sintering (Angin 2013). Fu et al. (2011) also covered that high pyrolysis temperature could result in softening, melting, and fusing of the pores which lead them to be the

partially blocked. The SEM analysis of Angin (2013) showed that when the temperature is above 500 °C, the biochar displayed shrinkage due to post-softening and swelling which leading to narrow or closed pores.

### 5.5.2. Effect of intermediate pyrolysis temperature on pore size and chemical structure

The pore size analysis was provided by surface area analyzer and NLDFT method both reveal that the pore size has decreased when increased the intermediate pyrolysis temperature from 450 to 1000 °C. The trend is in consistence with the result of Gai et al. (2014). The reported work showed a decreasing pore size from 8 nm to 2 nm when the pyrolysis temperature of biomass decreased increased from 400 to 700 °C. The report applied Field Emission-SEM which could have a better resolution (<2nm) to observe the structure of the pores. The biochar was imaged to have cylinder-like pores. The observation showed that the disordered fold structure has converted to ordered layer structure as the temperature increases. The laminated texture at higher temperature is believed to be the reason for reduced pore size (Gai et al. 2014). The current work and the reported one agrees on that although biochar has low specific surface area and pore volume, it has a major portion of micro-pores which are less than 2 nm. The activation step is the step which could largely improve the porosity despite of not changing the size of the microporous structure.

## 5.6. Conclusion

This work has successfully investigated the effect of intermediate pyrolysis temperature on the physicochemical properties of biochar and eventual activated carbon materials. The higher pyrolysis temperature generated a higher yield of eventual activated carbon while it gives a lower

yield of the biochar. The activated carbon materials from all four species has a higher specific surface area, total pore volume and microporous volume at intermediate pyrolysis temperature 450 °C than at 1000 °C. The SEM further confirmed the possible collapse of the pore development due to the high temperature during biochar processing. The spectra of Raman showed that the higher pyrolysis temperature displayed a lower graphitization degree which is due to the increased amorphous carbon structure.

## 5.7. References

Abioye, A.M. and Ani, F.N., 2015. Recent development in the production of activated carbon electrodes from agricultural waste biomass for supercapacitors: a review. Renewable and sustainable energy reviews, 52, pp.1282-1293.

Ahmadpour, A. and Do, D.D., 1996. The preparation of active carbons from coal by chemical and physical activation. Carbon, 34(4), pp.471-479.

Angın, D., 2013. Effect of pyrolysis temperature and heating rate on biochar obtained from pyrolysis of safflower seed press cake. Bioresource technology, 128, pp.593-597.

Azargohar, R., Jacobson, K.L., Powell, E.E. and Dalai, A.K., 2013. Evaluation of properties of fast pyrolysis products obtained, from Canadian waste biomass. Journal of analytical and applied pyrolysis, 104, pp.330-340.

Azargohar, R., Nanda, S., Kozinski, J.A., Dalai, A.K. and Sutarto, R., 2014. Effects of temperature on the physicochemical characteristics of fast pyrolysis bio-chars derived from Canadian waste biomass. Fuel, 125, pp.90-100.

Bagheri, N. and Abedi, J., 2009. Preparation of high surface area activated carbon from corn by chemical activation using potassium hydroxide. Chemical engineering research and design, 87(8), pp.1059-1064.

Bouchelta, C., Medjram, M.S., Zoubida, M., Chekkat, F.A., Ramdane, N. and Bellat, J.P., 2012. Effects of pyrolysis conditions on the porous structure development of date pits activated carbon. Journal of Analytical and Applied Pyrolysis, 94, pp.215-222.

Chang, C.F., Chang, C.Y. and Tsai, W.T., 2000. Effects of burn-off and activation temperature on preparation of activated carbon from corn cob agrowaste by CO2 and steam. Journal of Colloid and Interface Science, 232(1), pp.45-49.

Chen, X., Li, Z., Wei, L., Li, X., Liu, S. and Gu, J., 2015. Fabrication of hierarchical cabbage-like carbonaceous materials by one-step cobalt-assisted hydrothermal carbonization of furfural. Microporous and Mesoporous Materials, 210, pp.149-160.

Chiang, Y.C. and Juang, R.S., 2017. Surface modifications of carbonaceous materials for carbon dioxide adsorption: A review. Journal of the Taiwan Institute of Chemical Engineers, 71, pp.214-234.

Chingombe, P., Saha, B. and Wakeman, R.J., 2005. Surface modification and characterisation of a coal-based activated carbon. Carbon, 43(15), pp.3132-3143.

Fu, P., Yi, W., Bai, X., Li, Z., Hu, S. and Xiang, J., 2011. Effect of temperature on gas composition and char structural features of pyrolyzed agricultural residues. Bioresource Technology, 102(17), pp.8211-8219.

Gai, X., Wang, H., Liu, J., Zhai, L., Liu, S., Ren, T. and Liu, H., 2014. Effects of feedstock and pyrolysis temperature on biochar adsorption of ammonium and nitrate. PloS one, 9(12), p.e113888.

Guerrero, M., Ruiz, M.P., Millera, Á., Alzueta, M.U. and Bilbao, R., 2008. Characterization of biomass chars formed under different devolatilization conditions: differences between rice husk and eucalyptus. Energy & Fuels, 22(2), pp.1275-1284.

Hayashi, J.I., Kazehaya, A., Muroyama, K. and Watkinson, A.P., 2000. Preparation of activated carbon from lignin by chemical activation. Carbon, 38(13), pp.1873-1878.

Jung, S.H. and Kim, J.S., 2014. Production of biochars by intermediate pyrolysis and activated carbons from oak by three activation methods using CO2. Journal of analytical and applied pyrolysis, 107, pp.116-122.

Karagöz, S., Tay, T., Ucar, S. and Erdem, M., 2008. Activated carbons from waste biomass by sulfuric acid activation and their use on methylene blue adsorption. Bioresource technology, 99(14), pp.6214-6222.

Keown, D.M., Li, X., Hayashi, J.I. and Li, C.Z., 2007. Characterization of the structural features of char from the pyrolysis of cane trash using Fourier Transform− Raman spectroscopy. Energy & fuels, 21(3), pp.1816-1821.

Khulbe, K.C., Feng, C.Y. and Matsuura, T., 2007. Synthetic polymeric membranes: characterization by atomic force microscopy. Springer Science & Business Media.

Kupgan, G., Liyana-Arachchi, T.P. and Colina, C.M., 2017. NLDFT pore size distribution in amorphous microporous materials. Langmuir, 33(42), pp.11138-11145.

Marra, R., Vinale, F., Cesarano, G., Lombardi, N., d'Errico, G., Crasto, A., Mazzei, P., Piccolo, A., Incerti, G., Woo, S.L. and Scala, F., 2018. Biochars from olive mill waste have contrasting effects on plants, fungi and phytoparasitic nematodes. PloS one, 13(6), p.e0198728.

Li, X., Hayashi, J.I. and Li, C.Z., 2006. FT-Raman spectroscopic study of the evolution of char structure during the pyrolysis of a Victorian brown coal. Fuel, 85(12-13), pp.1700-1707.

Liou, T.H., 2010. Development of mesoporous structure and high adsorption capacity of biomass-based activated carbon by phosphoric acid and zinc chloride activation. Chemical Engineering Journal, 158(2), pp.129-142.

Lua, A.C., Yang, T. and Guo, J., 2004. Effects of pyrolysis conditions on the properties of activated carbons prepared from pistachio-nut shells. Journal of analytical and applied pyrolysis, 72(2), pp.279-287.

Lua, A.C., Lau, F.Y. and Guo, J., 2006. Influence of pyrolysis conditions on pore development of oil-palm-shell activated carbons. Journal of analytical and applied pyrolysis, 76(1-2), pp.96-102.

Pallarés, J., González-Cencerrado, A. and Arauzo, I., 2018. Production and characterization of activated carbon from barley straw by physical activation with carbon dioxide and steam. Biomass and bioenergy, 115, pp.64-73.

Park, J., Hung, I., Gan, Z., Rojas, O.J., Lim, K.H. and Park, S., 2013. Activated carbon from biochar: influence of its physicochemical properties on the sorption characteristics of phenanthrene. Bioresource technology, 149, pp.383-389.

Thommes, M., Kaneko, K., Neimark, A.V., Olivier, J.P., Rodriguez-Reinoso, F., Rouquerol, J. and Sing, K.S., 2015. Physisorption of gases, with special reference to the evaluation of surface area and pore size distribution (IUPAC Technical Report). Pure and Applied Chemistry, 87(9-10), pp.1051-1069.

Yuan, J.H., Xu, R.K. and Zhang, H., 2011. The forms of alkalis in the biochar produced from crop residues at different temperatures. Bioresource technology, 102(3), pp.3488-3497.

## Chapter 6. Summary

Lignocellulosic biomass has been successfully converted to activated carbon and used for energy storage and adsorption applications in this study. The fabricated activated carbon was comprehensively characterized by different scientific techniques. The influence of oxidative torrefaction on the lignocellulosic biomass was further studied. Lastly, the effect of intermediate pyrolysis temperature on the properties of lignocellulosic biomass derived activated carbon was investigated. The major findings could be summarized as follows:

(1) Lignocellulosic biomass has been successfully converted to highly porous activated carbon by direct and indirect activation processing using carbon dioxide. The activated carbon prepared by both activation methods have been fabricated to supercapacitor electrode and characterized for electrochemical performance. The activated carbon prepared by direct activation at 800 °C for 60 min has the highest BET specific surface area of 738.74 $m^2/g$ and total pore volume of 0.37 $cm^3/g$. The activated carbon prepared by indirect activation with an intermediate pyrolysis temperature of 450 °C has the highest BET specific surface area of 750.70 $m^2/g$ and total pore volume of 0.37 $cm^3/g$. The capacitance of direct and indirect activated carbon reaches the highest value of 80.9 and 92.7 F/g at current density of 100 mA/g, respectively. The assembled capacitor could run 1000 cycles with only slight capacitance loss (<0.5%). The surface chemistry reveals that the graphitization degree of carbon increases as the temperature increases during biochar preparation step in indirect activation process while it decreases as temperature increases during direct activation process. The study also found that the electrochemical performance is not only dependent with porosity but also heavily related with the functional groups on the carbon surface.

(2) Lignocellulosic derived activated carbons from two different routes of KOH carbonization have been successfully fabricated and characterized. The yield study showed that the direct KOH carbonization has a higher yield of 18.2 % than 14.7 % of indirect carbonization. The porosity

parameters of activated carbon such as specific surface area, total pore volume and microporous volume are relatively higher in direct KOH activation samples. The Barium adsorption test showed that both activated carbons can be used to adsorb Ba from actual shale gas flowback water. The activated carbon from direct KOH carbonization has a higher reduction rate which is 11.3% at a relatively low carbon loading (carbon to water mass ratio at 1:38). The oxygen containing functional groups of activated carbon has mainly contributed to the adsorption of barium.

(3) The influence of oxidative torrefaction on the chemical and structural properties of the four lignocellulosic biomasses was investigated. The yield study showed that along with the decreasing heating rate, the weight of the torrefied char decreases duo to further release of moisture and volatiles. The thermal degradation of different biomasses displayed a peak shift to lower temperatures because of the hemicellulose degradation during oxidative torrefaction. The elemental analysis showed that the H/C decreases with reducing heating rates. The range of the H/C ratio in selected wood and grass species decreased from 1.34 to 1.30 and 1.18 to 1.04, respectively. The infrared spectroscopy analysis indicated that the hemicellulose, amorphous cellulose and lignin have been decomposed based on the weakened characteristic peaks or shifted peaks. The microstructure images showed that the oxidative torrefaction could reserve the tubular structure of biomasses and create porosity at mediate level of 250 °C. The oxidative torrefaction is a potential pretreatment for biomass to improve its quality for further conversion.

(4) The effect of intermediate pyrolysis temperature on the physicochemical properties of biochar and eventual activated carbon materials was studied. The higher pyrolysis temperature generated a higher yield of eventual activated carbon while it gave a lower yield of the biochar. The activated carbon materials from all four species has a higher specific surface area, total pore volume and microporous volume at intermediate pyrolysis temperature 450 °C than these at 1000 °C. The SEM

further confirmed the possible collapse of the pore development due to the high temperature during biochar processing. The spectra of Raman showed that the higher pyrolysis temperature displayed a lower graphitization degree which is due to the increased amorphous carbon structure. Lower intermediate pyrolysis could better preserve the natural structure of lignocellulosic biomass and should be adopted in two-stage carbon dioxide activation for better pore development.

Future research on lignocellulosic derived activated carbon for energy storage should be focused on creating controlled process with pre-defined temperature, residence time and activation method for enhanced performance of the electrode, which could be applied not only to the supercapacitor application but to other energy storage fields. The cost-effectiveness should be taken into consideration to make sure the process is economically feasible. For adsorption application, the future research should be stressed on the development of suitable adsorption method beside static adsorption. Pressured water injection could be considered and compared. The saturation test and adsorption-temperature relations could be further studied to have a comprehensive insight on the biomass derived activated carbon products.